UNIVERSIDADE ESTADUAL PAULISTA "JÚLIO DE MESQUITA FILHO" – UNESP
PROGRAMA DE PÓS-GRADUAÇÃO EM CIÊNCIA E TECNOLOGIA DE MATERIAIS – POSMAT

Lucas Jorge Affonço

METAL OXIDES AS TRANSPORT LAYER FOR PEROVSKITE SOLAR CELLS.

Bauru

2024

Lucas Jorge Affonço

METAL OXIDES AS TRANSPORT LAYER FOR PEROVSKITE SOLAR CELLS.

Tese apresentada como requisito à obtenção do título de Doutor à Universidade Estadual Paulista "Júlio de Mesquita Filho" - Programa de Pós-Graduação em Ciência e Tecnologia de Materiais, área de concentração Ciência e Tecnologia de Materiais, sob a orientação do Prof. Dr. José Humberto Dias da Silva

Bauru

2024

Affonço, Lucas Jorge.
Metal Oxides as Transport Layer for Perovskite Solar Cells / Lucas Jorge Affonço. – Bauru, 2024
90 f.: il.

Tese (Doutorado)–Universidade Estadual Paulista (Unesp), Faculdade de Ciências, Bauru
Orientador: José Humberto Dias da Silva

1. Metal Oxides. 2. Transport Layers. 3. Deposition Methods. 4. Perovskite Solar Cell. 5. Photovoltaic devices. I. Universidade Estadual Paulista. Faculdade de Ciências. II. Título.

UNIVERSIDADE ESTADUAL PAULISTA

Câmpus de Bauru

ATA DA DEFESA PÚBLICA DA TESE DE DOUTORADO DE LUCAS JORGE AFFONÇO, DISCENTE DO PROGRAMA DE PÓS-GRADUAÇÃO EM CIÊNCIA E TECNOLOGIA DE MATERIAIS, DA FACULDADE DE CIÊNCIAS - CÂMPUS DE BAURU.

Aos 18 dias do mês de dezembro do ano de 2023, às 08:30 horas, por meio de Videoconferência, realizou-se a defesa de TESE DE DOUTORADO de LUCAS JORGE AFFONÇO, intitulada **Metal Oxides as Transport Layer for Perovskite Solar Cell**. A Comissão Examinadora foi constituida pelos seguintes membros: Prof. Dr. JOSE HUMBERTO DIAS DA SILVA (Orientador(a) - Participação Presencial) do(a) Departamento de Física / Faculdade de Ciências - Unesp/ Câmpus de Bauru, Profa. Dra. EVA UNGER (Participação Virtual) do(a) IRIS Adlershof e HySPRINT Innovation Lab / Humboldt Universität zu Berlin e Helmholtz-Zentrum Berlin., Prof. Dr. EUDES BORGES DE ARAUJO (Participação Virtual) do(a) Departamento de Física e Química / Faculdade de Engenharia de Ilha Solteira - Unesp, Prof. Dr. AUGUSTO BATAGIN NETO (Participação Virtual) do(a) Departamento de Ciências e Tecnologia / Instituto de Ciências e Engenharia - Unesp/Câmpus de Itapeva, Profa. Dra. LUANA CRISTINA WOUK (Participação Virtual) do(a) Instituto de Física / Universidade de Brasília. Após a exposição pelo doutorando e arguição pelos membros da Comissão Examinadora que participaram do ato, de forma presencial e/ou virtual, o discente recebeu o conceito final: aprovado . Nada mais havendo, foi lavrada a presente ata, que após lida e aprovada, foi assinada pelo(a) Presidente(a) da Comissão Examinadora.

Prof. Dr. JOSE HUMBERTO DIAS DA SILVA

Agradecimentos

A Deus sobre todas as coisas.

A minha família por tudo que tenho e sou.

Ao meu orientador, José Humberto Dias da Silvia, por tantos anos de dedicação, confiança apoio e ensinamentos.

Aos amigos da Bujinkan Bauru pelos treinos de corpo, mente e espírito.

Aos amigos, Roberto, Vinicius, Bruno, Lucas, Larissa, Raquel, Max, Bor, Aleksandra, Jesus, Lea e Chiara, pela amizade cultivada, por me acolherem e pelas mais variadas conversas e momentos.

Aos professores Eva Unger, Carlos F. de O. Graeff e Eudes B. de Araújo por abrirem as portas para meu intercambio.

A minha coorientadora Silvia L. Fernandes, por me ensinar tanto sobre as células solares e o apoio durante esse tempo.

Aos colegas do LFS e do SE-ALM, em especial Nilton, Janardan e Natalia pelos tantos ensinamentos, ajudas, ideias e troca de experiência.

Aos depois colegas dos CASCA e HySprint pelos dias compartilhados nos laboratórios e mais diversas colaborações.

Aos técnicos de laboratório pela supervisão e manutenção dos laboratórios e equipamentos.

E por fim, a todas as pessoas que passaram pela minha jornada e me estenderam a mão em algum momento ou que me ensinaram algo, para o bem ou o mal.

“Any sufficiently advanced technology is indistinguishable from magic.”

Clarke, C. Arthur

"Entities must not be multiplied beyond necessity."

of Ockham, William

AFFONÇO, L. J. **Metal Oxides as Transport Layer for Perovskite Solar Cell**. 2023. 90p. Thesis (Programa de Pós-Graduação em Ciência e Tecnologia de Materiais) – UNESP, Faculdade de Ciências, Bauru, 2024.

Resumo

Atualmente as células solares de perovskitas atraem grande interesse no campo de energias renováveis, principalmente devido ao rápido aumento de eficiência alcançada por esses dispositivos. Entretanto, para alcançarem o mercado, desafio associados a estabilidade e produção em larga escala precisam ser superados. Nessas células, apesar da camada de perovskita ser crucial, ela sozinha possivelmente não alcançaria o destaque que possui, sendo sua combinação com outras camadas de grande importância. As camadas transportadoras, auxiliam na extração de cargas, e os materiais que as compõe se mostram fatores fundamentais para que os dispositivos alcancem resultados expressivos, sendo o foco deste trabalho nas camadas seletivas.

Primeiramente, foi investigado a deposição do pentóxido de nióbio (camada transportadora de elétrons) por *slot die coating*. Este material se mostrou uma boa alternativa a tradicional utilização do dióxido de titânio. Além disso, a deposição por *slot die coating* é vantajosa por sua possibilidade de depositar camadas de diferentes materiais por meio de soluções e em grandes áreas. Para tal objetivo, diferentes parâmetros de deposição foram testados. As células solares de perovskita, foram construídas com êxito. Além disso, também foi investigado o impacto de estratégias de passivação entre a camada seletiva de elétrons de óxido de estanho e a perovskita. Utilizou-se cloreto de potássio, tanto como camada passivadora quanto aditivo na solução de perovskita. Em ambos os casos, as camadas foram avaliadas por meio de técnicas de microscopia e a performance do dispositivo pelas curvas J-V.

Considerando os dispositivos com base no pentóxido de nióbio por *slot die coating*, a eficiência alcançada na melhor células foi de aproximadamente 12 %. Apesar do valor estar abaixo do observado dos dispositivos presentes na literatura que beiram as mais altas eficiências, em geral estes utilizam outras técnicas de deposição, menos escaláveis e mais caras, sendo a obtenção do mesmo por *slot die coating* ainda não reportada. Quanto ao efeito da utilização do cloreto de potássio, houve o quase desaparecimento da histerese. A performance geral foi bem similar independendo do método de incorporação. Apesar disso, observou-se que a incorporação como aditivo pode ser prejudicial para camada de perovskita, sendo assim mais vantajoso a aplicação como camada passivadora ou ressaltando a necessidade de encontrar outra forma de incorporar na solução.

Palavras chaves: Óxidos metálicos, camadas transportadoras, métodos de deposição, células solares de perovskita, dispositivos fotovoltaico.

AFFONÇO, L. J. **Metal Oxides as Transport Layer for Perovskite Solar Cell**. 2023. 90p. Thesis (Programa de Pós-Graduação em Ciência e Tecnologia de Materiais) – UNESP, Faculdade de Ciências, Bauru, 2024.

Abstract

Nowadays, perovskite solar cells draw great interest in the energy harvest field mainly due to the rapid increase in efficiency. Nevertheless, challenges like the stability improvement and the scalability of the layers must be surpassed. Although the perovskite layer is the center of the device, this layer alone could not reach such high performance. Transport layers are necessary and offer great aid for charge extraction, and device performance, unveiling the importance of those layers and the materials used, being those layers the focus of this work.

Firstly, the niobium pentoxide deposition (electron transport layer) by slot die coating was investigated. The niobium pentoxide was presented as a viable alternative to the traditional titanium oxide, mainly due to a positive influence on the stability that might be seen through a reduction in the hysteresis. The slot die coating is an attractive solution-based deposition technique, as it allows the coating of a wide diversity of materials with high throughput, which can be favorable for large-scale production. For this goal, varied parameters were examined for the deposition process. Secondly, the usage of potassium chloride salt to mitigate the hysteresis effects between the transport layer and the perovskite was investigated, comparing its application as an additive in the perovskite precursor solution or as a passivation layer, in devices with tin oxide as transport layer. The layers were analyzed by microscopy, and the influence of the materials on the device performance was assessed using the J-V curves.

Considering the slot die coating of the niobium pentoxide, the layers were successfully obtained, and the best devices reached about 12 % efficiency. Although the obtained efficiency is still low compared to the present high-performance devices, obtained through other depositions techniques less scalable and more expensive, so far, no report on the slot die coating of the niobium pentoxide for perovskite solar cells was found, For the passivation, its utilization resulted in negligible hysteresis effects. Thus, either as a layer or additive, the performances were similar. However, the outcomes indicate that the usage as an additive might be a handicap for the perovskite being more favorable to use as a passivation layer.

Key words: Metal oxides, transport layers, deposition methods, perovskite solar cell, photovoltaic devices.

Abbreviations and symbols.

ºC – Degree Celsius

µL – Microliter

µm – Micrometer

µ - Viscosity

ρ – Density of the material

σ – Surface tension

τ_{fast} – Fast time constant

τ_{slow} – Slow time constant

AFM – Atomic force microscopy

ALD – Atomic layer deposition

AM – Air mass

AZO – Aluminium-doped zinc oxide (ZnO:Al)

BCP – Bathocuproine

BSE – Backscattered electrons

Ca – Capillary number

C_{60} – [60] Fullerene

$CaTiO_3$ – Calcium titanate

CBM – Conduction band minimum

cm^2 – Square centimeter

CoO – Cobalt oxide

CsFA – Cesium formamidinium perovskite ($Cs_{1-x}FA_xPb(I_{1-y}Br_y)_3$)

CsFAMA – Triple cation perovskite ($FA_{1-(x+y)}MA_xCs_yPb(I_{1-z}Br_z)_3$)

CsI – Cesium iodide

CuO_x – Cupper oxide

DMF – N,N-Dimethylformamide

DMSO – Dimethyl sulfoxide

DyMPPT – Dynamic maximum power point tracking

EDX – Energy dispersive X-ray

E_g – Band gap energy

EQE – External quantum efficiency

ETL – Electron transport layer

FA – Formamidinium ($CH(NH_2)_2^+$)

FAI – Formamidinium iodide

FAPI – Formamidinium lead iodide ($CH(NH_2)_2^+ PbI_3$)

FF – Fill factor

FK209 – FK209 Co(III) TFSI salt

FTO – Fluorine-doped tin oxide (SnO_2:F)

h – film thickness

h_d – Dry film thickness

h_w – Wet film thickness

H_0 – Gap of the slot die head

HI – Hysteresis index

HTL – Hole transport layer

Hz – Hertz

ITO – Indium tin oxide ($InSnO_2$)

IZO – Indium zinc oxide (InZnO)

J_{sc} – Short-circuit current density

J_{ss} – Steady state current density

J-V – Current density against voltage curves

KCl – Potassium chloride

LED – Light emitter diode

Li-TFSI – Bis(trifluoromethane)sulfonimide lithium salt

m^2 – Square meter

MA – Methylammonium (CH_3NH_3)

MABr – Methylammonium bromide

MAPI – Methylammonium lead iodide ($CH_3NH_3PbI_3$)

mg – Milligram

min – Minute

mL – Milliliter

mm – Millimeter

MPP – Maximum power point (P_{mpp})

MPPT – Maximum power point tracking

ms – Milliseconds

mV – Millivolts

Nb_2O_5 – Niobium pentoxide

NiO_x – Nickel oxide

P3HT – Poly(3-hexylthiophene)

$PbBr_2$ – Lead bromide

PbI_2 – Lead iodide

PCBM – [6,6] phenyl-C61-butyric acid methyl ester

PCE – Power conversion efficiency

PEDOT:PSS – Poly(3,4-ethylenedioxythiophene)−poly(styrenesulfonate)

PEIE – Polyethyleneimine ethoxylated

P_{in} – Incident power

PR – Pump rate

PSC – Perovskite solar cells

PTAA – Poly[bis(4-phenyl)(2,4,6-trimethylphenyl)amine]

PV – Photovoltaics

rpm – Revolutions per minute

SAM – Self-assembly monolayers

Sccm – Standard cubic centimeters per minute

SDC – Slot die coating

SE – Secondary electrons

SEM – Scanning electron microscopy

SnO_2 – Tin dioxide

Spiro-OMeTAD – 2,2′7,7′-tetrakis(N,N-di-p-methoxyphenyl amine)-9,9′-spirobifluorene

SPV – Surface photovoltage

TBP – 4-Tert-butylpyridine

TCO – Transparent conductive oxide

t_d – Settling / Delay time

TiO_2 – Titanium dioxide

TrAMPPT – Transient analysis during maximum power point tracking

t_s – Integration / Sampling time

UPS – Ultraviolet spectroscopy

UVVis – Ultraviolet visible (light) – referred to UVVis spectroscopy

V – Volts

VBM – Valence band maximum

V_{mpp} – Voltage of the MPP

V_{oc} – Open circuit voltage

w – coating width

W – Watts

WS – Web speed

XPS – X-Ray photoelectron spectroscopy

XRD – X-Ray diffraction

ZnO – Zinc oxide

Table of contents

1. Introduction

Over time, the world's demands for a sustainable future rise exponentially. The need for change is driven mainly by modern challenges like inhibiting climate change and global warming, in addition to political and economic concerns. Regarding the strategies to surpass those problems, the transition from fossil fuels to renewable energy is crucial, and photovoltaics (PV) devices plays a significant role in making renewable energy feasible.

For a long time, silicon solar cells have been the dominant photovoltaic technology in the market. However, a few decades back, a distinct series of materials ignited an evolution in the field (KOJIMA et al., 2009; LEE et al., 2012). Emerging from the dye-sensitized solar cells, the so-called perovskite solar cells (PSC) originated from the use of a lead halide perovskite as a sensitizer, which increased the efficiency of the dye-sensitized, showing 3.8 % of efficiency in 2009 as the first report (KIM et al., 2020; KOJIMA et al., 2009) and improving to 6.5 % in 2011 (KIM et al., 2020; IM et al., 2011).

Although, only in 2012, a solid-state PSC was reported, achieving the power conversion efficiency (PCE) of about 10 % (KIM et al., 2020; LEE et al., 2012). In the upcoming years, the PCE of the perovskite solar cells rapidly increased, reaching the certificated record of 25.7% for the device on a laboratory scale (MIN et al., 2021). The expressive increase of efficiency attracted the attention and efforts of the PV community, and significant advances in PSC technology in the past decade suggest those devices as the most promising candidates for the next generation of solar cells and a plausible substitute for the silicon solar cell.

Nevertheless, to reach this point of development and attractiveness for commercialization, it is still necessary to solve issues related to long-term stability and upscaling (HAN et al., 2022; RONG et al., 2018). Notwithstanding, for commercial production some requirements like, the deposition of all functional layers over larger areas, the material efficiency, competitive cost, and sustainable implementation must also be considered (RONG et al., 2018).

Those considerations motivate this work, wherein different aspects of the perovskite solar cell will be discussed and investigated. However, it will not be related directly to the perovskite as an absorber layer, thus indeed to the other layers that compose the devices, i.e., the transport layers, which will be presented in the following sections.

1.1 Perovskite solar cells

Perovskite is related to a crystalline structure, cubic lattice of space group $Pm\bar{3}m$, named over the calcium titanate ($CaTiO_3$), where the observation of this structure was first reported (FERNANDES, 2016; GAO; GRÄTZEL; NAZEERUDDIN, 2014). Nowadays, the name denotes materials with the same structure mentioned, which is used as an absorber layer in solar cells, given the denomination of perovskite solar cells. Generally, perovskite has the chemical formula ABX_3, where A and B are cations, and X represents the anion, as illustrated in Figure 1.

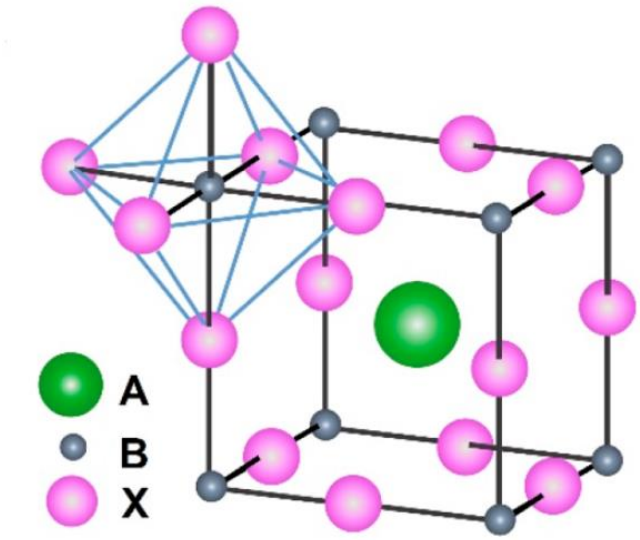

FIGURE 1. The ABX_3 schematic structure of perovskite. A and B represent the larger and smaller cations, respectively, and X the anions. Adapted from (KIM et al., 2020).

The pioneer perovskite material used as absorber layers in PSC was the hybrid organic-inorganic lead halide $MAPbI_3$ (methylammonium lead iodide; $CH_3NH_3PbI_3$, for short MAPI), reaching 9.7% of PCE (GREEN; HO-BAILLIE; SNAITH, 2014; LEE et al., 2012). Later, several other materials, mainly either substituting and/or combining different cations and/or anions, for example, right after the $FAPbI_3$ (FA = formamidinium; $CH(NH_2)_2^+$, or FAPI), emerged in search to push the performance further or to solve drawbacks of the MAPI.

Among the optoelectronics characteristics that make the perovskite an attractive absorbing layer are its tunable band gap (E_g ~1.6 - 2.5 eV), high absorption coefficient (>10^4 cm^{-1}), good mobility, and long charge carrier lifetime (GARCIA, 2022; HAN et al., 2022; HE et al., 2021). In addition to the suitable characteristics that lead the devices to the spotlight for

the next generation of energy harvesting, perovskite also presents some downsides, worthing efforts, and attention from the scientific community to understand and overcome.

Most of those concerns lie in reaching the commercialization of the devices, and to achieve this, issues related to the rapid degradation of the perovskite (when compared to the silicon solar cells), the toxicity of components like lead, production cost, material abundance, and others (GIUSTINO; SNAITH, 2016; HE et al., 2021; KE; KANATZIDIS, 2019; SCHILEO; GRANCINI, 2021; YANG et al., 2022), needs to be solved.

Regarding the presence of lead, encapsulation, and recycling may render its presence tolerated. Thus, substituting this element for another is desirable. Alternatives like the tin-based perovskite have been developed. Nevertheless, it does not reach higher efficiency and has even lower stability than the lead-based perovskite, in addition to other limitations (SCHILEO; GRANCINI, 2021).

Concerning stability, several factors are reported as relevant issues. The oxygen, moisture, ambient humidity, temperature, ion migration, and others usually induce the degradation of the perovskite layer(ELSEMAN et al., 2020; HARTONO et al., 2023; KIM; PARK, 2014). The consequence of low stability is usually considered as an initial cause of the hysteresis of the device, which will be discussed in detail later.

Given that this study does not delve into the perovskite layer itself, the optimization aspects of this layer will be only briefly mentioned. Details on perovskite layer optimization are available in the literature(DONG; WANG; LIAO, 2020; KIM et al., 2020; LI et al., 2022; SCHILEO; GRANCINI, 2021).

Concerning the strategies to improve the stability and efficiency of the perovskite absorber layer that consequently originated other materials, change composition (cation/anions) or stoichiometry (bandgap tunning) have been widely explored. Those gave birth to distinct combinations, like the CsFA and triple cation (CsFAMA). Thus, at present, the recording device is a FAPI-based perovskite (MIN et al., 2021).

The substitution of the MA by FA and the addition of the inorganic Cs help to increase mainly the thermal stability. Consequently, the CsFA shows improved stability. However, the photoactive phase control during the deposition of those layers is more complicated, which may result in a slightly inferior efficiency if the process is not well-controlled (DONG; WANG; LIAO, 2020; HE et al., 2021; LI et al., 2022; YANG et al., 2021). On the other hand, the CsFAMA, despite usually showing better efficiency due to superior phase stabilization (over the CsFA), has a quicker and easier crystallization. Thus, this may result in higher density of

grain boundaries and defects, which negatively impact the device's stability (HE et al., 2021; LI et al., 2022; YANG et al., 2021).

Those new materials' composition resulted in an improvement in the efficiency and stability of the devices. The CsFA and CsFAMA were used in this work due to their well-established device production methodology, scientific interest, and optimized performance over the pioneer MAPI.

Another attractive characteristic of the perovskite layers is its versatility concerning the deposition techniques (LI et al., 2021; YANG et al., 2022). The most common is spin coating. Although several other solution routes, mainly scalable ones, like inkjet printing, blade coating, and slot die coating, have been employed (YANG et al., 2022). Also, it is possible to obtain the layer through thermal evaporation.

The perovskite layer were obtained by the spin-coating, which are usually a relatively small area, about 625 mm^2, and show a reliable performance for laboratory. However, it is not scalable. Thus, developing other methods, for example, the slot die coating (SDC) mentioned above, can be considered a future step toward commercialization. Although the perovskite layer is the heart of the device, this layer alone could not reach such efficiency and attention. A combination of other layers is required to achieve an optimal operation of the devices.

In the device, if we overlook the process like recombination and losses, what happens basically is that when an incident photon with proper energy ($\geq Eg$) reaches the absorber layer (in the case of the perovskite), it might be absorbed and generates an electron-hole pair. Subsequently, under the influence of an electric field, the electrons and holes ideally are separated and moved in opposing directions. This process is dependent on factors such as the mobility and lifetime of the charge carriers, as well as charge trapping and recombination (CAI; ZHU, 2021; WÜRFEL; WÜRFEL, 2016).

The separated charge carriers need to be extracted to an external circuit. It is when the transport layers and electrodes show their convenience. Those layers undoubtedly play a fundamental role in the device's performance. Thus, the focus here will be mainly on inorganic metal oxides applied as transport layers. Regarding those layers, one is responsible for the electron transport (usually called electron transport layer – ETL) and the other for the hole (denoted as hole transport layer – HTL). A schematic of the process described in the previous couple of paragraphs is represented in Figure 2.

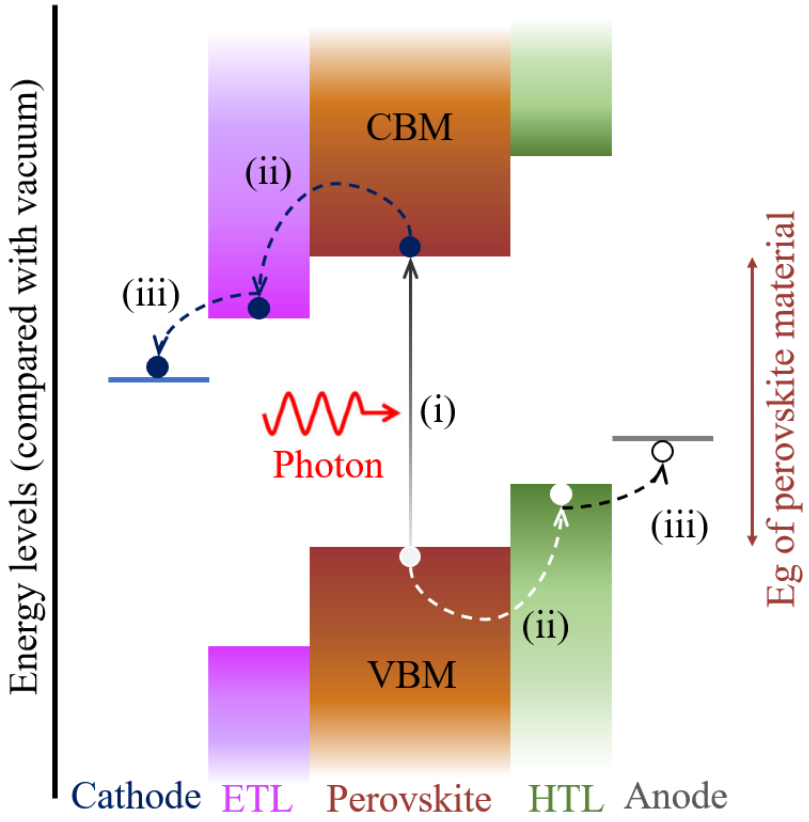

FIGURE 2. Schematic of the charge generation and extraction in the perovskite solar cells. i. Indicates the photon absorption and the electron-hole pair generation. CBM stands for conduction band minimum, and VBM for valence band maximum. ii. Represents the electron transition from the absorber layer to the ETL according to the difference of energy of the CBMs and the hole in the valence band to the HTL. iii. Denotes the transition of the charge carrier from the SL to the electrode. Adapted from (CAI; ZHU, 2021).

The earlier perovskite solar cells were made with the perovskite layer (absorber) placed between the ETL and HTL. In this way, it is possible to separate the devices into two groups, the n-i-p and the p-i-n.

The n-i-p represents the structure where the perovskite (intrinsic semiconductor – i) is on top of an “n” type semiconductor (n-negative) and under the “p” type (p-positive). In addition, devices can also be separated into three most basic configurations: i) the mesoporous; ii) the planar, and; iii) the inverted planar architecture, as represented in Figure 3.

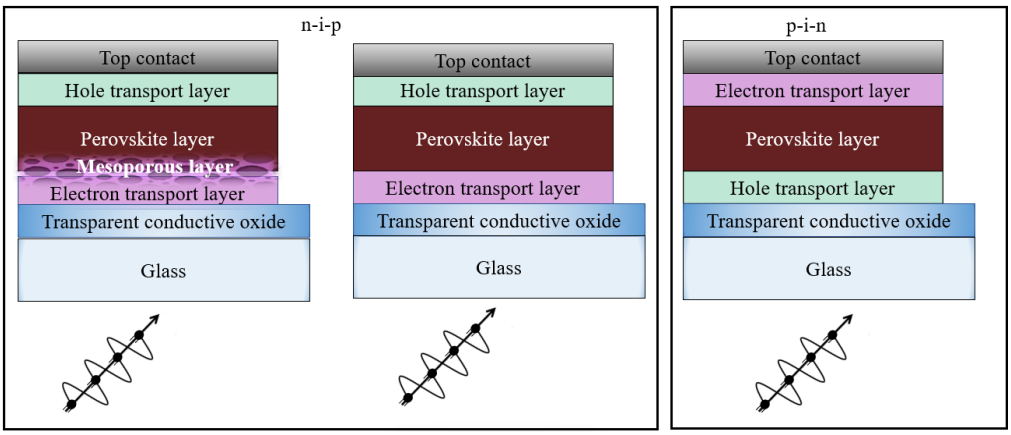

FIGURE 3. Schematic of the three different configurations of the perovskite solar cell. From left to right, the mesoporous and planar n-i-p and the planar p-i-n.

It can be considered that, in most cases, the layers are deposited consecutively on top of a substrate, which is a glass slide coated with a transparent conductive oxide (TCO) that will play the whole of a bottom contact. Nowadays, the FTO (fluorine-doped tin oxide – SnO_2:F) and the ITO (indium tin oxide - $InSnO_2$) are frequently used as TCO. However, other materials have also been explored, such as the IZO (indium zinc oxide) and AZO (aluminum-doped zinc oxide) (CAI; ZHU, 2021).

In general, the commercialized FTO and ITO have similar characteristics, being possible to acquire both with the sheet resistance from 7 to 15 Ω/sq and transmittance over 80 % in wavelength above 400 nm. On the other hand, the FTO bears higher temperatures for annealing. Meanwhile, the ITO has a smooth surface. It is important to note that when a substrate is cited in this work, it will refer to the set glass and TCO.

Considering the three architectures, what differentiates them is how the layers are stacked on top of the substrate. In the mesoporous architecture, on top of the TCO (electrode) goes a compact electron transport (selective) layer, followed by a mesoporous layer, typically titanium dioxide (TiO_2). Then, the perovskite layer, the hole transport (selective) layer, and a top contact (electrode). The presence of the mesoporous layer increases the surface area interaction between the absorber and transport layer, consequently improving the charge transfer.

In the case of the planar device, the main difference is that the mesoporous layer is dismissed, leaving only the compact layers. Although the mesoporous may increase the surface area for charge transfer, it can have the disadvantage of increasing the losses due to recombination at the interface. In this way, the planar devices have the advantage, considering

a flat and compact layer, of decreasing losses at the interface. In addition, one layer less to deposit can be advantageous in industrial productions.

Notwithstanding, the compact layer may also be propitious for the perovskite to crystalize in larger grains, reducing the grains boundaries, which is favorable for the charge transport, especially when the grains grow more uniform in the perpendicular direction considering the electrodes. In addition, to lower interfacial recombination losses, the strategy of the surface passivation between the perovskite and the SL has often been investigated and will be explored in this work.

Initially, planar devices were made using the TiO_2, although it was noted that the TiO_2 presented considerable photocatalytic activity under ultraviolet light illumination, which induced the degradation of the perovskite layer(ALTINKAYA et al., 2021; IM et al., 2011; KOJIMA et al., 2009; LEE et al., 2012). Other materials emerged as potential alternatives to mitigate the problem. Common choices, like tin dioxide (SnO_2) and zinc oxide (ZnO), were employed. In addition, niobium pentoxide (Nb_2O_5) was found to be a viable alternative (CAI; ZHU, 2021; ELSEMAN et al., 2020; FERNANDES et al., 2016, 2019, 2022; LIN et al., 2021; SHEN et al., 2018).

The SnO_2 is extensively used and presently holds the efficiency record in this group of solar cells (MIN et al., 2021). Another material that has been gaining attention is the Nb_2O_5. However, the n-i-p planar devices using Nb_2O_5 as ETL do not reach efficiency as high as the ones with SnO_2 yet. Nevertheless, the Nb_2O_5 can surpass the efficiency of the TiO_2-based devices and shows improved stability. Both materials were explored in this work and will be discussed in more detail in upcoming topics.

Still considering the n-i-p devices, in both mesoporous and planar ones, following the stack: substrate (glass + FTO), ETL, and perovskite, it comes next to the HTL. The pioneer HTL that is still massively utilized is the Spiro-OMeTAD. Despite its high popularity, the Spiro-OMeTAD, as an organic layer, also jeopardizes the stability of the devices (HAN et al., 2022; KIM et al., 2020; YANG et al., 2022). Other alternatives have been used as ETL in the n-i-p devices, such as P3HT and PTAA, thus still not surpassing the Spiro-OMeTAD. Finally, at the end (top of the stack) is the top contact, which is a metal, frequently gold (KIM et al., 2020).

Regarding the planar p-i-n device, the difference (compared with the planar n-i-p) is, the fact that the HTL comes on top of the substrate and under the perovskite solar cell. The stack is then followed by the ETL, after (on top of) the perovskite layer, and finalized by the metal contact. In addition, different materials are often used to make the device feasible.

In the inverted structure, as HTL, the organic PEDOT: PSS was the first to be used. Nowadays, it is widely employed the self-assembled monolayers (SAM) and inorganic materials, such as nickel oxide (NiO_x), Copper Oxide (CuO_x), and Cobalt Oxide (CoO_x) (GIL et al., 2019; SHALAN et al., 2016). Considering the ETL used in the inverted structure, fullerene based like PCBM and C_{60} are the most common. In addition, interfacial layer utilization, such as bathocuproine (BCP) and polyethyleneimine ethoxylated (PEIE), proved to enhance the charge extraction and, consequently, the device performance. For the top contact, copper and silver are usually thermally evaporated (KIM et al., 2020).

The reason that limits the usage of certain materials is the processing conditions to obtain the layer. For example, the TiO_2 is unsuitable for ETL in the p-i-n devices because it requires a high processing temperature. Although the SnO_2, deposited by ALD (atomic layer deposition), can be used as an interlayer on top of the C_{60} in the p-i-n configuration (KIM et al., 2020).

Hence, the decision among types of solar cell structure and materials relies on specific objectives. The p-i-n structure usually shows better stability and negligible hysteresis. On the other hand, higher efficiency can be achieved with the n-i-p structure. If the objective involves investigating an ETL requiring high process temperature or energetic deposition methods, the n-i-p is more suitable. It is essential to note that both types exhibit distinct complexities and phenomena that need understanding.

1.2 Transport layers

The transport layers stack define more problems and complexity regarding the device fabrication and operation, lighting relevant questions. What are the remarkable characteristics of a material to fulfill this role? How to choose suitable materials for those layers in each case (device configuration)? How is the interaction, and what do those layers cause to the perovskite? Some characteristics can be analyzed as a first approach for those questions, and they may be used as preconditions to select potential materials.

Some requirements are that the layer, preferably, must be: i) highly transparent (at least the one preceding the perovskite) in the visible range to avoid optical losses and guarantee that the light will reach the perovskite layer; ii) homogeneous and pinhole-free surfaces, once the previous layer will influence the perovskite growth and crystallization. In addition, good coverage is significant to avoid current leakage (losses) between the perovskite and the

electrodes; iii) a good match of energy levels (alignment of energy levels between the adjacent layers) to promote a favorable charge transfer; iv) high mobility of one charge carrier (either electrons or holes), and consequently, a blocking capability of the other one (ELSEMAN et al., 2020; KIM et al., 2020; LIN et al., 2021).

Many inorganic metal oxides, like semiconductors, can fulfill those criteria. In addition to their stability as inorganic materials, those metal oxides are widely used and, nowadays, shown as candidates with high potential to be fundamental parts of the devices. For those reasons, and as mentioned before, the investigation of those layers will be the focus of this thesis.

Mainly, this study aims to investigate the performance and impact of niobium pentoxide as an ETL deposited using a slot die coating. This approach is chosen based on the proven potential of Nb_2O_5 when applied through alternative techniques in perovskite solar cells. Additionally, the study will delve into the interface passivation of the tin oxide layer in planar devices.

1.2.1 Niobium Oxide

The niobium oxide is nowadays widely used in many different technologies. It can be employed in batteries, capacitors, and photovoltaic devices, which is the case of this work (FERNANDES et al., 2019; GRIFFITH et al., 2021; NICO; MONTEIRO; GRAÇA, 2016). In the perovskite solar cells, the niobium oxide, mainly in the Nb_2O_5 stoichiometry, is used as the electron transport layer, sometimes also cited as hole blocking layer, for n-i-p devices. The main advantage of this n-type semiconductor over the traditional titanium dioxide layer is its improved chemical stability, considering that the TiO_2 has a substantial photocatalytic activity in the ultraviolet that impacts the device stability (FERNANDES et al., 2019; KIM et al., 2020; SHEN et al., 2018).

Other properties of the Nb_2O_5, like energy level alignment, band gap, and optical characteristics, are comparable to the TiO_2, which makes this metal oxide suitable as an ETL. Its band gap is reported to be about 3.4 – 3.6 eV(FERNANDES et al., 2016; LEMOS et al., 2023; NICO; MONTEIRO; GRAÇA, 2016). However, the conduction band minimum of the Nb_2O_5 is slightly inferior in energy than the TiO_2, which is an additional advantage for this oxide usage (FERNANDES et al., 2016; FU et al., 2018; WANG et al., 2019a), as illustrate on Figure 4. Hence, this may indicate a better capacity to extract the electrons or block the holes.

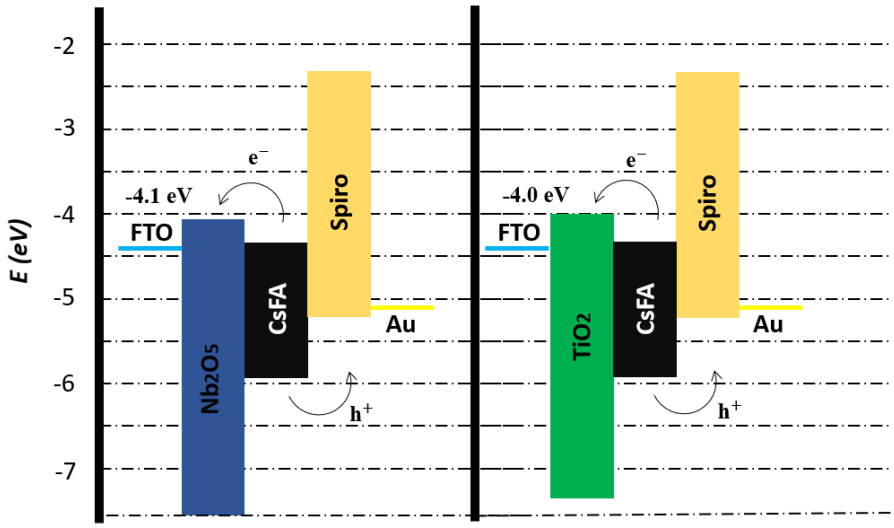

FIGURE 4. Comparison between the Nb_2O_5 and TiO_2 energies level on the perovskite solar cells. Adapted from(FERNANDES et al., 2016; FU et al., 2018)

In addition, this layer can be obtained by distinct deposition techniques. The most common are spin coating, atomic layer deposition, and reactive sputtering. For the spin coating, it is reported efficiency of 19.2 % by SHEN et al., (2018). WANG et al., (2019) reached 20.22 % using spin coated Nb_2O_5 nanoparticle. CHAVAN et al., (2021) reported an efficiency of 21.04 % when using the Nb_2O_5 deposited by ALD as a buffer layer. Meanwhile, for sputtering (FERNANDES et al., 2022) reported an efficiency of 18.6 % in the single-junction perovskite solar cells, and AYDIN et al., (2021) even successfully applied the layer in multijunction, i.e., TADEM solar cells, reaching even further efficiencies. In addition, LIU et al., (2019) reported the compact layer deposited by electron beam with devices reaching am efficiency of 19 %.

So far, no report on Nb_2O_5 deposited by slot die coating then applied as ETL in the perovskite solar cells was found. Thus, to bring together the advantages previously mentioned of the slot die coating technique and the suitability of the niobium pentoxide, it was tested in this work to coat and apply the Nb_2O_5 as ETL in the perovskite solar cells.

1.2.2 Tin oxide and the potassium chloride passivation

Among the metal oxides for electron transport layers, despite the titanium dioxide, nowadays, tin dioxide is an n-type semiconductors often used in perovskite solar cells. Besides the fact that the SnO_2 is a well-known material that matches the fundamental requirements of an ETL, i.e., optical transparency, band alignment with the perovskite, high electron mobility,

wide bandgap, etc., several reports highlight its advantages in the versatility to produce and apply this layer instead of the TiO_2 (ALTINKAYA et al., 2021; MIN et al., 2021; PARK; ZHU, 2022).

The SnO_2 allows low processing temperatures, in addition to being a relatively simple layer to deposit by different techniques and does not require the mesoporous layer as the TiO_2-based devices usually do, which emphasizes the suitability of the material (DAGAR et al., 2019; JIANG et al., 2019; MIN et al., 2021; PARK; ZHU, 2022). Despite the promising results reported, with devices reaching over 20 % efficiency, the n-i-p devices developed with the SnO_2 as ETL still show a non-negligible hysteresis, which represents the discrepancy between the forward and reverse scans in current density against voltage measurements (J-V curves).

The hysteresis is often addressed to problems in the charge extraction, for example, due to accumulation or recombination on the interface and ion migration (DAGAR et al., 2019; UNGER et al., 2014, 2020), thus representing a limitation for those perovskite solar cells once it indicates reduced operational stability. Different strategies have been employed to mitigate this effect. Using interface modifiers between the transport and perovskite layers or adding additives to the perovskite layer is among the prominent ways to reduce the hysteresis on n-i-p devices. Reports show that alkaline metals and salts used as additives and interface modifiers proved beneficial and enhanced the perovskite solar cells' performance, especially concerning hysteresis (DAGAR et al., 2019; JIANG et al., 2019).

In this way, exploiting the role of potassium chloride (KCl) addition was also tested in this work, which was done using n-i-p devices with planar architecture. The SnO_2 was used as ETL once it can be considered a good and well-established standard layer due to its previously mentioned characteristics. The perovskite used was the triple cation - CsFAMA. The KCl was applied either as an interface modifier, a separated layer between the SnO_2 and the perovskite, or as an additive, being mixed with the perovskite precursor solution.

1.3 Data overview

An overview of the materials and techniques investigated in this work is presented in Table 1. The bold letters are related to the results presented in this report.

TABLE 1. Index of materials, depositions, and characterization techniques utilized. However, only part of them will be presented in the thesis. AFM stands for atomic force microscopy, XRD for X-ray diffraction, UVVis for ultraviolet-visible spectroscopy, XPS for X-ray spectroscopy, UPS for ultraviolet spectroscopy, SPV for surface photo voltage, SEM for scanning electrons microscopy, TrAMPPT for Transient analysis during maximum power point tracking and, EQE for external quantum efficiency.

Metal oxides				
CoO	**Nb_2O_5**		**SnO_2**	
Depositions				
Sputtering	Sputtering	**Slot Die**	**Spin Coating**	Slot Die
Application				
MAPI	CsFA	**CsFA**	**KCl + CsFAMA**	CsFA
Characterizations				
AFM	XPS	**Laser Microscopy**	**J-V**	Laser Microscopy
XRD	UPS	**SEM**	**SEM**	SEM
UVVis	SPV	**J-V**	**EQE**	J-V
XPS		**TrAMPPT**		
UPS				
J-V				

The results related to the niobium pentoxide (Nb_2O_5) deposited by slot die coating and applied as electron transport layers (ETL) in the perovskite solar cells will be discussed in this thesis. In addition, the potassium chloride (KCl) as an interface modifier for n-i-p devices using tin oxide (SnO_2) as a transport layer will be described.

The slot die-coated Nb_2O_5 was chosen due to the potential and importance of this material, being the center of the collaboration between the Brazilian and German groups (Laboratório de Filmes Semiconductors, Unesp – Bauru and Solution Processes for Hybrid Materials and Devices, Helmholtz Zentrum Berlin), linked with this research. In addition, slot die coating is a promising technique for the scalability of devices, which is one of the relevant topics among the community for the perovskite solar cell. Notwithstanding, no report that has combined this material and technique could be found so far.

Although the KCl seems to deviate from the metal oxide as the main topic of the thesis, it is a topic of interest concerning the work developed during the research stay and resulted in

a complete data set. Moreover, the KCl addition can still be considered related to the metal oxides layer since this may affect the interface and charge extraction, therefore improving the performance when used as an interface modifier (between the metal oxide – ETL – and the perovskite layer) for the n-i-p devices. Those are the reasons for choosing to report this topic here.

Currently, it is intended to present the other results and discussion of the subjects mentioned above in future works. The complexity of this additional data requires further study and understanding to ensure a precise and coherent analysis and conclusion, which could not be accomplished within the current timeframe.

2. Techniques and methodologies

The upcoming topics will describe the basics of the slot die coating process, followed by the preparation procedure for each layer necessary for the perovskite solar cell. In the sequence, the bases of the characterization techniques used in this work will be described together with the details of the measurements.

2.1 Device Fabrication

The slot die coating of the niobium pentoxide layer, and its solution preparation was performed at the Printing Laboratory of the Integrative Research Institute for the Sciences IRIS Adlershof of the Humboldt-Universität zu Berlin. Meanwhile, the perovskite layer preparation and all other layers were carried out at the Helmholtz Innovation Lab HySPRINT of the Helmholtz-Zentrum Berlin, Adlershof.

2.1.1 Slot Die Coating and the perovskite layer

The slot die coating (SDC) is considered one of the most, if not the most, promising solution-based methods for high throughput thin film manufacturing. The suitability to the laboratory and industrial scale, through its potential in printing in a wide variety of lengths and widths, guarantees its advantage when compared with other techniques, such as spin coating, that lack the capability to scale. Moreover, the solution loss is quite minimal, and the SDC allows the coating of thin and homogeneous layers over the deposition area and in a variety of substrates.

However, it is quite complex to achieve good-quality coating. For this, it is necessary to tune the substrate speed, solution flow rate, solution viscosity, and the distance to which the solution will be applied. Other approaches are also possible, aiming to improve the coating quality, like adding an air knife blower or preheating the substrate. The system (from FOM Technologies©) used in this work can be seen in Figure 5.

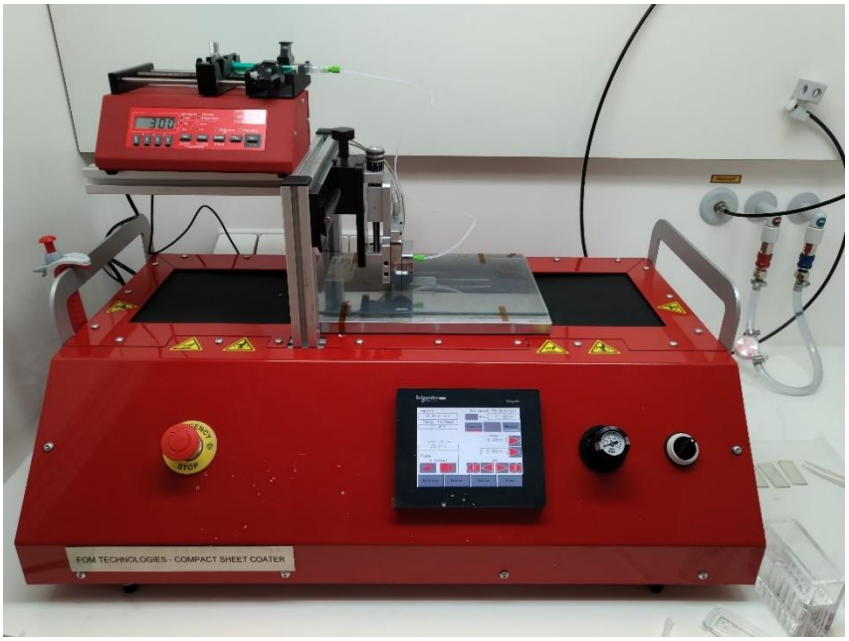

FIGURE 5. Slot die system from FOM Technologies used to coating the metal oxide layers at Humboldt-Universität zu Berlin.

Although great efforts to obtain the perovskite layer using this technique are heading to improvements in the devices and their scalability, the application of the SDC process for other materials and layers, such as the charge transport layer, is also important and can lead to a step closer to the commercialization. Furthermore, it may become popular to produce other materials, such as metal oxides, applied in different thin film technologies, like batteries and photocatalysis, that the high throughput can be beneficial.

The SDC process consists of spreading a solution or ink (the coating material) over a surface (substrate). The solution is usually pumped and applied on the top of the substrate through the slot die head, which is positioned slightly above the substrate, as illustrate in Figure 6.

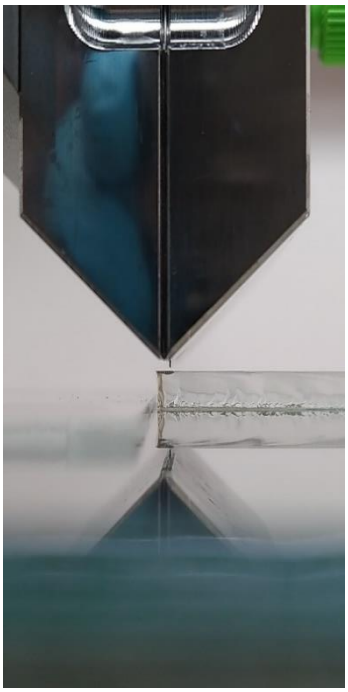

FIGURE 6. Slot die coating head positioned on top of the substrate right before starting the Nb2O5 coating, illustrating the gap between blade and substrate surface.

When the solution reaches the surface, it forms a meniscus that depends on the viscosity and the head-substrate distance, and it is one of the keys to control the process and achieving an ideal coating. Then, the substrate moves toward the head, according to the web speed, and the solution is spread, forming the coating. After the solvent evaporates, it results in a thin layer or film. A schematic illustration of the process is shown in Figure 7.

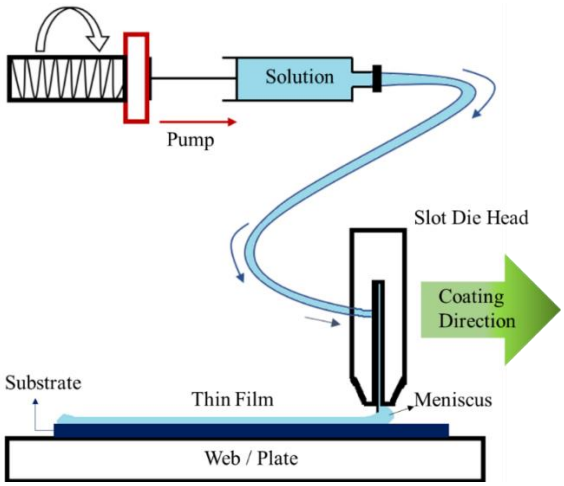

FIGURE 7. Schematic of the slot die coating process. The figure represents the main parts such as the solution dispenser, the slot die head, meniscus, and the plate.

Despite the solution viscosity, which can be controlled by changing the precursor solution concentration (C), web speed (WS), which is related to the velocity that the substrate moves towards the blade located at the end of the head, and the pump rate (PR), which influences the solution flow rate through the slot die head, are relevant parameters that will mainly affect the thickness of the films (DING; LIU; HARRIS, 2016; PATIDAR et al., 2020). In addition, it is a fair estimation to expect that the ratio between PR and WS affects the wet film thickness (h_w), according to Equations 1a and b, and, therefore, the dry film thickness (h_d) (DING; LIU; HARRIS, 2016; RICHARDS et al., 2022).

$$h_w = \frac{PR}{wWS} \quad \text{Eq (1a)}$$

$$h_d = \frac{PR}{wWS} x \frac{C}{\rho} \quad \text{Eq (1b)}$$

According to the equation, the coating width (w), and density of the material (ρ) also influence the thickness. Although equation 1 can be considered a good approach (DING; LIU; HARRIS, 2016; RICHARDS et al., 2022), more careful consideration concerning fundamental aspects of the fluid dynamic, according to discussions explored in other works presented in the literature, must be considered.

Carvalho and Kheshgi (CARVALHO; KHESHGI, 2000), based on the theory developed by Landau and Levitch (LANDAU; LEVICH, 1988) and later predictions from Ruschak (RUSCHAK, 1976), used a viscocapillary model to report a systematic study investigating operational limits of the slot die coating process. On their predictions, distinct coating operation regions can be achieved according to the balance of the fluid pressures between the head and the substrate surface (which rely on the coating parameters and head geometry) and the precursor solution characteristics (especially the viscosity).

The operation regions, or coating window, define conditions necessary to obtain potential regions for a defect-free coating. Despite the pump rate and the web speed, those regions are strongly affected by the gap between the slot die head and the substrate surface (H_0), in addition to a Capillary number (Ca), which is related to the solution viscosity (μ) and surface tension (σ). Changes in those parameters will affect not only the film thickness (h) but also the quality of the coating related to defects such as rubbing, stripes, rivulets, and air (DING; LIU; HARRIS, 2016; LI et al., 2023; LIN et al., 2010; PATIDAR et al., 2020; SEONG et al., 2016).

According to Equation 2, it is possible to establish the coating windows and estimate, based on the coating parameters, the possible regions where the coating was performed (CARVALHO; KHESHGI, 2000; CHANG et al., 2007; RICHARDS et al., 2022).

$$Ca = \frac{\mu V}{\sigma} = 0.65 \left(\frac{2}{\frac{H_0}{h} - 1} \right)^{\frac{3}{2}} \quad \text{Eq (2)}$$

One of the purposes of this subtopic was to control the thickness and achieve good coverage of the metal oxide layer on top of the FTO coated glass. For the coating, different web speeds and pump rates were tested. The values used for each parameter were combined as presented in Table 2.

TABLE 2. Different parameters used in the slot die process to investigate the metal oxide layer deposition.

Slot die coating parameters	
Web speed (cm/min)	**Pump rate (µL/min)**
25	60
	120
	300
75	60
	120
	300
125	60
	120
	300

Those parameters were used to investigate the coating of the Nb_2O_5 to later apply as the electron transport layer, in the perovskite solar cells.

To accomplish this goal, the Nb_2O_5 was coated on top of FTO. The FTO had 25 x 25 mm, with sheet resistance of 15 Ω/sq and patterned to form six smaller or sub-cells. Before the deposition, the substrates were cleaned with an ultrasonic bath in deionized water mixed with Mucasol® 9:1, then just deionized water, following acetone and isopropanol alcohol, each part left for 10 minutes. Then, the substrates were dried using a nitrogen gun and, finally, an ultraviolet ozone cleaning for 15 minutes.

The Nb_2O_5 precursor solution was prepared using 12.5 µL of niobium ethoxide per mL of ethanol. After mixing both, 20 µL of hydrochloride acid was added to help the stabilization. The procedure was previously reported for the spin coat (FERNANDES et al., 2022; GARCIA, 2022; SHEN et al., 2018). The solution was left stirring without temperature for at least 2 hours.

The solution preparation and the coating process of the Nb_2O_5 was performed inside a fume hood. The coating was followed by different steps of annealing, first at 100 ºC for 10 minutes, then 150 ºC for 30 min, 370 ºC for 30 min, and 550 ºC for 1 hour, all steps with a heating rate of 5 ºC/min. Finally, it was left for a few hours at 70 ºC to cool down smoothly.

Cesium formamidine lead halide perovskite, also known as double cations mixed halide or CsFA and denoted by $Cs_{0.17}FA_{0.83}Pb(I_{0.83}Br_{0.17})_3$, was deposited by spin coat as an active layer for the investigation of the devices based on the slot die coated Nb_2O_5. All the preparations related to the perovskite layer were performed inside gloveboxes with nitrogen atmosphere.

The precursor solution was prepared with 57.42 mg of cesium iodide (CsI), 121.66 mg of lead bromide ($PbBr_2$), 185.56 mg of formamidinium iodide (FAI), and 446.49 mg of Lead iodide (PbI_2), together. Then, it was mixed 1 mL of DFM: DMSO (dimethylformamide: dimethyl sulfoxide) in the proportion of 4:1 v/v. The solution was stirred for a minimum of 2 hours and, afterwards, filtered with a 0.45 µm syringe. For the deposition, 100 µL of the perovskite precursor solution was spin-coated for 35 seconds at 3500 rpm, with 250 µL of anisole dropped at 30 seconds. In sequence, the samples were annealed for 30 min at 100 ºC. The results are shown in Section 3.1.

2.1.2 Spin coated tin oxide and the perovskite layer

The SnO_2 layer was deposited by spin coated following a preview report (DAGAR et al., 2019) on top of ITO substrates, analogous to the FTO described in the previous section, including the cleaning process. The SnO_2 (from Sigma-Aldrich) was prepared inside a laminar flow fume hood.

A precursor solution was prepared mixing 22.56 mg of tin chloride per mL of ethanol. It was left stirring overnight without heating. Then, the solution was spin-coated in two steps using 150 µL each, first at 1500 rpm, followed by 2500 rpm, both steps for 30 seconds. Finally, a small area on two parallel sides of the substrates was cleaned with ethanol to expose the back contact (ITO substrate), and the samples were annealed for 1 hour at 180 ºC.

The samples were then separated into three different groups. One as standard (only SnO_2, no KCl). The other one with the KCl as a passivation layer deposited on top of the SnO_2, resulting in a KCl layer sandwiched between the SnO_2 and the perovskite layer. Then, the last was with the KCl mixed in the perovskite precursor solution, acting like an additive.

For the KCl layer preparation, 2.5 mg of KCl was dissolved in 1 mL of deionized water and then left to stir for 10 minutes. The solution was then deposited on top of the SnO_2 film, also by spin coating, using 300 µL and 4000 rpm for 30 seconds, followed by the annealing at 120 ºC for 10 minutes, to the solvent evaporation. Those samples are related to the KCl as the passivation layer.

Regarding the third group of samples that uses KCl as an additive in the perovskite, it was prepared using different concentrations of salt mixed in the perovskite solution. The mixed cation perovskite, also designated triple cation and denoted as $FA_{0.79}MA_{0.16}Cs_{0.05}Pb(I_{0.83}Br_{0.17})_3$, was prepared as described below.

It was weighted 19.49 mg of cesium iodide (CsI), 27.13 mg of methylammonium bromide (MABr), 203.40 of formamidine iodide (FAI), lead bromide ($PbBr_2$) 96.91 mg and lead iodide (PbI_2) 594.33 mg. After the weight, 1 mL of a mix of DMF and DMSO, consisting of 0.8 mL of DMF and 0.2 mL of DMSO, was mixed. Then, the solution was left to stir for 1.5 hours at 60 ºC. Afterward, it was separated into four different vials, where one was left just with the perovskite solution, the other three were separately added 1.0, 1.5, and 2.5 mg of KCl in each mL of perovskite, then again left for stir overnight at 60 ºC.

Some remarks are worth mentioning. First, although it was detailed the amount of 1 mL of perovskite solution, it was produced enough to use the same solution to spin coating the layer on the reference, on the KCl layer, and to mix with the different concentrations. The perovskite was prepared inside a glovebox with a nitrogen atmosphere, including the mixing with the KCl. However, the KCl and SnO_2 layers were prepared outside in an ambient atmosphere. In addition, two hours was expected to be the ideal for the perovskite to dissolve. However, it was necessary to leave it overnight to dissolve the KCl, which might harm the layer formation and, consequently, the device's performance.

After that, the perovskite solution, either without the KCl additive or with it, was spin-coated at 3500 rpm for 35 seconds on top of the ETL. It was used 100 µL of the perovskite solution per sample, and at 25 seconds it was dropped 500 µL of ethyl acetate as an antisolvent. After the depositions, the samples were annealed on a hot plate at 100 ºC for 20 min. Then, the samples are ready to proceed with the other steps to finalize the devices. This procedure was also performed inside a glove box.

Despite that, the HTL and the metal contact used were the traditional ones: Spiro-OMeTAD and gold. It is worth mentioning that it was used for standard comparison, devices

without modification (no KCl added in any way, prepared only the ITO, SnO_2, Perovskite, Spiro-OMeTAD, and gold). The results of those analyses are discussed in the following topics.

2.1.3 Spiro-OMeTAD as hole transport layer

For all the batches prepared, it was adopted the same procedure for the Spiro-OMeTAD preparation and deposition. It was also prepared inside a glovebox and deposited by spin coating. For the solution, it was necessary to prepare some dopants beforehand.

In separated vials, 300 mg of FK209 (cobalt dopant), 520 mg of Li-TFSI (lithium dopant), and 36.15 mg of Spiro-OMeTAD were weighted. The FK209 and Li-TFSI were then mixed with 1 mL of acetonitrile each and left to stir for 30 min without temperature. The Spiro-OMeTAD was mixed, only sometime before the deposition, with 1 mL of chlorobenzene. It was then left to stir for around 10 min. The dopants were then added to the Spiro-OMeTAD solution, following 14.4 µL of TBP (4-Tert-Butylpyridine), 14.6 µL of FK209 solution, and 8.8 µL of the Li-TFSI solution. Finally, it was stirred for 15-30 min right before the deposition.

The Spiro-OMeTAD was deposited on top of the freshly prepared perovskite. It is important to note that it was necessary to anneal the perovskite layer, so it waited around 15 min for the sample to cool down before proceeding. Moreover, the perovskite layer and the Spiro-OMeTAD layer were deposited in different gloveboxes connected by an antechamber, so the samples were not exposed to the air during those depositions.

For the spin coating, it was used 1800 rpm for 32 seconds. Approximately three seconds after the beginning of the spin, 100 µL of the solution was dropped on top of the sample. After the layer deposition, the samples were transferred to an oxygen box with controlled humidity (~3%) and left overnight to promote the oxidation of the Spiro-OMeTAD layer. A picture of one sample is shown in Figure 8.

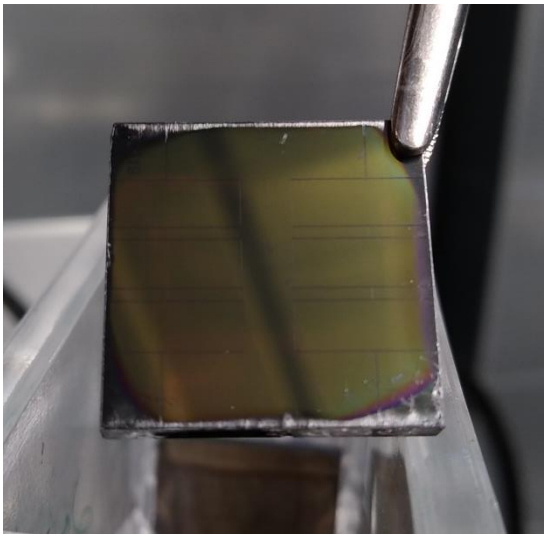

FIGURE 8. Photo of the sample after the deposition of the Spiro-OMeTAD layer. It is possible to note the pattern from the substrate (the narrow line separation).

2.1.4 Rear electrode evaporation

To proceed with the device preparation, after the Spiro-OMeTAD layer, the gold contact was deposited by thermal evaporation as the top electrode (the evaporator chamber was also inside another glovebox). For all the samples, the same automatic procedure was used. One hundred nanometers of gold was evaporated at a rate of 1.0 Å/s. A mask, like the one in Figure 9, was used to match the pattern of the TCO. After the evaporation, the sides of the sample were scratched with a small blade to expose the back contact. The completed sample can also be seen in Figure 9.

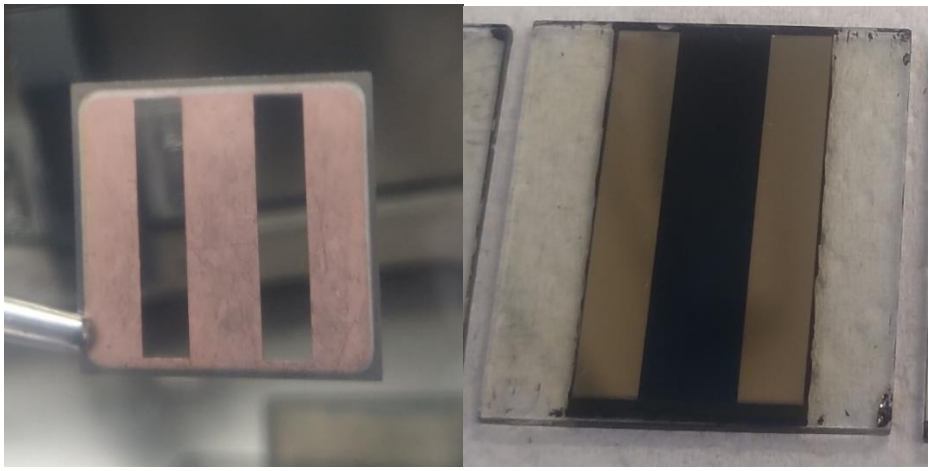

FIGURE 9. On the left is the mask used for the gold evaporation. On the right is the finished sample. The connection between the gold and the pattern of the FTO defines the active area of a pixel or cell.

2.2 Characterization

2.2.1 Confocal laser microscopy

Confocal microscopy or confocal laser scanning microscopy is a non-destructive technique used to analyze specific areas precisely in the order of micrometers on the surface of materials. This technique allows obtaining images of the surface of samples, usually without harming them, which permits easy access to information such as the surface morphology, roughness, and even thickness of samples.

In a very simple way, the operation of the confocal microscope consists of an incident light beam, focused by a set of lenses, that reaches a localized point in the surface of a sample. This light beam is then reflected towards a pinhole that sets the incident light from the focus point. The selected light reaches the photomultipliers, which generate a signal that will be converted by the computer into images of the surface area. The schematic of the microscope is represented in Figure 10.

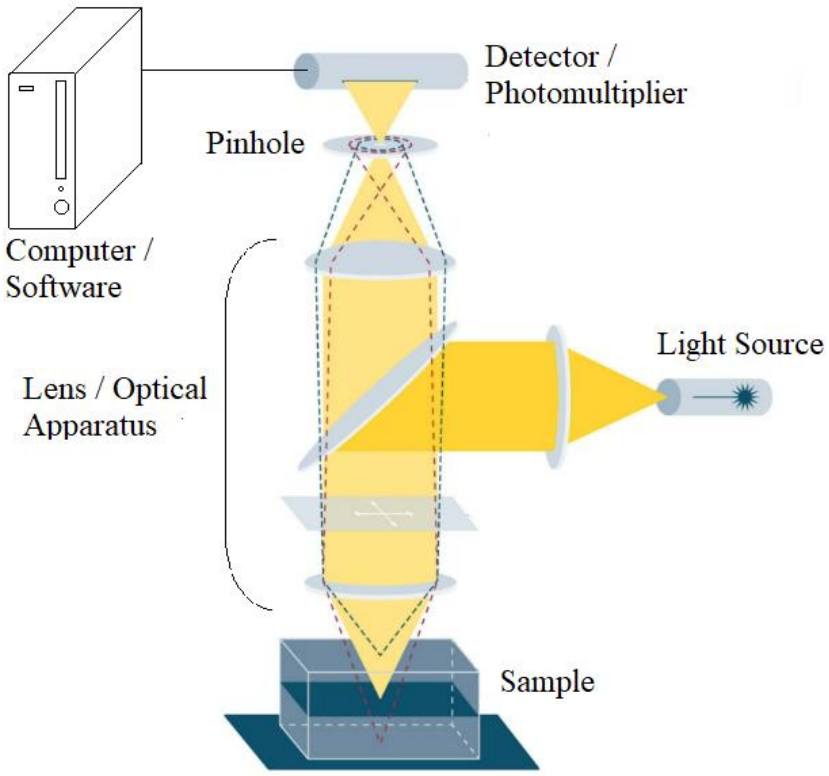

FIGURE 10. Schematic of the confocal microscope. Adapted from: ("ZEISS LSM 900 - Confocal for Materials Research", 2023).

Although confocal microscopy can be useful in general surface analysis, it has some limitations related to the wavelength and equipment optics that cap the resolution to usually a few micrometers and, in the best case, several nanometers.

The measurements were performed with a LEXT OLS4100 at the Integrative Research Institute for the Sciences (IRIS Adlershof) of the Humboldt-Universität zu Berlin. An area of 644x644 from the different metal oxide layers' surfaces was measured in µm using a 20x magnification lens and a 405 nm laser to analyze its coverage and in search of quantifying the pinholes in the sample surface. Figure 11a shows an example of measurements. Different points of the sample were scanned, forming a 5x5 matrix. Each generated image was then compiled by a Python code (written by Dr. Edgar Nandayapa). With the size and brightness tunning, the program identifies potential pinholes in the sample surface, as shown in Figure 11b.

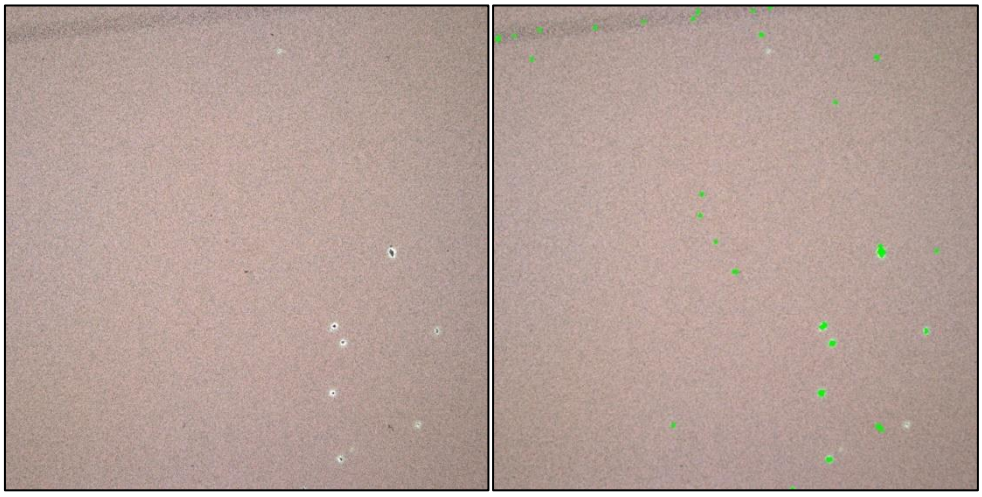

FIGURE 11. a) Image from the confocal microscopy of the niobium pentoxide coated on the FTO-glass substrate and b) after the pinhole analysis. The green area indicates the potential pinhole identified by the code

The code provides an estimate of the counts (number) and area of potential pinholes, and a collage with all images is generated at the end. The number of pinholes for each analyzed sample will be detailed in section 3.1.1, and individual images of each scanned area can be found in the supplementary data.

2.2.2 Scanning electron microscopy

Scanning electron microscopy (SEM) is a powerful imaging technique extensively used to analyze the microstructures, compositions, thickness (in the case of cross-section images),

and other characteristics that extend from the surface through the bulk of a wide variety of samples and in ranges down to few nanometers.

The SEM consists of an electron beam, usually originated either by electrons emitted from a thermionic emission of a filament (commonly made of tungsten) or by a field emission gun. The electron beam is focalized into a specific point of the samples through a series of electromagnetic lenses, hitting the designed area and interacting with the sample atoms.

The interaction may result in several electron and/or photon emissions, and the analysis depends on which of those emissions will be collected (selected by the detector that is used) as output. Some of the possible emissions are represented in Figure 12. Secondary electrons (SE), backscattered electrons (BSEs), and energy-dispersive X-rays (EDX) are usually the most common techniques.

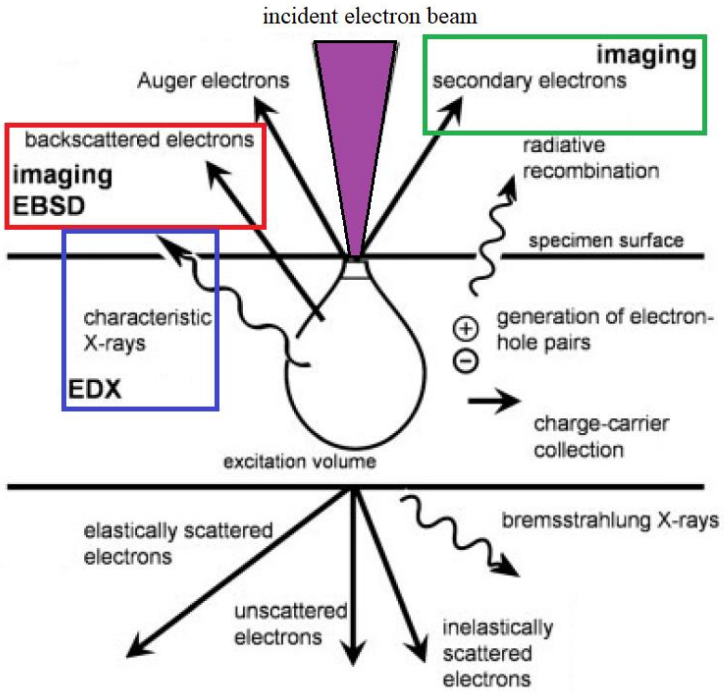

FIGURE 12. The schematic of the possible emissions resulted from the interaction of the electron beam with the sample in the SEM. Adapted from (ABOU-RAS; KIRCHARTZ; RAU, 2011).

The SE and BSEs, in a simple way, are image techniques that will provide information mainly from the morphology with different contrasts of the specimen. The SE collects electrons with lower energy, small angles (regarding the beam), and shallow regions of the sample, and the detector is frequently positioned surrounding the microscope column. On the other hand, for the BSEs, the detector is usually placed aside, and it collects electrons with higher energy in deeper regions and at higher angles from the primary electron beam. Meanwhile, for the

EDX, typically, a separated detector is necessary, and it allows the estimation of the composition of the samples through the detection of the characteristic energy emitted by each element. It is worth mentioning that a series of aspects, from the sample preparation to the measurement adjustments, shall be considered for a good analysis and a correct interpretation of the data.

The samples in conventional SEM systems are loaded in a vacuum, which most of the time limits it to samples that are not sensitive to vacuum. The high energy of the beam during the measurement can also damage the sample. For cross-section measurements, a perpendicular clean cut is necessary, and an incorrect angulation of the sample can mislead the interpretation.

During the measurement, a charge effect may occur due to the high incidence of electrons. To mitigate this effect, it is necessary to provide a way to discharge. For conductive samples, this can be achieved through the connection with the stub (sample holder). In the case of samples with poor or no conductivity, a thin metal layer can be deposited on the top of the sample to facilitate discharge.

Additionally, the work distance, alignments (apertures), acceleration voltage, and electron beam current are some of the parameters necessary to adjust for an optimized sample analysis. The acceleration voltage is related to the energy of the incident electron beam and defines the penetration depth, which also depends on the material. Meanwhile, the electron beam current affects the rate of incident electrons in the sample.

In this work, the SEM surface and cross sections measurements were mainly performed in a Zeiss Gemini SEM 500, hosted by the Structure Research and Electron Microscopy group at the Humboldt-Universität zu Berlin IRIS – Adlershof and with the help of the technician Ms. Carola Klimm. The parameters used for each measurement can be found in the respective image, as exemplified in Figure 13.

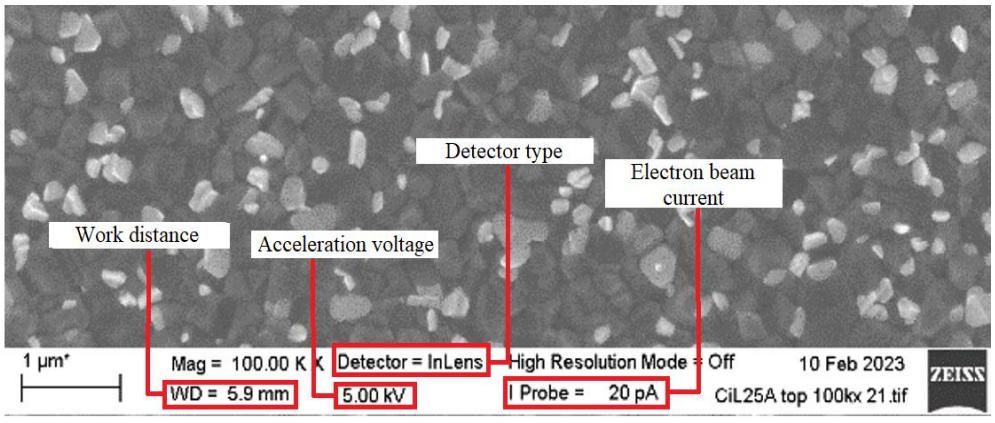

FIGURE 13. Indication of SEM parameters. Image from the perovskite layer on top of the SnO_2 and the FTO-glass substrate

2.2.3 Current-Voltage Curves

As previously discussed in the introduction, the great success and popularity of perovskite solar cells are primarily due to their power conversion efficiencies. The PCE is typically determined from the current density vs voltage curves, commonly obtained by measuring the current resulting from applied potential under illumination.

The J-V curve of the device can be characterized by the diode equation (UNGER et al., 2020; WÜRFEL; WÜRFEL, 2016). In addition to the PCE, the short-circuit current density (J_{sc}), open circuit voltage (V_{oc}), and fill factor (FF) are the most elementary metrics obtained from the J-V curves. The PCE can be expressed by multiplying the J_{sc}, V_{oc}, and FF divided by the incident power (P_{in}), as given in Equation 3. A schematic of a J-V curve and its characteristic points can be seen in Figure 14 below.

$$PCE = \frac{P_{mpp}}{P_{in}} = \frac{V_{mpp} \times J_{mpp}}{P_{in}} = \frac{V_{oc} \times J_{sc} \times FF}{P_{in}} \qquad \text{Eq (3)}$$

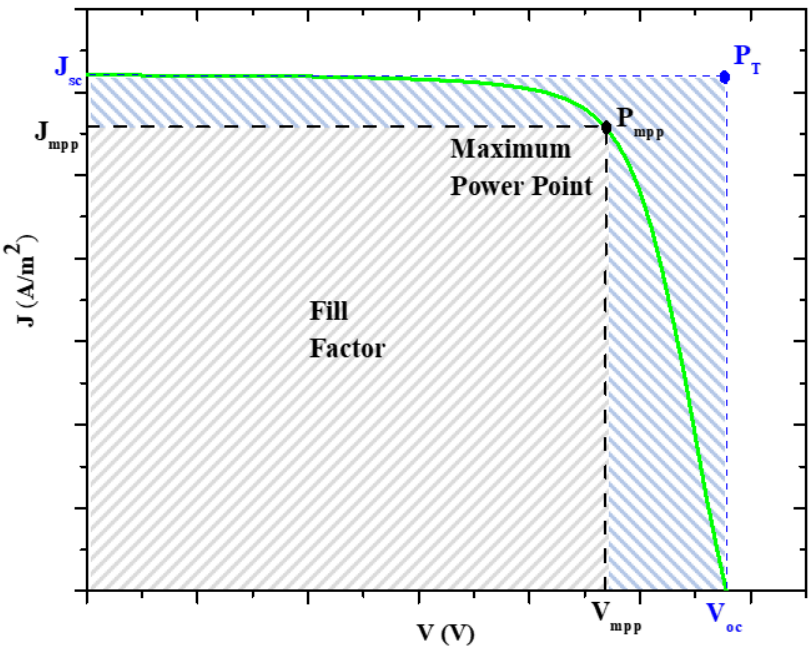

FIGURE 14. The figure indicates the J-V curve of a perovskite solar cell and the main points of interest concerning device analyses and performance quantification.

From the J-V curve schematic, it is possible to note the J_{sc} at the point when the curve crosses the y-axis. The point represents the maximum current that can be obtained from the

solar cell and refers to the value at which no voltage is applied and is equivalent to the terminals of the devices being short-circuited. On the other hand, the V_{oc} is represented by the point where the curve crosses the x-axis, i.e., the current is zero. In other words, no current is flowing through the device. The V_{oc}, alternatively, can be described as the equilibrium between charge generation and extraction. ("Electrical Characterization of Organic and Perovskite Solar Cells", 2023; "PVEducation", 2023; WÜRFEL; WÜRFEL, 2016).

The FF is relative to how close to the theoretical efficiency limit the device reaches. It is worth mentioning that actual devices present a limitation in their efficiency, which means the impossibility of achieving total energy conversion. This characteristic is known as the Shockley–Queisser limit (ABOU-RAS; KIRCHARTZ; RAU, 2011; SHOCKLEY; QUEISSER, 1961; WÜRFEL; WÜRFEL, 2016). Hence, it is essential to consider the probability of incident photons being absorbed, leading to the generation of electron-hole pairs and the subsequent processes of thermalization or recombination. Additionally, the maximum power point (MPP), denoted by P_{mpp}, is the maximum output power resulting from the current density and voltage of the device and will be a point of interest in future analysis and discussions.

Although parameters such as the V_{oc}, J_{sc}, and FF from the J-V curves are widely used to describe the device performance, other factors can also be obtained to complement the investigation of the limitations on the device performance. Those are derived from fitting the J-V curve according to the diode equation, like the series resistance (R_s), shunt resistance (R_{sh}), saturation current (I_o), and ideality factor (n) (CHAN; PHANG, 1987; DIANTORO et al., 2018; WÜRFEL; WÜRFEL, 2016; YANG et al., 2023).

However, obtaining with high precision the equivalent circuit parameters derived from the J-V curve fitted according to the diode equations is a challenge (PREMKUMAR et al., 2023; YANG et al., 2023), since it is sensitive to instrumental and measurement deviation. Furthermore, the device's performance can be strongly affected by hysteresis effects, light intensity, relaxation process, and others. Several models and approaches (CHAN; PHANG, 1987; DIANTORO et al., 2018; PREMKUMAR et al., 2023; YANG et al., 2023) were proposed as alternatives to obtain the values mentioned.

The determination of the R_s and R_{sh} by the inverse of the slop of the J-V curve at V_{oc} and J_{sc} points, respectively, is reported as an acceptable analytical method and will be employed in this work to cross-compare the effect of the resistance in the different devices (DIANTORO et al., 2018; "PVEducation", 2023). Although parameters such as I_0 and n are neglected, the resistance determination using the slopes is a quick, simple, and reliable alternative for an

estimative (DIANTORO et al., 2018). The slope of the curve was found using the first-order derivative. Afterward, the resistance was estimated using an average of four points toward V_{oc} and J_{sc} points in each curve.

Typically, J-V scans are performed with the incident power density based on solar spectrum references, such as the AM 1.5 G spectrum. This spectrum is related to the air mass, which quantifies the power reduction of the radiation that crosses the atmosphere and is absorbed before reaching the surface, and it is angle dependent. Figure 15 represents the spectra from AM 1.0, which is the extraterrestrial spectra (before entering the atmosphere at a normal incidence), and AM 1.5, which is the spectra that reach the Earth's surface at the incidence angle of 48.2 º ("Reference Air Mass 1.5 Spectra | Grid Modernization | NREL", 2023; SHROTRIYA et al., 2006).

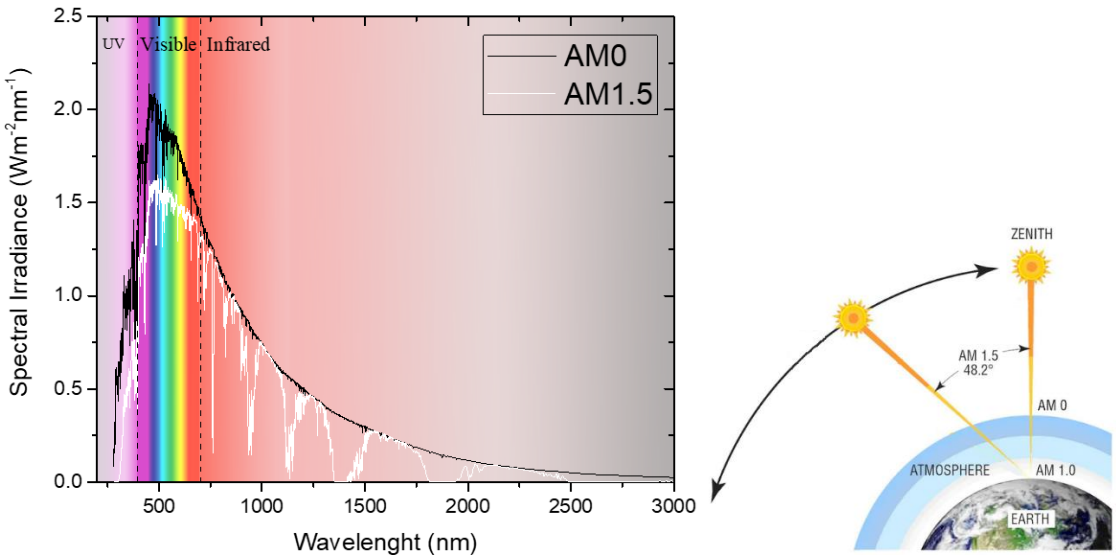

FIGURE 15. On the top is the AM 0 and AM 1.5 spectra. At the bottom is the representation of the difference between the AM 0 and AM 1.5 incidence. Adapted from "Reference Air Mass 1.5 Spectra | Grid Modernization | NREL", 2023; SHROTRIYA et al., (2006).

Furthermore, the scans are usually performed in two different directions, i.e., the polarization of the electric field, denoted by forward and reverse scan direction, in which the forward is the scan with voltage from "0 V" to V_{oc} and the reverse from V_{oc} to "0 V". Those two different scan directions frequently result in a discrepancy between the curves, nominated as hysteresis (shown in Figure 16).

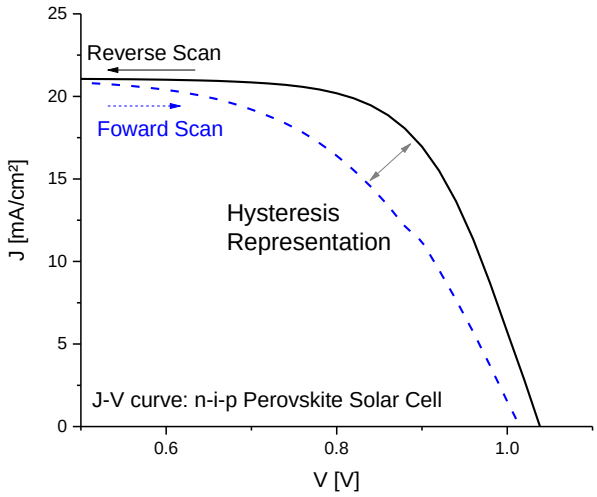

FIGURE 16. J-V curve of a n-i-p perovskite solar cell. The SnO_2 was used as the electron transport layer. The hysteresis, i.e., the discrepancy between the forward and reverse scan, is explicit in the figure.

Distinct reasons are usually addressed to cause the hysteresis. Several reports investigate this phenomenon and point to hysteresis as one of the crucial affairs in the perovskite solar cells' stability performance. However, those same reports highlight that accurate analysis can be tricky once the measurements affect the hysteresis shape, being necessary to achieve the steady-state response of the device during the measurement or as close as possible to a better hysteresis comparison.

In this work, the hysteresis of the J-V curves will be one of the points of interest, and for this analysis, the hysteresis index (HI) will be calculated via Equation 4 (HABISREUTINGER; NOEL; SNAITH, 2018; UNGER et al., 2020). Whereas the investigation of the hysteresis may lead to an inaccurate conclusion, it works very well to cross-compare the sample's performance measured under the same conditions.

$$HI = \frac{PCE_{rev} - PCE_{for}}{PCE_{rev}} \qquad \text{Eq. (4)}$$

In this way, the J-V curves measurements, in forward and reverse scan directions, were made using AAA Wavelabs Sinus-70 sun simulator (LED source) adjusted to emit accordingly with the AM 1.5 G spectra and 1000 W/m² of intensity. The active area measured of the cells was 0.09 cm² (limited by a metallic mask), and the standard values for the delay and integration time and the voltage steps were 40 ms, 20 ms, and 20 mV, respectively. However, devices were

also measured at different times, as explained in the results, to analyze the hysteresis change. The measurement parameters were controlled by a digital source meter (Keithley model 2400) and could be adjusted by an interface programmed in LabVIEW code. The support for the sample and the mask utilized in the measurement is shown in Figure 17.

FIGURE 17. Image of the perovskite solar cell on the sample holder and the mask. The device is being prepared to measure the J-V curve.

2.2.4 The MPP tracking and the transient response

The J-V curves might result in mismatches of the device performance and imprecise maximum power point values since it strongly depends on the scan conditions. Although it is a usual methodology applied for device characterization, comparing between different laboratories, and determining the steady-state performance of the solar cells is not trivial, and the transient phenomena must be taken carefully into account (CZUDEK et al., 2019; HABISREUTINGER; NOEL; SNAITH, 2018; UNGER et al., 2014). Therefore, alternative measurements can be used to complement those data.

Among the complementary analysis, the maximum power point tracking (MPPT) and a new methodology proposed by Unger and collaborators (CZUDEK et al., 2019; DAGAR et al., 2019; UNGER et al., 2014), denominated as transient maximum power point tracking (TrAMPPT) or dynamic maximum power point tracking (DyMPPT) can be used to access the steady state response and the short-term stability of the devices.

The MPPT involves monitoring the maximum power point over time. For this study, a standard perturb-and-observe algorithm was used (CZUDEK et al., 2019; RAM; BABU;

RAJASEKAR, 2017) as part of the J-V curves measurement routine. This analysis includes applying ± 10 mV double-step perturbation at the MPP voltage (V_{mpp}) derived from the J-V measurements. Then, a new value for the V_{mpp} is assigned, and the perturbation is applied again, repeating this over the designed time.

Meanwhile, the TrAMPPT can be seen as an expansion of this method to monitor the transient response of the devices. In addition, the TrAMPPT allows the determination of conditions (times scales) for the J-V measurement closer to the quasi-steady-state condition. Although this could be done by changing the J-V curve scan rate several times and comparing the HI mentioned before, it would be extremely time-consuming. On the other hand, the TrAMPPT may be a faster and more complete analysis. For the TrAMPPT, a perturbation of ± 50 mV around the V_{mpp} is applied. It allows an amplitude large enough for fitting using a biexponential expressed in Equation 5. The voltage cycle is represented in Figure 17.

$$J(t) = J_{ss} + A_{fast}e^{-\left(\frac{t-t_0}{\tau_{fast}}\right)} + A_{slow}e^{-\left(\frac{t-t_0}{\tau_{slow}}\right)} \quad \text{Eq. (5)}$$

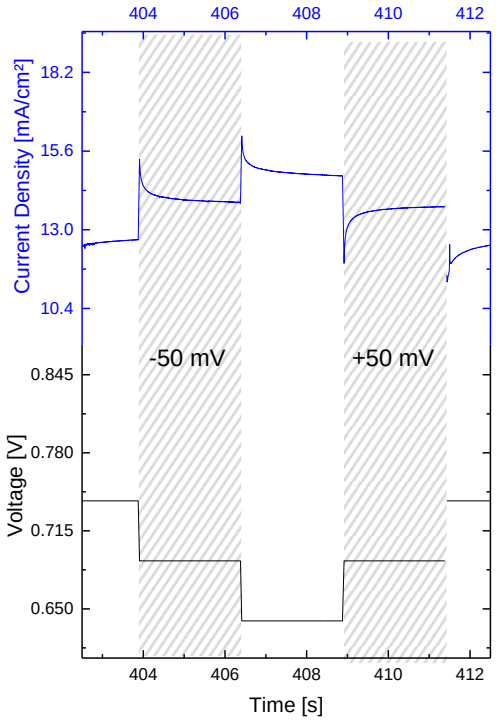

FIGURE 18. Representation of the double steps of the voltage perturbation for the TrAMPPT analysis carried out in an n-i-p FACs-based perovskite solar cell using the niobium pentoxide as the electron transport layer.

In Equation 5, A and τ are the amplitude and time constant, respectively, being considered for the fast and slow response. J_{ss} is the steady state current. The fitting, and consequently those values, were determined by a MATLAB code. The τ_{slow} is considered equivalent to the minimum delay (settling) time suitable to perform the J-V measurement that may present the minimum hysteresis of the device.

The correspondent value of the relative discrepancy ($\frac{\Delta J(t)}{J_{ss}}$) between the forward ($J_{trans,F}(t)$) and reverse ($J_{trans,R}(t)$) scans can be estimated from the TrAMPPT using Equation 6, and it will be compared with the HI calculated at different scan rates, as shown and discussed in the Results section.

$$\frac{\Delta J(t)}{J_{ss}} = \frac{J_{trans,R}(t) - J_{trans,F}(t)}{J_{ss}} \qquad \text{Eq. (6)}$$

All the MPPT and TrAMPPT analyses were carried out using the same setup of the J-V curves. For the measurements of the samples, the J-V curve at the standard scan rate was first done, followed by the MPPT and TrAMPPT, and, finally, the J-V curves with different scan rates for the HI comparison.

2.2.5 External Quantum Efficiency

External quantum efficiency (EQE) can be defined as the number of electrons that are collected per photon incident on the solar cell (ABOU-RAS; KIRCHARTZ; RAU, 2011). For an ideal solar cell, it was expected that all the incident photons with energy above the bandgap would be absorbed. Although, in the real solar cell, this does not happen, as explained previously by the Shockley-Queisser limit. Thus, the EQE measurements allow one to measure the real number of photos that generate the electron-hole pairs in the function of the energy or wavelength and depend on the light-harvesting efficiency, charge injection, transfer, and extraction (ABOU-RAS; KIRCHARTZ; RAU, 2011; HEO et al., 2015)

For the measurements, a light source generates the irradiation, then a chopper and a lock-in are used to modulate the light and amplify the signal. After that, monochromatic light is selected using a monochromator, and the beam is focused on the surface of the sample, being either a reference or the solar cell, through the adjustment of the position of the sample. A silicon detector was used as a reference, and the reference spectra are shown in Figure 19. In the solar

cell, the beam was focused on the pixel with the best performance evaluated from the J-V curves. Then, the spectra of the EQE are recorded, here, in function of the wavelength.

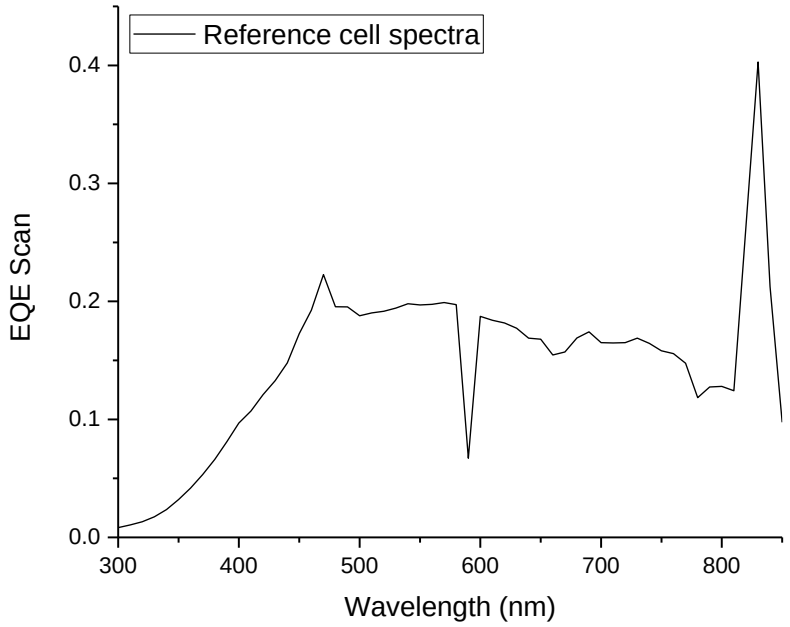

FIGURE 19. The EQE spectra performed before measurements using the calibration cell and used as reference.

An Oriel Instruments QEPVSI-b with a Xenon arc lamp (Newport 300 W, 66902) chopped at 35.5 Hz and a Newport Cornerstone 260 monochromator was used for this measurement. The EQEs were performed on n-i-p samples with the SnO_2 as ETL and the KCl additive to cross-compare possible changes in the optical-electronic characteristics due to the KCl additive.

3. Results and discussions

3.1 Slot die coated niobium pentoxide

Spin coating was shown as a feasible technique to obtain the Nb_2O_5 using solution-based processes (FERNANDES et al., 2022; SHEN et al., 2018; WANG et al., 2019b), described in the section 2.1.1. However, this technique has some limitations concerning the possibility of scale (YANG et al., 2022). As an intention to explore an alternative solution-based process and aim for a future possibility of scale-up, the niobium pentoxide deposition by slot die coating (SDC) was tested.

Initially, it was employed in the SDC process the same precursor solution as reported for the spin coating method (FERNANDES et al., 2022; SHEN et al., 2018). Then, the deposition parameters were varied. Different speeds for the web (considered the substrate holder and, consequently, the substrate) and the pump rate were mixed and tested. The parameters to be combined were; i) Web Speed: 25, 75, and 125 cm/min and; ii) Pump rate: 60, 120 and 300 μL/min.

The wet and dry film thickness were estimated by the equation 1 using the WS and PR variations. The constant values utilized for the w, C, and ρ, were respectively, 15 mm (measured blade width), 0.16 g/cm³ (0.05 M, Nb_2O_5 precursor solution), and 4.6 g/cm³ (Nb_2O_5 density). The results are presented in Table 3.

TABLE 3. Estimative of the wet and dry film thickness based on the coating parameters calculated by the theoretical equations.

Web Speed (cm/s)	Pump Rate (μL/s)	h_w (nm)	h_d (nm)
25	60	16000	55.3
	120	32000	110.7
	300	80000	276.7
75	60	5333	18.5
	120	10667	36.9
	300	26667	92.2
125	60	3200	11.1
	120	6400	22.1
	300	16000	55.3

Via Equation 2, a correlation curve predicting the stable and unstable coating limits according to the viscocapillary model was plotted based and the Ca were calculated to evaluate

if the coating, for the different web speed and pump rate combinations, were either close to a stable or unstable coating window. The relationship is illustrated in Figure 20. The value of 2 µm was used for the gap, unchanged for all the samples.

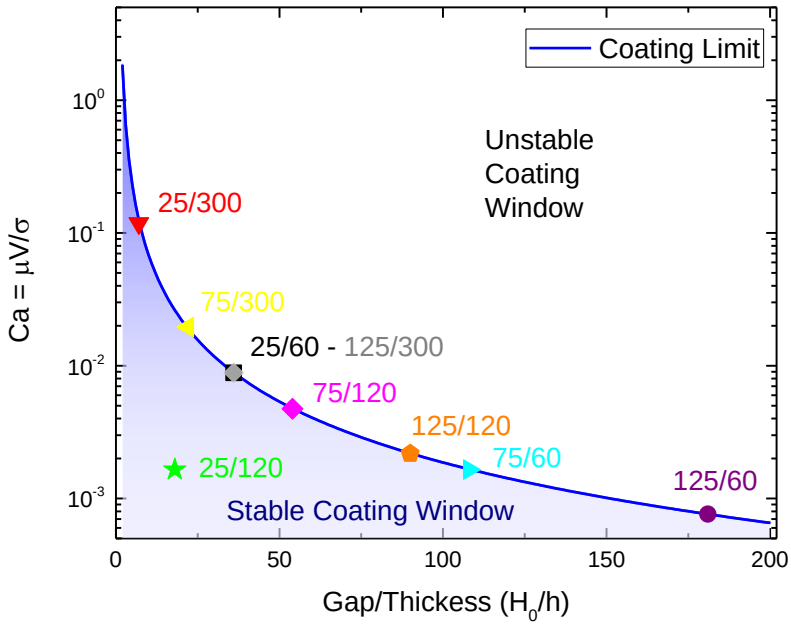

FIGURE 20. Prediction curve of the limit between the stable and unstable regions for the coating. In addition, it is presented in which window each parameter may be. It was plotted based on Equation 2

As can be noted in Figure 20 , only the sample with web speed of 25 cm/s and pump rate of 120 µL/s was inside the stable zone as the prediction following the viscocapillary model. The other samples are in the limit between stable and unstable operation, which may affect the coating quality and, consequently, the device performance, as it will be discussed in following sections.

To obtain an overview of the coating, concerning the application as electron transport layer, microscopy measurements were performed to investigate the possible changes in the coverage related to the variation of parameters.

3.1.1 Coating surface analysis

The Figures from 21 to 29 show the surface and the cross-section image obtained via the scanning electron microscopy (SEM) for the morphology and thickness analysis.

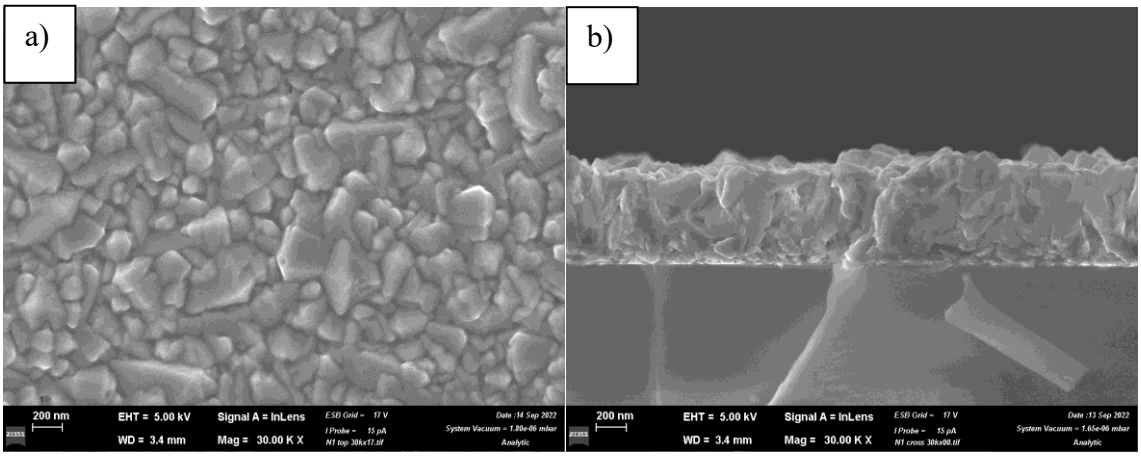

FIGURE 21. Microscopy image of the sample coated at web speed: 25 cm/min and pump rate: 60 µL/min; a) Surface SEM; b) Cross-Section SEM.

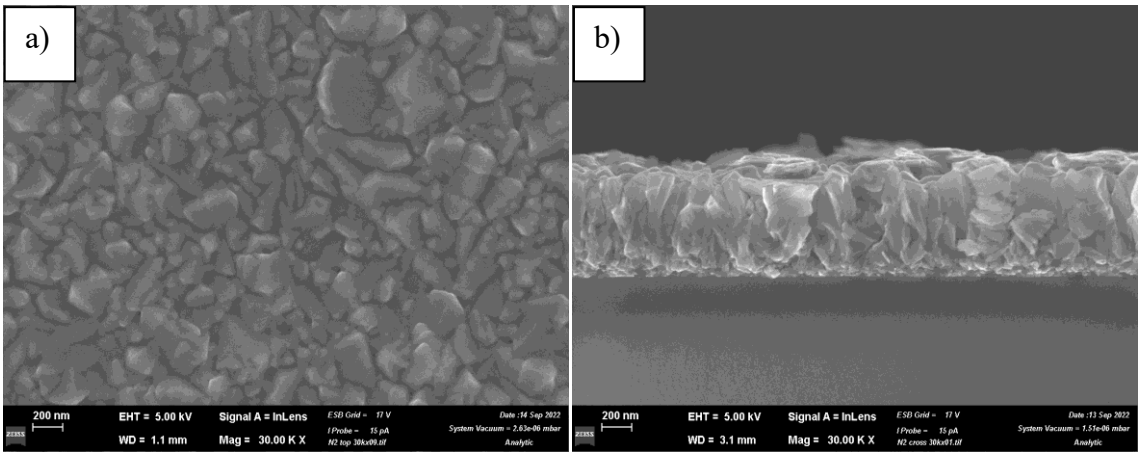

FIGURE 22. Microscopy image of the sample coated at web speed: 25 cm/min and pump rate: 120 µL/min; a) Surface SEM; b) Cross-Section SEM.

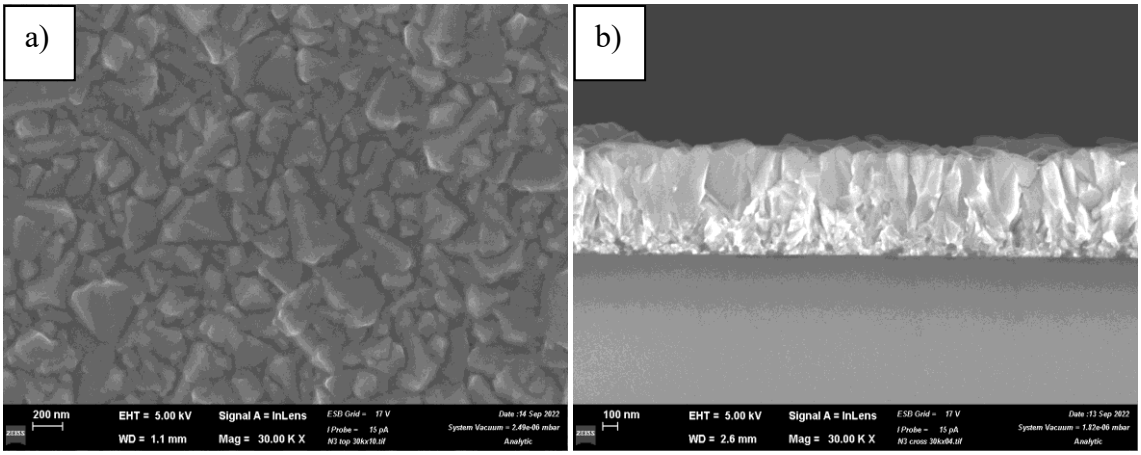

FIGURE 23. Microscopy image of the sample coated at web speed: 25 cm/min and pump rate: 300 µL/min; a) Surface SEM; b) Cross-Section SEM.

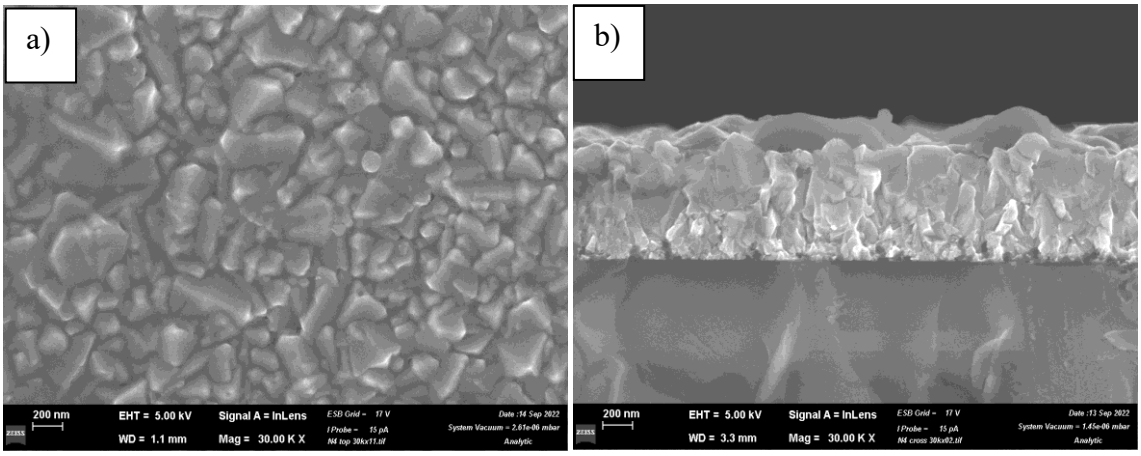

FIGURE 24. Microscopy image of the sample coated at web speed: 75 cm/min and pump rate: 60 µL/min; a) Surface SEM; b) Cross-Section SEM.

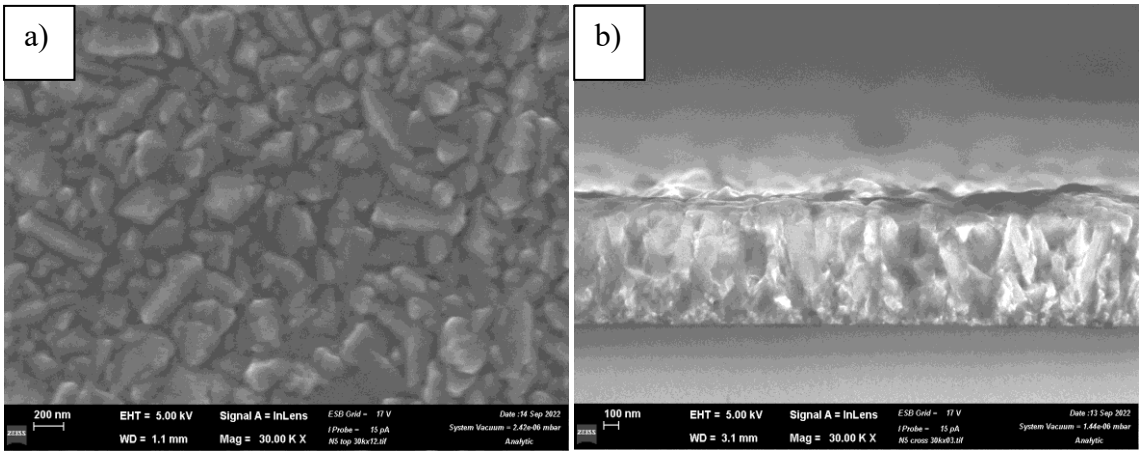

FIGURE 25. Microscopy image of the sample coated at web speed: 75 cm/min and pump rate: 120 µL/min; a) Surface SEM; b) Cross-Section SEM.

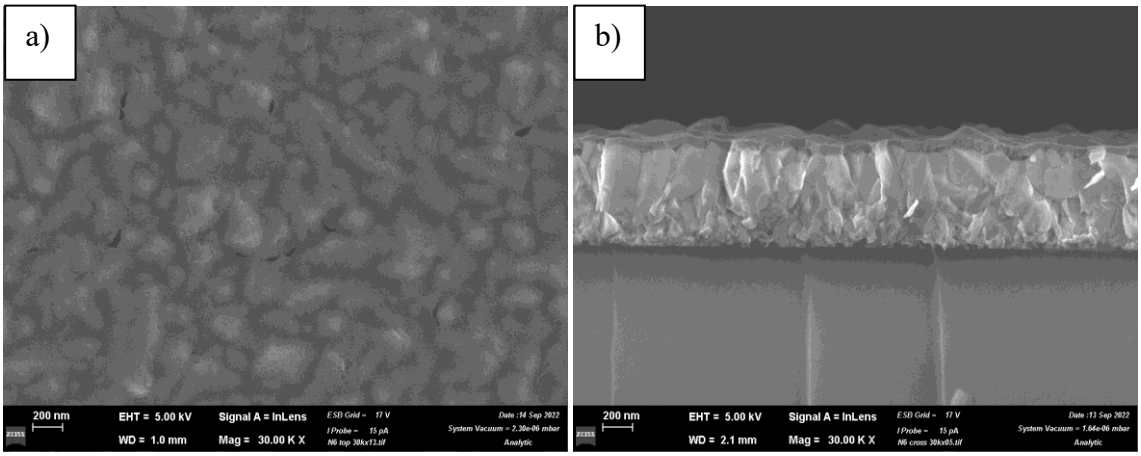

FIGURE 26. Microscopy image of the sample coated at web speed: 75 cm/min and pump rate: 300 µL/min; a) Surface SEM; b) Cross-Section SEM.

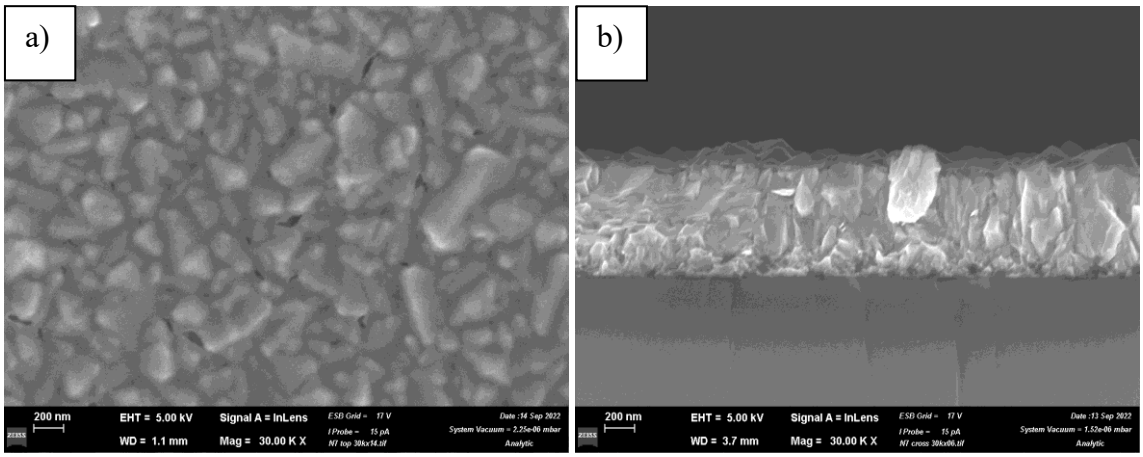

FIGURE 27.Microscopy image of the sample coated at web speed: 125 cm/min and pump rate: 60 µL/min; a) Surface SEM; b) Cross-Section SEM.

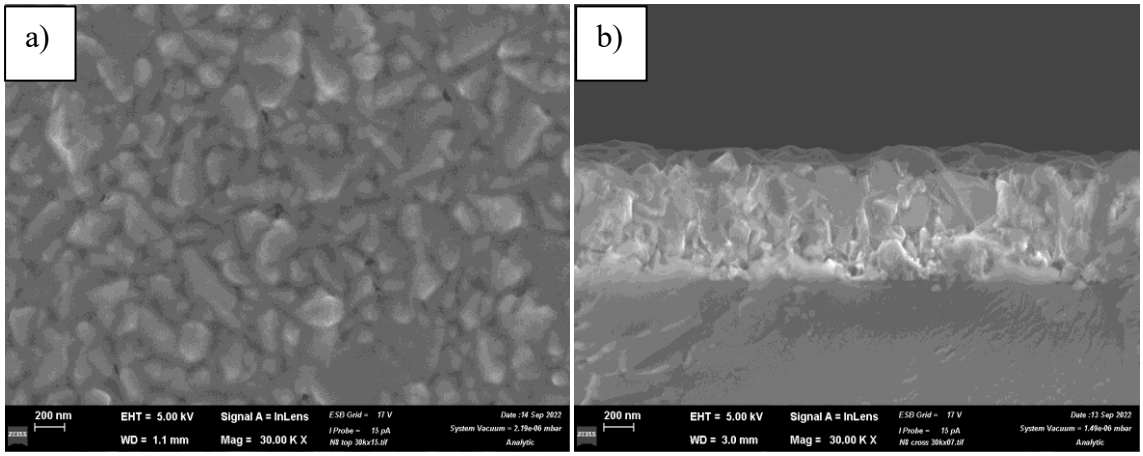

FIGURE 28. Microscopy image of the sample coated at web speed: 125 cm/min and pump rate: 120 µL/min; a) Surface SEM; b) Cross-Section SEM.

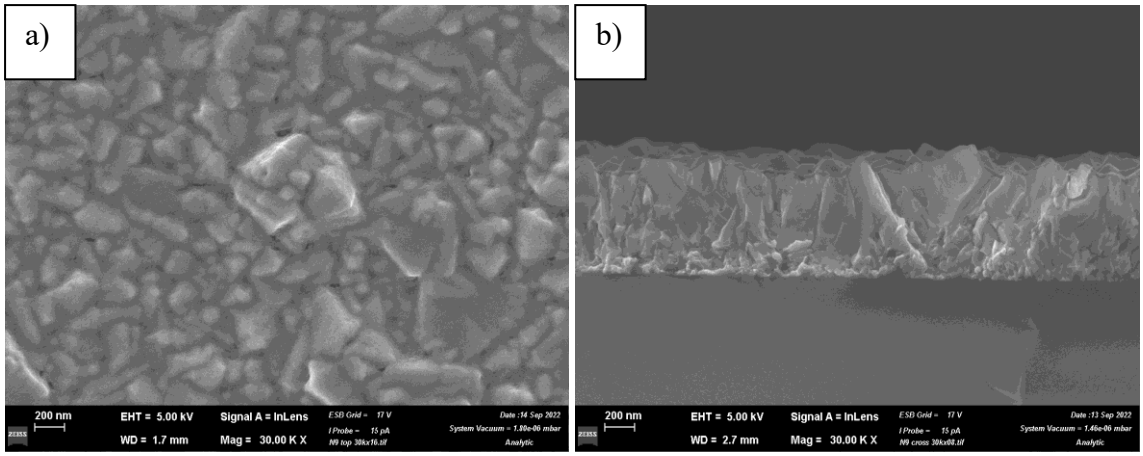

FIGURE 29.Microscopy image of the sample coated at web speed: 125 cm/min and pump rate: 300 µL/min; a) Surface SEM; b) Cross-Section SEM.

From the surface measurements, it is possible to note some similarities, like the overall shape of the grains. Most of them are very similar to the FTO substrate morphology, which indicates that the thickness should not be enough to overcome the substrate characteristic. The sample with a Web Speed of 125 cm/min is one of the exceptions. The surface shows some non-uniform regions that seem like either holes, pores, or unknown particles at the surface.

Concerning the pinhole analysis, Table 4 contains the pinhole count and the thickness estimative of each sample and correlated to the SEM images. The thickness in function of the coating parameters are also presented in Figure 30. It is possible to note that the samples shown in Figures 20 and 27 are related to the sample that had the lower number of pinholes, about 10. Meanwhile, Figure 26 to the sample with the highest number of them, about 30. It might be related to the device's performance, which will be discussed later in the next section.

TABLE 4. Values estimated to the thickness from the cross section and the pinhole counts from the laser confocal microscopy.

Surface Analysis - Nb_2O_5					
Web Speed (cm/min) Pump Rate (µl/min)	**SEM Figure**	**Thickness (nm)**	**Standard Deviation (± nm)**	**Pinhole (Counts)**	**Standard Deviation (%)**
25 / 60	21	<10	-	17	47
25 / 120	22	12	4	10	30
25 / 300	23	14	4	13	38
75 / 60	24	21	4	19	95
75 / 120	25	<10	-	15	40
75 / 300	26	42	8	17	47
125 / 60	27	18	4	12	42
125 / 120	28	18	5	30	60
125 / 300	29	17	6	10	40

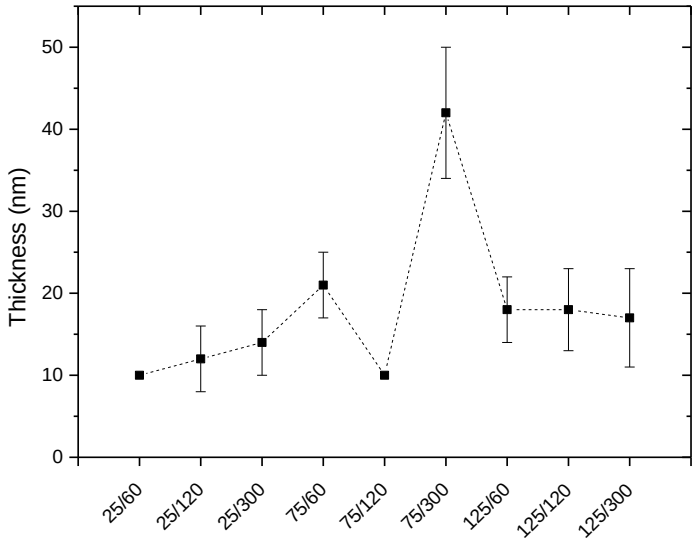

FIGURE 30. The thickness estimated for the Nb_2O_5 layer, using the SEM images, in function of the coating parameters.

In most of the cross-section images, it is not clear the partition between the Nb_2O_5 and FTO layers. It could indicate that the layer is thin and unable to cover the roughness of the substrate. However, it was possible to verify the thickness ranging from 30 to 50 nm.

Regardless of the difficulty in differentiating the Nb_2O_5 in the measurements, the thickness is one of the characteristics that need to be optimized and will affect the device performance, as reported elsewhere (FERNANDES et al., 2016; GUO et al., 2018; HUANG et al., 2017; SHEN et al., 2018; ZHAO et al., 2020). Although the cited work showed that the thickness of the Nb_2O_5 for devices with optimized performance was around 100 nm, here it was found that around 20 nm presented a better performance than thicker samples like 50 nm. However, it is important to consider this could also be addressed to the quality of the layer, resulted from a coating performed in a stable region.

To further verify the applicability of the coating and the impact of the diversity of parameters, the different layers were applied in the perovskite n-i-p devices and characterized as described in the next topic.

3.1.2 Devices J-V Curves

The devices with the SD coated Nb_2O_5 as the electron transport layer were characterized firstly with the current density x voltage curves (J-V curves). Each sample, related to each

combination of parameters, has six pixels or cells with an area of 0.09 cm². The curves presented in the following figures show the forward and reverse scans of each distinct cell.

Figure 31 shows the scan of the sample in which the result had an inferior performance, followed by Table 5 with the numerical data. On the other hand, Figure 32 is the curve of the sample with the best performance, as the same for Table 6, which contains the respective values of that device. The J-V curve and numerical data associated with the intermediary performance can be found in the appendix.

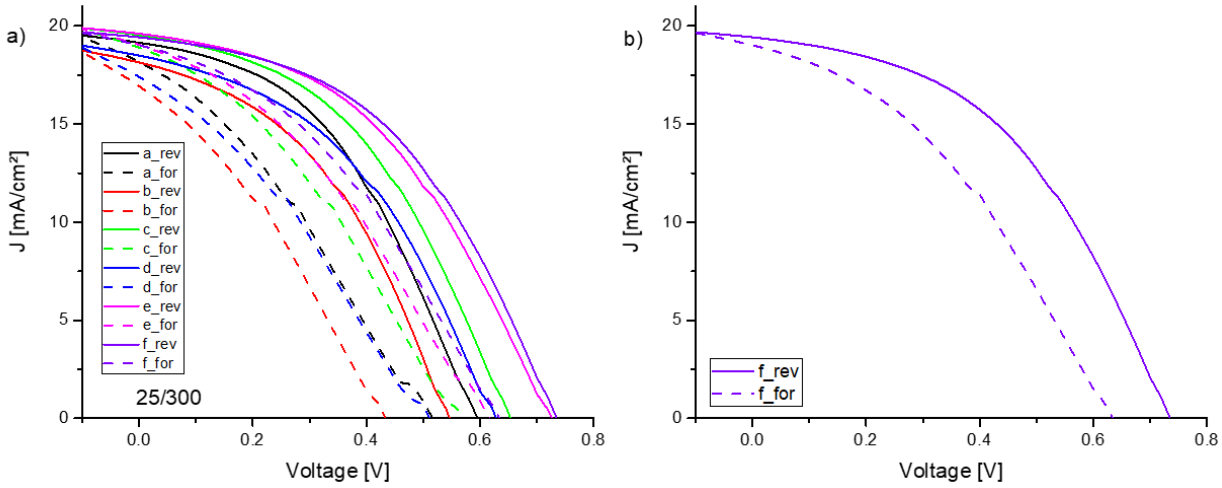

FIGURE 31. Current density versus voltage curve in reverse and forward scans. a) Curve for each of six pixels in one sample coated at web speed 25 cm/min and pump rate 300 µL/min. b) Curve of the best pixel of the sample.

TABLE 5. Values of the parameters obtained from the current density versus voltage curve in reverse and forward scans for the coated sample at web speed 25 cm/min and pump rate 300 µL/min. The values in the table are for the best pixel and the average for the six pixels in the device.

Web speed: 25 cm/min, Pump rate: 300 µL/min.				
Parameter	F Rev.	F For.	Avg. Rev.	Avg. For.
J_{sc} (mA/cm²)	19.42	19.02	19.1 ± 0.6	18.2 ± 0.9
V_{oc} (V)	0.73	0.63	0.65 ± 0.07	0.55 ± 0.07
Fill Factor (%)	45.57	37.87	43 ± 2	34 ± 2
Rsh (Ohmcm²)	0.32	0.14	-	
Rs (mOhmcm²)	15.33	22.83		
PCE (%)	6.50	4.56	5.4 ± 0.9	3.5 ± 0.8
HI	0.30		0.36	

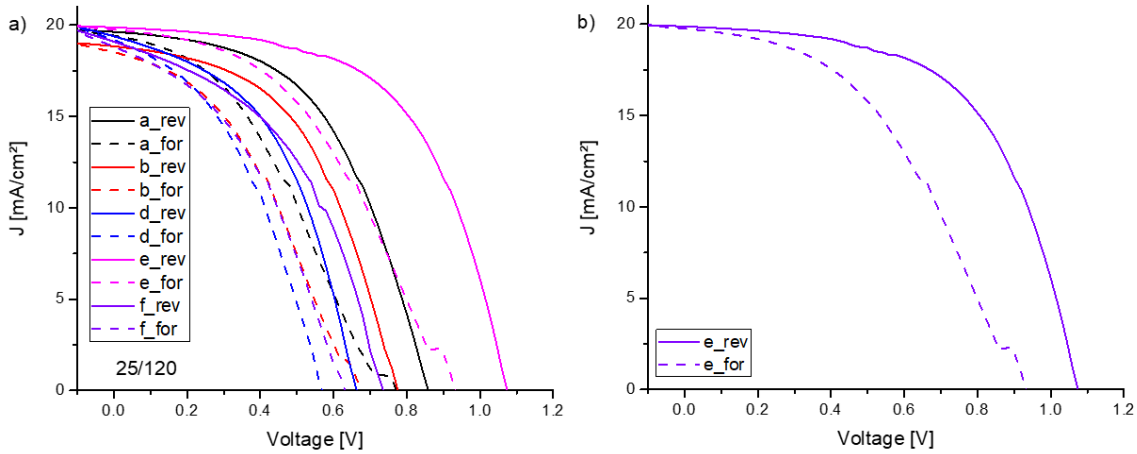

FIGURE 32. Current density versus voltage curve in reverse and forward scans. a) Curve for each of six pixels in one sample coated at web speed 25 cm/min and pump rate 120 µL/min. b) Curve of the best pixel of the sample.

TABLE 6. Values of the parameters obtained from the current density versus voltage curve in reverse and forward scans for the coated sample at web speed 25 cm/min and pump rate 120 µL/min. The values in the table are for the best pixel and the average for the six pixels in the device.

Web speed: 25 cm/min, Pump rate: 120 µL/min.				
Parameter	E Rev.	E For.	Avg. Rev.	Avg. For.
J_{sc} (mA/cm²)	19.88	19.75	19.3 ± 0.4	19.1 ± 0.4
V_{oc} (V)	1.07	0.93	0.8 ± 0.1	0.7 ± 0.1
Fill Factor (%)	57.25	43.47	52 ± 3	42 ± 2
Rsh (Ohmcm²)	1.15	0.53	-	
Rs (mOhmcm²)	9.43	15.75		
PCE (%)	12.22	8.00	8 ± 1	6 ± 1
HI	0.35		0.31	

For the first attempt, the best pixel, concerning the PCE, was achieved for the sample with a web speed of 25 cm/min and pump rate of 120 µL/min, with 12% for the reverse scan, highlighting the potential in utilize the Nb_2O_5 coated by SDC as ETL. Nevertheless, optimization in the coating, such as the thickness, through changes in the process, like the concentration of the precursor or the preheating of substrates, might be necessary to reach or even surpass the current performance reported in the literature (DING; LIU; HARRIS, 2016; FERNANDES et al., 2022; GUO et al., 2018; PATIDAR et al., 2020; SHEN et al., 2018). In addition, even for the samples with pixels that showed lower performance, the overall result was satisfactory, with the PCE of almost all the pixels being >5%. The statistical results of the other characteristics, J_{sc}, V_{oc}, FF, PCE, and HI, obtained from the J-V curves are presented in Figure 33.

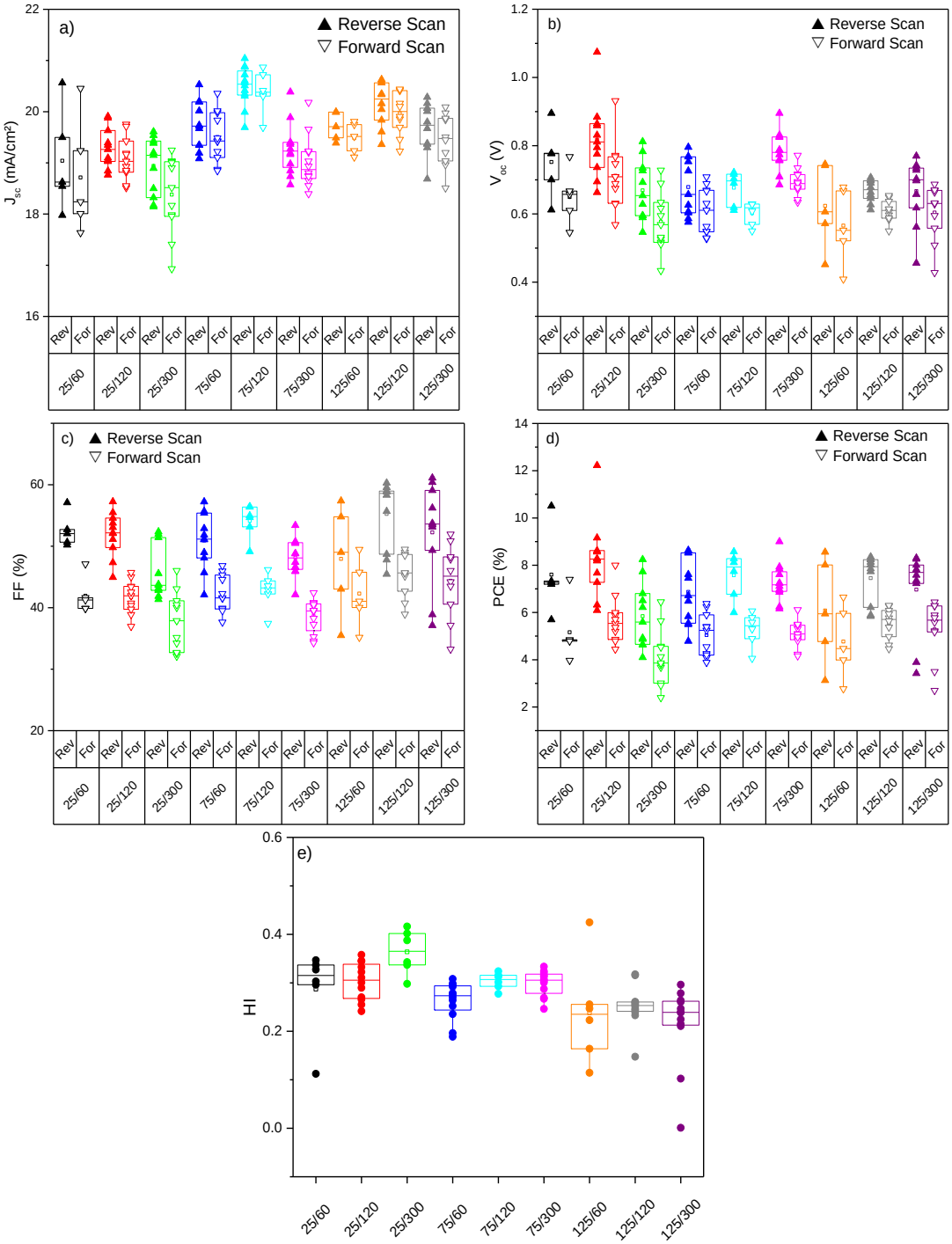

FIGURE 33. Statistic results obtained from the J-V curves of a) J_{sc}, b) V_{oc}, c) FF, d) PCE, and e) HI for all the Nb_2O_5 samples coated with different parameters by slot die coating.

Although it is not so simple to analyze and correlate the hysteresis index (HI) with the stability of the device (CZUDEK et al., 2019; HABISREUTINGER; NOEL; SNAITH, 2018; UNGER et al., 2014), the index can be taken as a first approach to compare the short-term stability among the devices. It is possible to note, in Figure 33 e), that the higher HI, representing the broader difference between the reverse and forward scans, is observed for the

sample coated at a web speed of 25 cm/min and pump rate of 300 μL/min which is also the sample with the worst PCE.

On the other hand, it is not easy to identify the sample with lower HI, and although the sample with a web speed of 25 cm/min and pump rate of 120 μL/min had the best PCE, it presents an intermediate value of HI. This indicates that short-term stability is compromised. In search to better comprehend those relations, the maximum power point tracking was done which is presented in the following sections.

Although the devices' architecture is different, a careful comparison between the devices explored here and the one related to previous work developed on the group considered that some differences arise from the mesoporous layers. In the pioneer study, (FERNANDES et al., 2016), reported the result for devices using the MAPI perovskite, a TiO_2 mesoporous layer, and the compact Nb_2O_5 deposited by reactive sputtering with thickness ranging from 50 to 220 nm. A higher efficiency of 12.3 % was found for a reverse scan of the device with 50 nm. The same device showed 17.9 mA/cm², 0.92 V, and 74 % for the J_{sc}, V_{oc}, and FF respectively. In addition, no hysteresis effect was observed, which motivated the use of the compact Nb_2O_5 over the compact TiO_2. The difference in performance was attributed to the thickness affecting the electron-hole extraction balance, which mitigates the charge accumulation, therefore increasing the performance.

Following, (FERNANDES et al., 2019), reported the effect of different oxygen rates during the deposition of the Nb_2O_5 compact layer deposition. The device configuration was the same as previously reported, except that the thickness was optimized for 100 nm. It was found that the oxygen content affects the vacancies and, therefore the conductivity, and phase of the niobium layer. The best performance was found in the sample deposited at 3.5 sccm (standard cubic centimeters per minute) of oxygen, with an efficiency of 15.4 %, and J_{sc} of 21.77 mA/cm². V_{oc} of 0.98 V and FF of 73 %. No hysteresis was observed for this device. However, as the oxygen content increased, the hysteresis effect occurred.

Recently, (FERNANDES et al., 2022), published a study comparing the niobium oxide deposition by reactive sputtering and spin coating. In both cases, a TiO_2 mesoporous layer was deposited on top of the Nb_2O_5 compact layer, and the perovskite utilized was the CsFA. The devices with the Nb_2O_5 deposited by sputtering showed a better performance, which was attributed to a more homogeneous, compact, and pin-hole free layer. In addition, it seems to induce a better crystallization of the perovskite layer, which induces a better change separation and transport. The sputtered Nb_2O_5 device had an efficiency of 17 %, with 22.0 mA/cm², 1.05

V, and 73 % of J_{sc}, V_{oc}, and FF respectively, against PCE of 16 %, J_{sc} of 22.2 mA/cm², V_{oc} 1.02 V, and FF of 69 % for the spin-coated device. In this case, both devices had a hysteresis index of about 0.10.

Compared with this study, the first and most important point to highlight is that no mesoporous layer was used, which already represents an improvement that was not achieved before. Despite that, a higher V_{oc} for the sample coated at a web speed of 25 cm/min and pump rate of 120 µL/min had a V_{oc} superior to all other samples. However, except for the J_{sc} of the first publication, all parameters were inferior. The difference in performance, especially hysteresis, could be attributed mainly to two different causes: i. the change extraction, affected by defects, thickness, and the mesoporous layer; ii. J-V scan conditions. Nevertheless, the Nb_2O_5 has potential as an ETL. Moreover, the layer coated by SDC can be improved through the enhancement of the layer homogeneity and defect reduction, in addition to thickness optimization.

3.1.3 Devices MPP Tracking

Maximum power point tracking (MPPT) is one of the measurements that can be done for a rough analysis of short-term stability. The results for the sample with higher and lower performance are presented in Figure 34. For the other samples, the results can be verified in the appendix.

The sample coated at 25 cm/min and pump rate of 120 µL/min has an average decay compared with the other samples, as the same was observed at the HI. This could be an additional indication that the device still has space for improvement, especially concerning stability. Similarly, the one with a web speed of 25 cm/min and a pump rate of 300 µL/min has a slightly higher decay in terms of power.

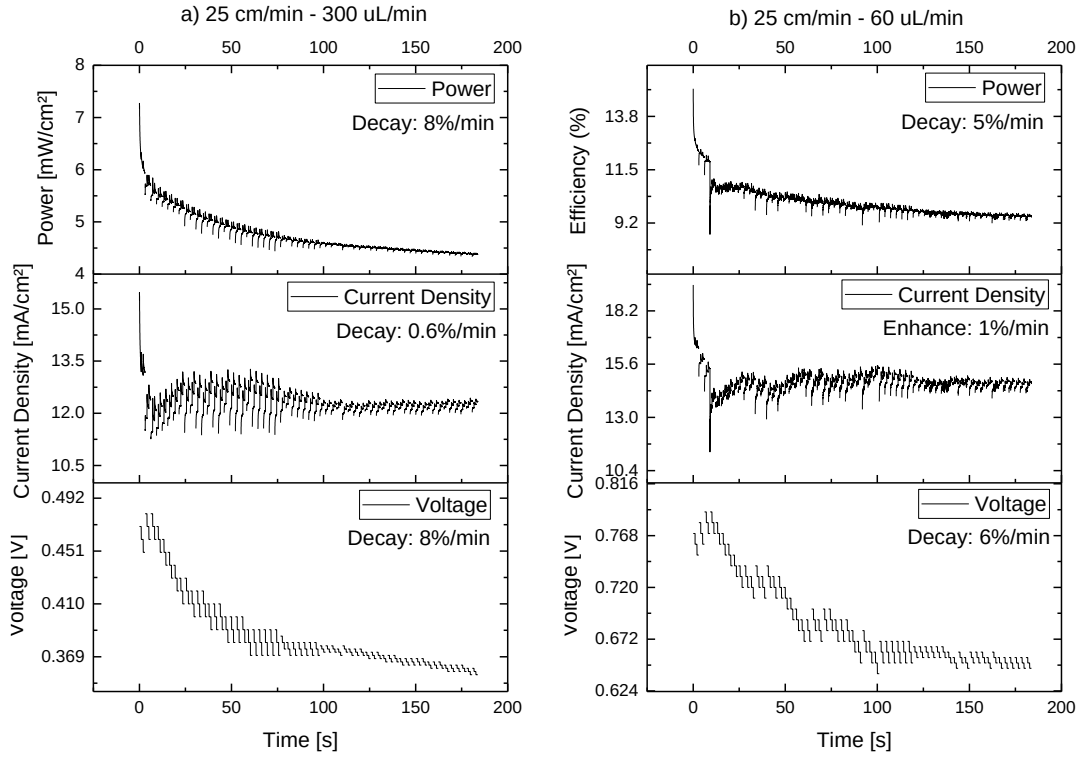

FIGURE 34. Power, Current density, and voltage vs time from the MPPT for a) the pixel with the overall lower PCE (web speed 25 cm/min and pump rate 300 µL/min). b) the pixel with the overall higher PCE (web speed 25 cm/min and pump rate 120 µL/min).

For a more precise evaluation of the steady-state analysis, a transient response of the MPPT, known as dynamic MPPT (DyMPPT) or transient MPPT (TrAMPPT) (CZUDEK et al., 2019; DAGAR et al., 2019; UNGER et al., 2014) was performed, and the results are shown in the next topic.

3.1.4 Dynamic MPP Tracking

As proposed by (CZUDEK et al., 2019), the TrAMPPT measurements can be considered a way to achieve the steady state and the transient response of devices. So, it is possible to estimate the transient time constant (τ_{slow} and τ_{fast}) and use them to establish a delay time that might be more suitable to be used at the J-V scans (CZUDEK et al., 2019; DAGAR et al., 2019). It is present in Figure 35 the TrAMPPT scans for the samples coated at a web speed of 25 cm/min and pump rate of 300 µL/min (lower performance) and web speed of 25 cm/min and pump rate of 120 µL/min (best performance), and the response for the transient photocurrent of each cycle (Perturbation of ± 50 mV toward the MPP).

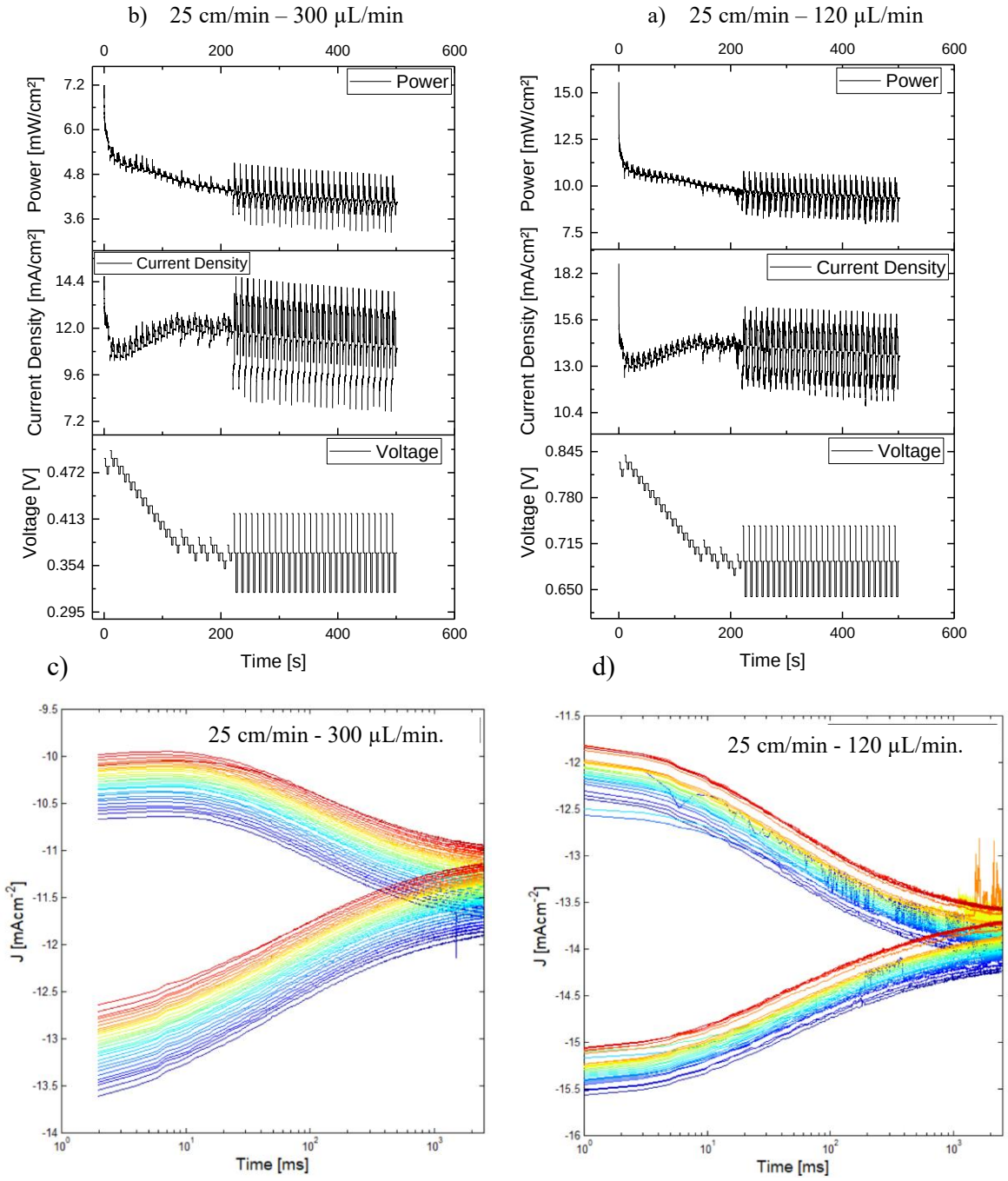

FIGURE 35. TrAMPPT measurements of sample coated at a) web speed of 25 cm/min and pump rate of 300 µL/min and b) web speed of 25 cm/min and pump rate of 120 µL/min. From top to bottom, it is shown the evolution in time for the maximum power point, the current density, and the maximum voltage towards MPP. Followed by the transient current response of c) sample at web speed of 25 cm/min and pump rate of 300 µL/min and d) sample at web speed of 25 cm/min and pump rate of 120 µL/min.

It is possible to note in Figure 35 c) and d) that, for both coating conditions, the photocurrent transient, for the – 50 mV and + 50 mV steps, are less symmetric under 10 ms, becoming more symmetrical over this value and merging for times above 100 ms, highlighting a dynamic capacitive response. Those changes indicate that the charge/discharge is affected

differently over time, which could mean that varied phenomena occur in different time scales (CZUDEK et al., 2019; UNGER et al., 2014).

The dynamic response in perovskite solar cells can be attributed to various factors, including the internal distribution of charges and defects, carrier trapping/de-trapping, and ion migration (DAGAR et al., 2019; GUERRERO et al., 2016; LEE et al., 2017; SHAO et al., 2014). However, which of the mentioned causes dominates at each time scale remains unclear. Furthermore, the hypothesis suggesting the existence of a few distinct causes influencing the transient and hysteresis response of perovskite solar cells is supported by the observation that a single time constant is insufficient to accurately fit the transient response. The τ_{slow} and τ_{fast}, amplitudes, and steady-state current density (J_{ss}) obtained fitting those curves with Equation 3 (as described in Section 2.2.4) are shown in Figure 36.

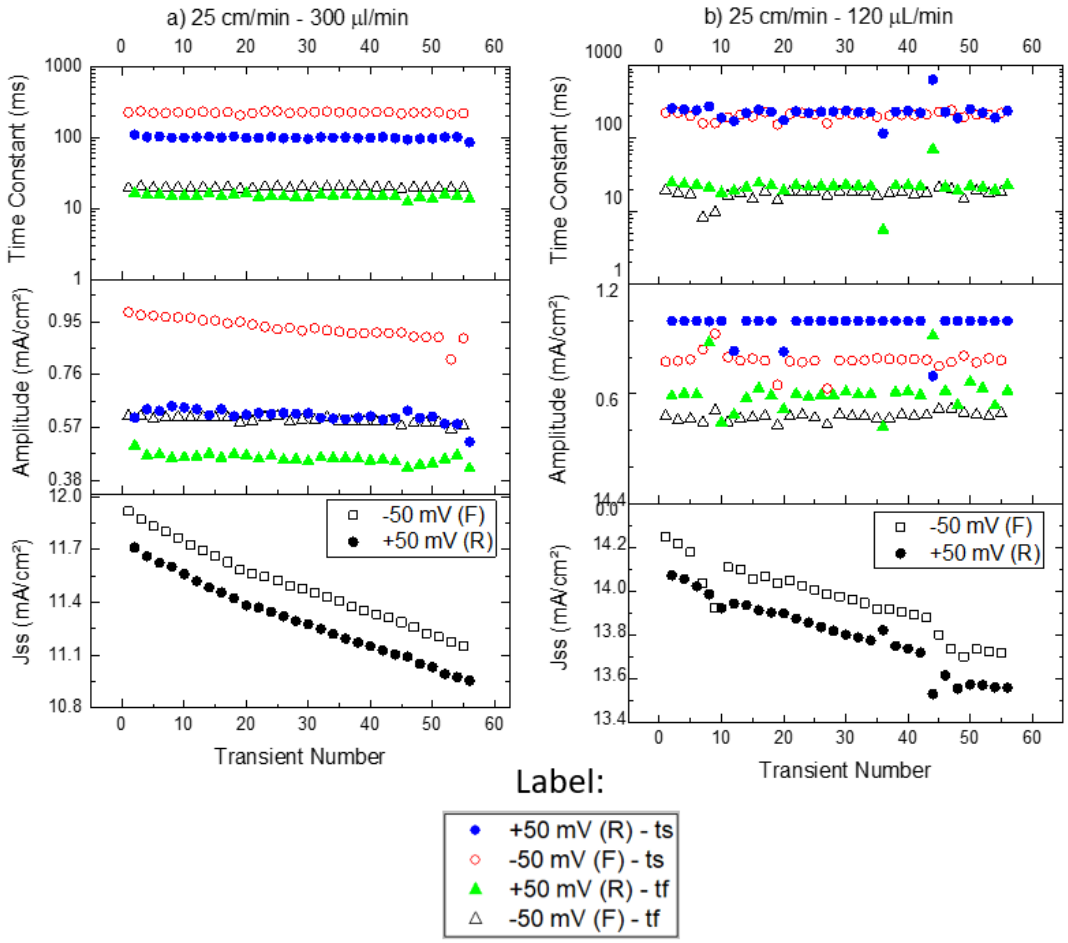

FIGURE 36. The top panel shows the time constants (τ_{slow} - ts - and τ_{fast} - tf -), followed by the amplitude, and the bottom panel shows the steady state current (J_{ss}) for the sample coated at a) web speed of 25 cm/min and pump rate of 300 µL/min and b) web speed of 25 cm/min and pump rate of 120 µL/min, for the -50 mV (Forward - F -) and +50 mV (Reverse - R -) steps.

Furthermore, there is a notable decline in the J_{ss} for both devices in Figure 36. The device's web speed of 25 cm/min and pump rate of 120 µL/min declines from 14.10 mA/cm² and 14.07 mA/cm², in -50 mV and +50 mV respectively, at a rate of 0.009 mA/cm²min for both cases. The device of web speed of 25 cm/min and pump rate of 300 µL/min declines at 0.013 mA/cm²min from 11.91 mA/cm² (-50 mV) and 11.71 mA/cm² (+50 mV).

Concerning the time constants, an average of 207 ± 22 ms and 17 ± 3 ms for τ_{slow} and τ_{fast} respectively, were determined for – 50 mV and τ_{slow} 239 ± 83 ms and τ_{fast} 23 ± 10 ms +50 mV for the device of web speed 25 cm/min and pump rate 120 µL/min. For the device with a web speed of 25 cm/min and a pump rate of 300 µL/min, the time constants were calculated as τ_{slow} 224 ± 6 ms and τ_{fast} 19.9 ± 0.5 ms for -50 mV, τ_{slow} 100 ± 4 ms and τ_{fast} 15.2 ± 0.9 ms for +50 mV. The time constants are summarized in the table 6 below.

TABLE 7. Time constant values obtained from the fitting of the transient response of the current density.

Performance	Sample	Step (mV)	τ_{fast} (ms)	τ_{slow} (ms)
Lower	Web speed 25 cm/min Pump rate 300 µL/min	-50	19.9 ± 0.5	224 ± 6
		+50	15.2 ± 0.9	100 ± 4
Higher	Web speed 25 cm/min Pump rate 120 µL/min	-50	17 ± 3	207 ± 22
		+50	23 ± 10	239 ± 83

Additionally, in Figure 37, the HI for different delay times, as presented in Table 8, is also compared with the transient behavior (calculated accordingly with Equation 6).

TABLE 8. Diverse time parameters for the J-V scans used in the analysis of the changes in the hysteresis index.

Voltage Step Size (mV)	t_s - Integration / Sampling Time (ms)	t_d - Settling / Delay Time (ms)	Scan Rate (V/s)
20	20.00	40.00	0.33
50	0.20	0.10	166.67
	0.20	1.00	41.67
	1.00	10.00	4.55
	2.00	100.00	0.49
	10.00	1000.00	0.05
	20.00	3000.00	0.02

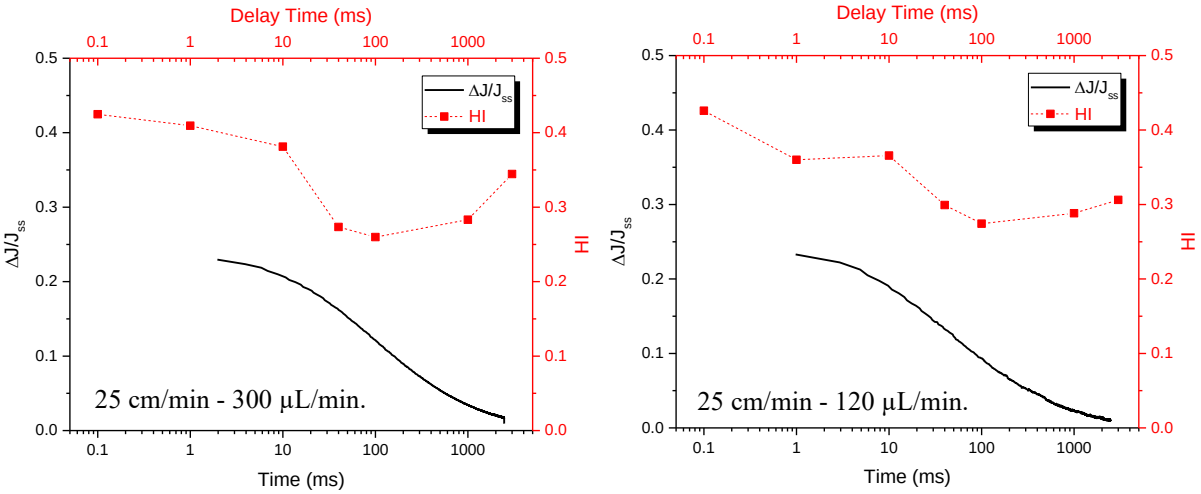

FIGURE 37. The relative discrepancy between the reverse and forward transient current ($\Delta J/J_{ss}$) in time (left y and bottom x-axis) correlated with the hysteresis index at each delay time (right y and top x-axis) for the sample coated with a) web speed of 25 cm/min and pump rate of 125 µL/min and b) web speed of 25 cm/min and pump rate of 300 µL/min.

For both devices, the transient response discrepancies are lower than the J-V scan discrepancies, i.e., hysteresis index, for different delay times. In addition, meanwhile, the transient response goes towards 0 for higher times, and the HI increases again. Furthermore, it is important to consider that a higher delay time implies a longer time for the J-V measurements cycling. From the MPPT, it was noticeable that this longer time affects the device performance, decreasing it. This may indicate a change in the charge carrier extraction over time (DAGAR et al., 2019).

It is possible to note a minimum of the HI closer to 0.1 s, considering this the delay time that approaches the most from the τ_{slow} constant obtained from the TrAMPPT analysis, which shows the potential of this analysis to reach the steady-state and dynamic response of the device and estimate the optimal delay time to be used for the J-V curves. In addition, the lowest HI point is in accordance with the case that τ_{slow} indicates a delay time that might be optimal for the J-V scan. Moreover, the fact that the hysteresis increase while the transient current decrease for the higher times serves as an additional indication that capacitive phenomena with different time scales are affecting the device performance.

3.2 SnO_2 as ETL and the KCl Passivation

The use of salts, either as a passivation layer between the transport layer and the perovskite or as an additive at the perovskite solution, can be a way to reduce the effects of hysteresis and improve the device's performance (DAGAR et al., 2019). Potassium chloride

(KCl) is one of those salts that proved beneficial for the device's performance (DAGAR et al., 2019). In this work, the KCl is implemented in both ways i.e., the passivation layer and additive with different concentrations, to analyze and compare its effects in the device.

Regarding the role of the KCl addition, it can be separated into the effect caused by the potassium and the chloride. Considering the chloride ion (Cl^-) it is reported that, although it is unclear its presence due to the difficulty in finding it, the chloride usually shows improvement in the perovskite homogeneity and crystallinity (PETRUS et al., 2017; WANG et al., 2018). Concerning the potassium ion (K^+), it is reported that it mainly passivates defects related to iodine (I^-) mobile ions and improves the charge carrier extraction in the electron selective contact, therefore affecting especially the hysteresis (DAGAR et al., 2019; LEE et al., 2018).

3.2.1 SEM measurements

For comparison purposes, the structure of the layers without and with KCl were evaluates. The results are presented in the Figures 38 - 42.

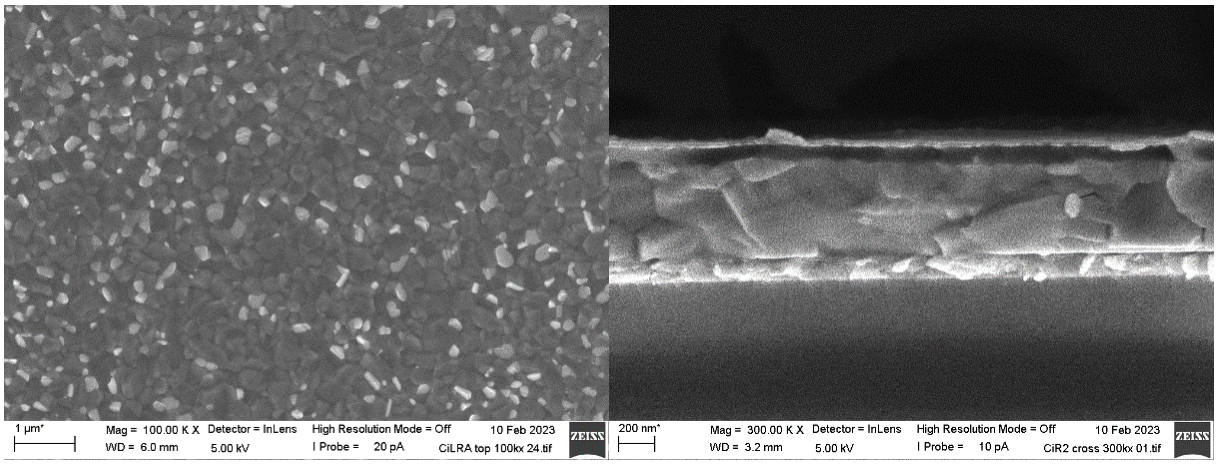

FIGURE 38 The scanning electron microscopy images of the n-i-p reference (SnO_2 followed by the perovskite layers) device: a) the surface image; b) cross-section image.

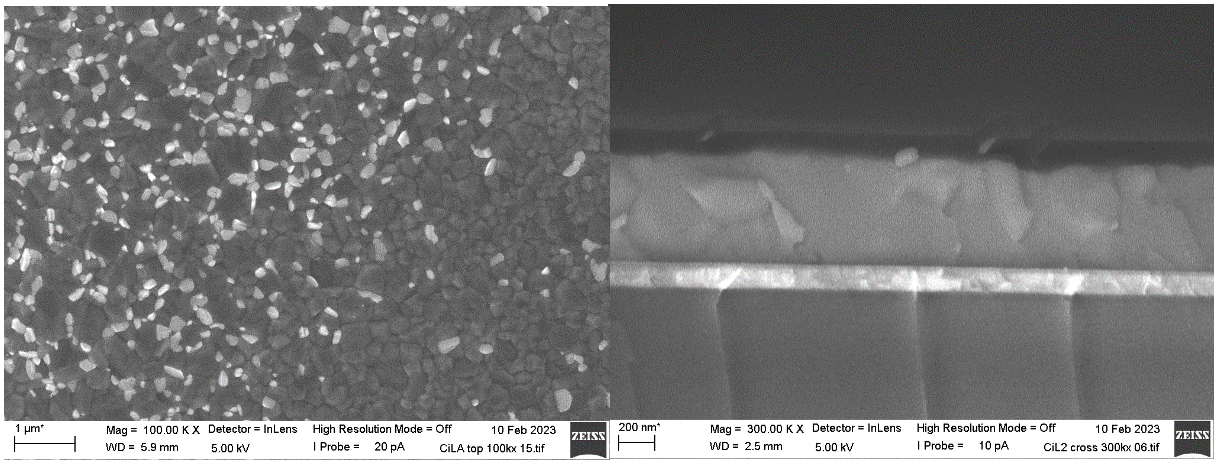

FIGURE 39. The scanning electron microscopy images of the KCl layer device (SnO_2 followed by KCl and then perovskite layers): a) the surface image; b) cross-section image.

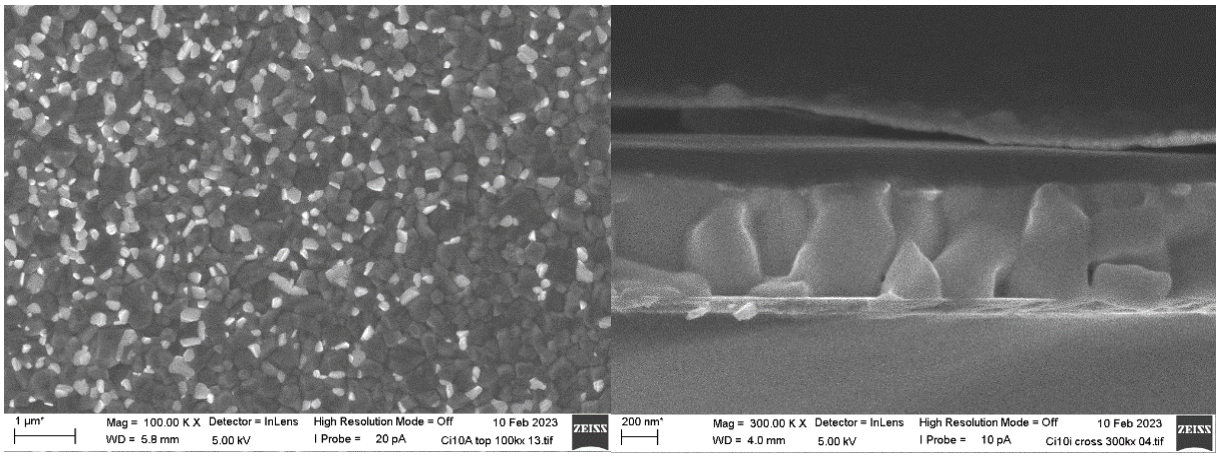

FIGURE 40. The scanning electron microscopy images of the KCl mixed with perovskite device (SnO_2 followed by perovskite mixed with 1.0 mg/mL of KCl): a) the surface image; b) cross-section image.

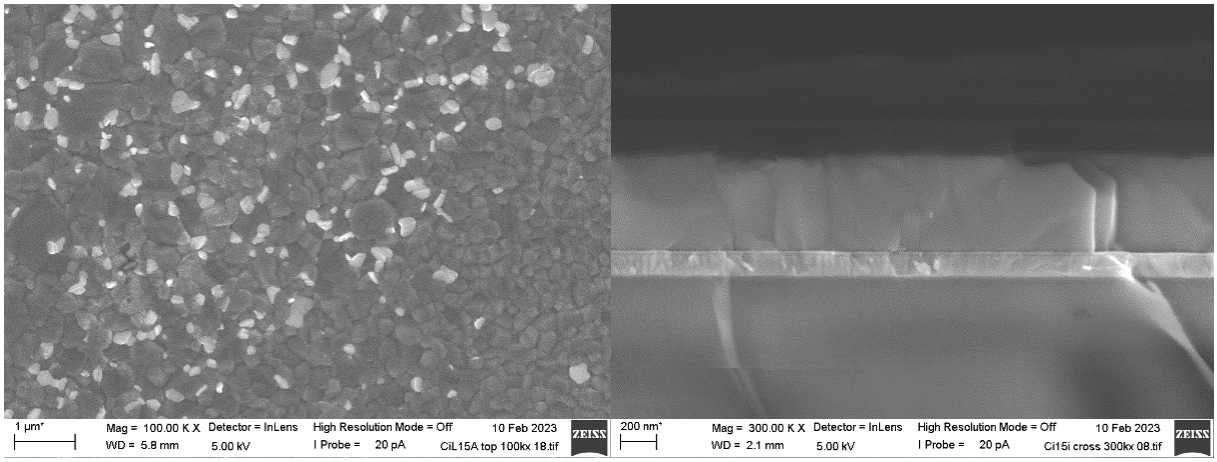

FIGURE 41. The scanning electron microscopy images of the KCl mixed with perovskite device (SnO_2 followed by perovskite mixed with 1.5 mg/mL of KCl): a) the surface image; b) cross-section image.

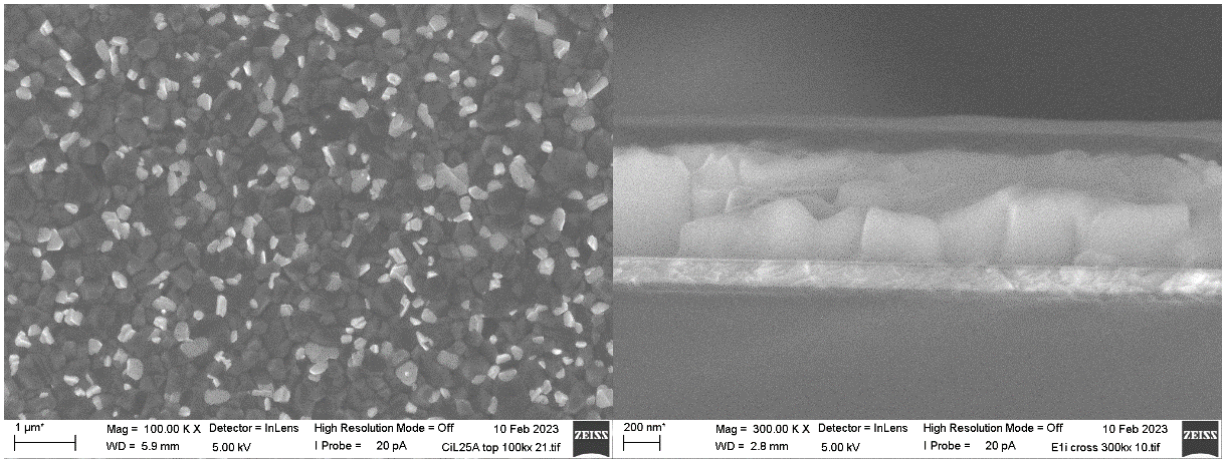

FIGURE 42. The scanning electron microscopy images of the KCl mixed with perovskite device (SnO_2 followed by perovskite mixed with 2.5 mg/mL of KCl): a) the surface image; b) cross-section image.

From the surface image, it seems that the reference sample, which has only the tin oxide (SnO_2) and the perovskite on top of it without any KCl addition, presents smaller grains when compared with the others. That can also be seen from the cross-section view. Concerning the brighter grains, since it is noted in all the samples, it is believed that they are related to some phase segregation of the perovskite layer or signs of the beginning of degradation and not related to the KCl.

In the cross-sections image, it is possible to note that Figure 38 shows a smaller and more random distribution of the grain denoted by the grain boundaries. It indicates that the KCl helps the growth and crystallization of the perovskite layers.

Regarding the thickness, all the samples present similar values for the SnO_2 and Spiro-OMeTAD, about 30 nm and 100 nm, respectively. For the perovskite layer, in the reference sample, it is about 500 nm, and for the samples with KCl, either the one with the layer or the other with the addition in the solution, the perovskite layer is around 600 nm. Table 9 summarizes the average thickness value for each layer of the different devices. The thickness was estimated using five distinct points from the SEM cross-section. The ETL layer in the reference and 1.0 mg/mL mixed KCl were not possible to identify, thus, the values are not specified.

TABLE 9. Thickness values of the layers and their respective standard deviations estimated from five different positions of the cross-section SEM measurement of the devices.

SEM Thickness Estimative			
Sample	**Layer**	**Thickness (nm)**	**Standard Deviation (± nm)**
SnO_2 - Reference	FTO + SnO_2	125	7
	Perovskite	523	22
	Spiro+Au	117	10
SnO_2 – KCl 1.0 mg/mL	FTO + SnO_2	91	5
	Perovskite	646	28
	Spiro+Au	216	22
SnO_2 – KCl 1.5 mg/mL	FTO	121	5
	SnO_2	20	5
	Perovskite	533	13
	Spiro+Au	218	5
SnO_2 – KCl 2.5 mg/mL	FTO	126	4
	SnO_2	23	5
	Perovskite	627	13
	Spiro+Au	173	14
SnO_2 / KCl Layer	FTO	114	3
	SnO_2	25	4
	Perovskite	579	16
	Spiro+Au	125	6

The influence of the layer on the device performance will be discussed with the J-V curves in the next topic.

3.2.2 Devices J-V curves

The J-V curves of each pixel for the reference sample and KCl as a layer are shown in Figure 43, and for the samples where the KCl was mixed with different concentrations in the perovskite solution, the curves are shown in Figure 44. The parameters of each set of samples are presented in Tables 10 and 11, following the respective figures.

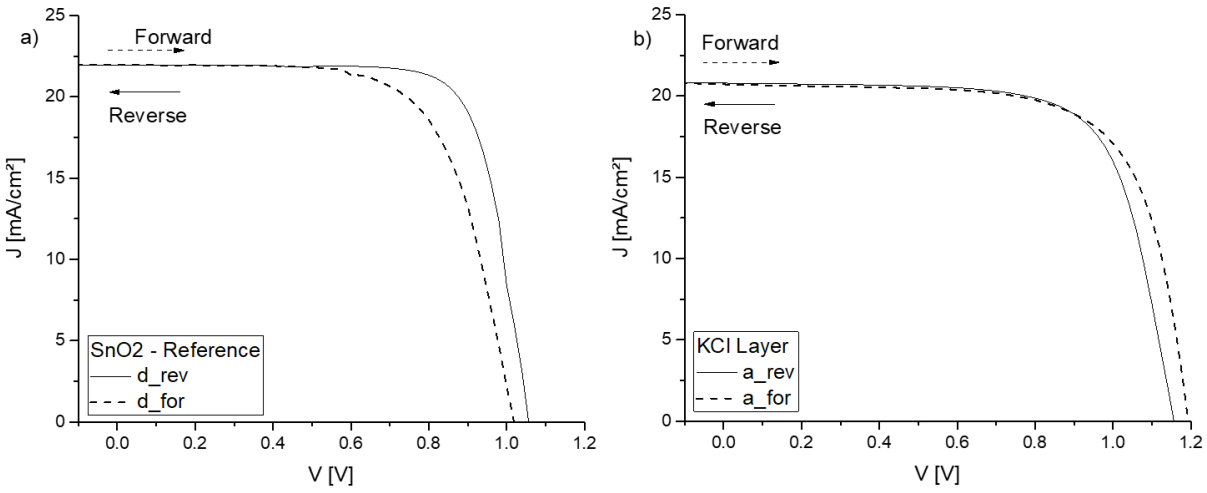

FIGURE 43. Current density versus voltage curve in reverse and forward scans of best pixel for the n-i-p a) reference (SnO_2 followed by the perovskite layers) and b) KCl mixed with perovskite (SnO_2 followed by KCl and then perovskite layers) devices.

TABLE 10. The best pixel parameters obtained from the current density versus voltage curve in reverse and forward scans for the n-i-p reference (left - SnO_2 followed by the perovskite layers) and KCl layer device (right - SnO_2 followed by KCl and then perovskite layers) devices.

SnO2 - Reference		
Parameter	Rev	For
J_{sc} (mA/cm²)	22.0	22.0
V_{oc} (V)	1.1	1.0
Fill factor (%)	75.8	66.9
Efficiency (%)	17.6	15.0
Rsh (Ohmcm²)	22.47	5.22
Rs (mOhmcm²)	5.57	7.36
HI	0.15	

SnO_2 / KCl Layer		
Parameter	Rev	For
J_{sc} (mA/cm²)	20.8	20.7
V_{oc} (V)	1.2	1.2
Fill factor (%)	71.0	70.0
Efficiency (%)	17.1	17.3
Rsh (Ohmcm²)	3.86	1.83
Rs (mOhmcm²)	10.56	5.40
HI	-0.01	

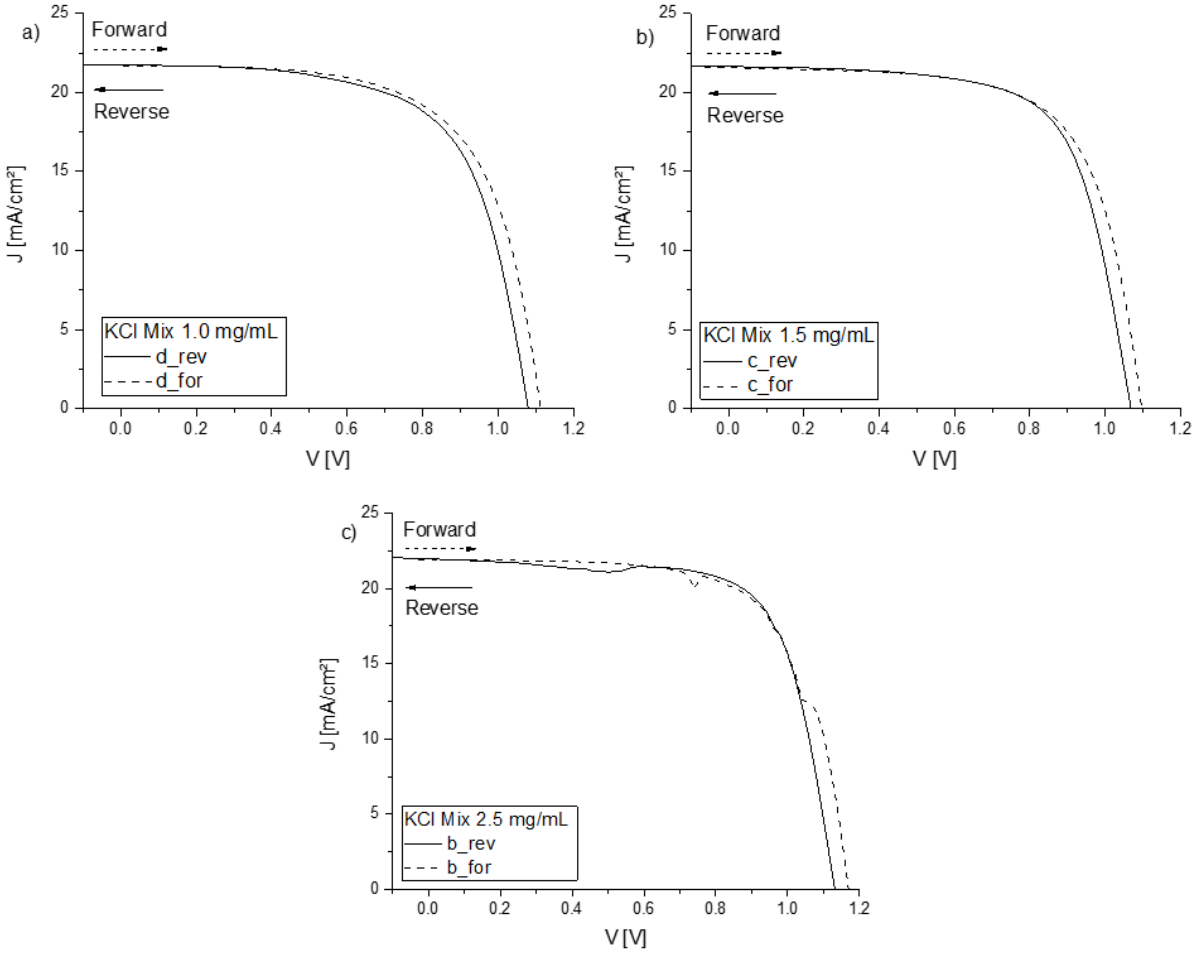

FIGURE 44. Current density versus voltage curve in reverse and forward scans of the best pixel of the KCl mixed with perovskite device. a) SnO_2 followed by perovskite mixed with 1.0 mg/mL of KCl. b) SnO_2 followed by perovskite mixed with 1.5 mg/mL of KCl. c) SnO_2 followed by perovskite mixed with 2.5 mg/mL of KCl.

TABLE 11. The best pixel parameters obtained from the current density versus voltage curve in reverse and forward scans for the n-i-p SnO_2 followed by perovskite mixed with 1.0 mg/mL, 1.5 mg/mL, and 2.5 mg/mL of KCl.

SnO2 – KCl 1.0 mg/mL			SnO2 – KCl 1.5 mg/mL			SnO2 – KCl 2.5 mg/mL		
Parameter	Rev	For	Parameter	Rev	For	Parameter	Rev	For
J_{sc} (mA/cm²)	21.7	21.7	J_{sc} (mA/cm²)	21.7	21.6	J_{sc} (mA/cm²)	22.0	21.9
V_{oc} (V)	1.1	1.1	V_{oc} (V)	1.1	1.1	V_{oc} (V)	1.1	1.2
Fill factor (%)	64.7	64.6	Fill factor (%)	67.9	67.3	Fill factor (%)	70.8	67.9
Efficiency (%)	15.2	15.6	Efficiency (%)	15.7	15.9	Efficiency (%)	17.6	17.4
Rsh (Ohmcm²)	6.64	3.64	Rsh (Ohmcm²)	2.93	1.53	Rsh (Ohmcm²)	1.15	3.02
Rs (mOhmcm²)	7.14	5.82	Rs (mOhmcm²)	8.13	6.37	Rs (mOhmcm²)	7.85	4.65
HI	-0.03		HI	-0.01		HI	0.01	

It is clear the beneficial effect of the KCl implementation on the samples. Although the concentration of 1.0 mg/mL and 1.5 mg/mL shows a slightly lower PCE and fill factor, the J_{sc} and V_{oc} are similar, and the HI improvement was notable. Furthermore, the samples with a concentration of 2.5 mg/mL for the KCl layer and for the addition in the perovskite solution showed similar performance and an outstanding result compared with the others, which highlights the benefit of using higher concentrations.

Concerning the fact that the use of the KCl as a passivation layer or an additive had similar performance may indicate that the spin-coating of the separated solution might not result in the formation of a homogeneous layer that expressive interferes in the charge extraction. Instead, the role of KCl seems similar in both cases, most probably acting mainly as ionic defect passivation (DAGAR et al., 2019; KANG; PARK, 2019; KIM et al., 2022), as mentioned previously. However, whether the KCl interferes with the I^- at the interface or in the bulk remains unclear.

It is worth mentioning that the hysteresis is much lower for the devices with KCl, resulting from the ionic vacancies and defect reduction (KANG; PARK, 2019; KIM et al., 2022; LEE et al., 2018; SNAITH et al., 2014). Thus, it highlights the possible role of using this salt as an enhancer of stability in the n-i-p devices. However, to achieve this conclusively and completely understand the mechanisms of passivation, complementary analysis should be done. In addition, it is possible to note not only the hysteresis reduction but also the change from positive to negative values. This results from the improvement of the performance of the forward scan. However, this might happen due to differences in the device capacitance, which can originate from the modification of the charge and discharge of trapped charges due to the reduction in the effects of the iodine-mobile ions (SNAITH et al., 2014). The statistical analysis of the parameters related to each pixel of the devices is presented in Figure 45.

To complement the HI analysis, the MPPT was performed and will be presented in the next section.

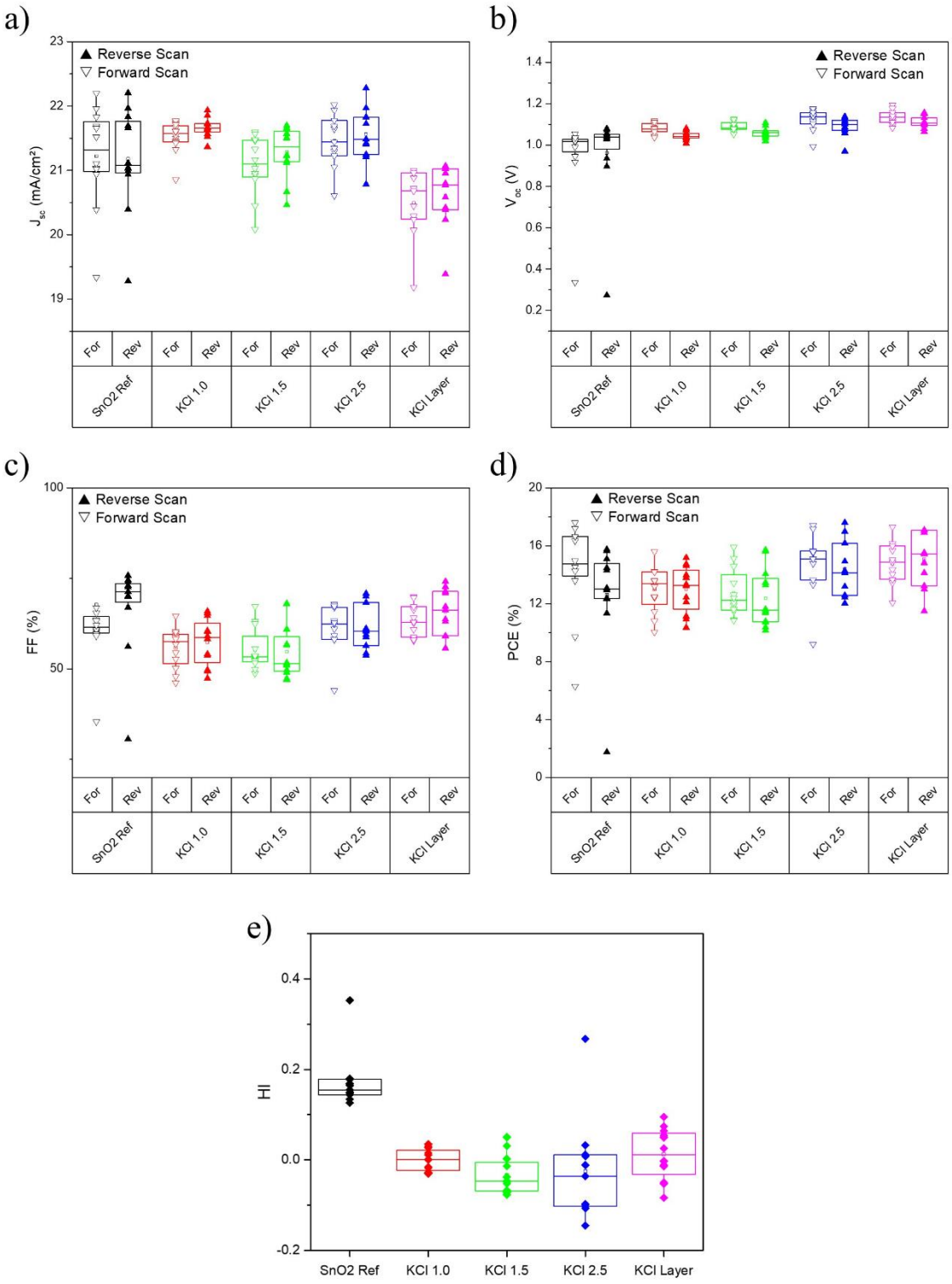

FIGURE 45. Statistic results obtained from the J-V curves of a) J_{sc}, b) V_{oc}, c) FF, d) PCE, and e) Hysteresis index for the SnO_2 reference and all the samples with different incorporation of KCl

3.2.3 MPP Tracking

For a look at the short-term stability of the devices, the MPPT measurements of the best pixel of each sample were done. Figures 46 - 50 present those results.

It is possible to note that the performance of the reference device decays through time. Otherwise, the devices based on the KCl addition present a high disturbance, followed by a stabilization of the performance with a slight improvement of the overall performance. This observation provides further evidence that the stability enhancement effect with KCl has been achieved, although the specific implementation method of KCl appears to be less critical compared to the concentration utilized.

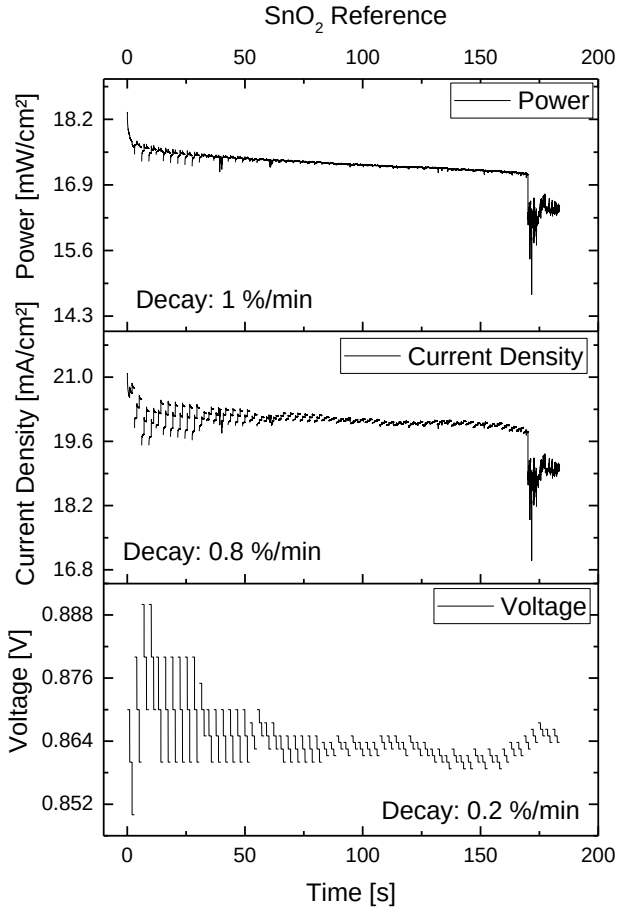

FIGURE 46. Power, current density, and voltage vs time from the MPPT for the n-i-p reference (SnO_2 followed by the perovskite layers) device.

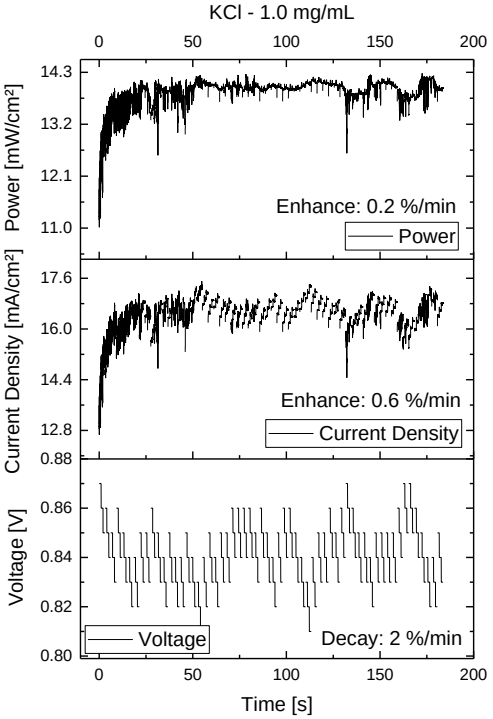

FIGURE 47. Power, current density, and voltage vs time from the MPPT for the KCl mixed with perovskite device (SnO_2 followed by perovskite mixed with 1.0 mg/mL of KCl).

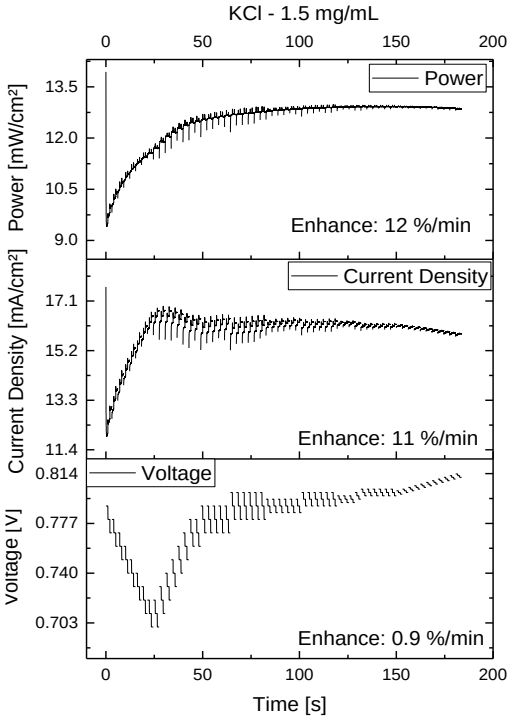

FIGURE 48. Power, current density, and voltage vs time from the MPPT for the KCl mixed with perovskite device (SnO_2 followed by perovskite mixed with 1.5 mg/mL of KCl).

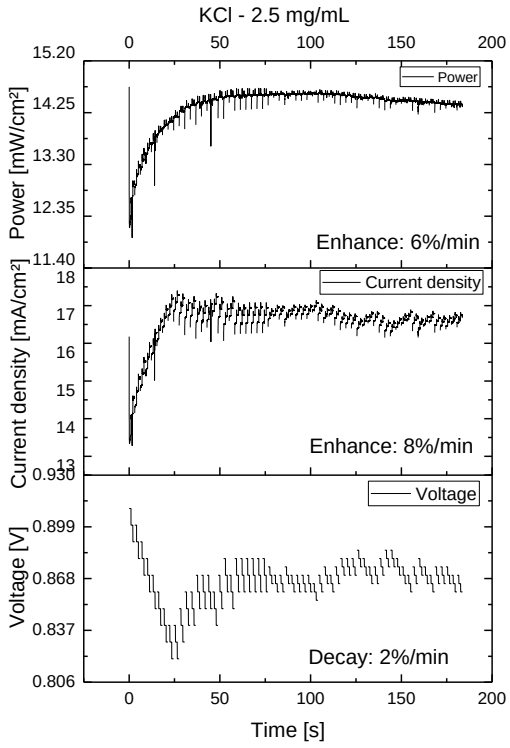

FIGURE 49. Power, current density, and voltage vs time from the MPPT for the KCl mixed with perovskite device (SnO_2 followed by perovskite mixed with 2.5 mg/mL of KCl).

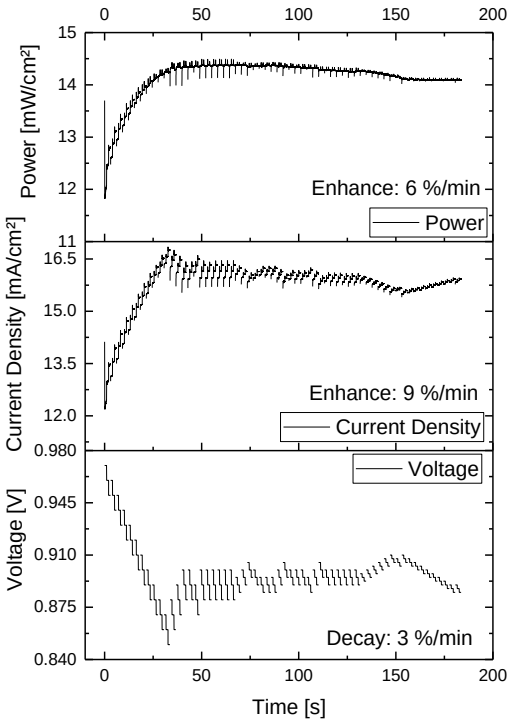

FIGURE 50. Power, current density, and voltage vs time from the MPPT for the KCl layer device (SnO_2 followed by KCl and then perovskite layers).

3.2.4 External Quantum Efficiency

To evaluate the photon conversion, EQE was measured in function of the wavelength, and it is presented in Figure 51. It is possible to note that the curves have similar shapes, which indicates no expressive optical changes in the samples. Nevertheless, the reference (without KCl), the sample with KCl layer and the sample with 1.0 mg/mL mixed in the perovskite solution has the maximum efficiency around 410 nm, and the samples with higher concentrations (mixing 1.5 and 2.5 mg/mL) has the maximum around 440 nm.

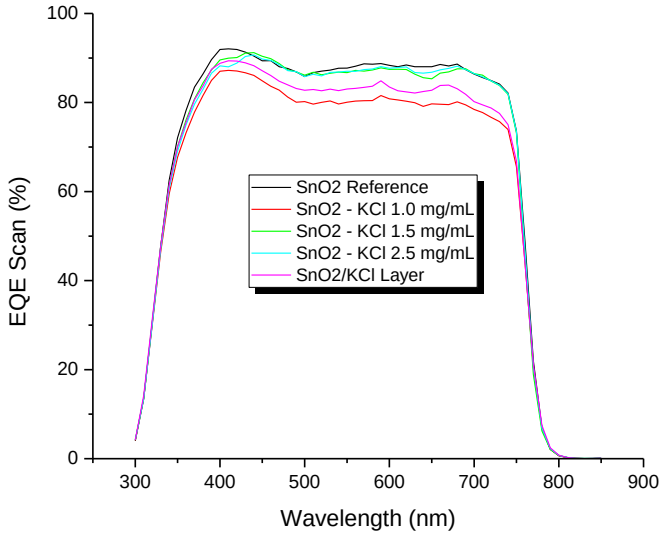

FIGURE 51. External Quantum Efficiency scan. The y-axis on the left represents the result for the SnO_2 reference and all the samples with different incorporation of KCl.

In addition, it is possible to roughly estimate the band gap energy (Eg). All the samples showed Eg = 1.60 ± 0.01 eV. Finally, the curve of the reference device has about 3% higher intensity when compared to the sample with the KCl layer, which might be due to the J_{sc} difference.

4. Conclusions

This thesis primarily delves into the utilization of metal oxides as transport layers in perovskite solar cells, specifically focusing on their role as the electron transport layer (ETL) in n-i-p devices. Two distinct materials, namely niobium pentoxide (Nb_2O_5) and tin dioxide, were employed as ETL , each holding unique characteristics and potential contributions to solar cell performance. The emphasis on Nb_2O_5 pertained to the deposition technique, with a focus on slot die coating for layer application. In the case of SnO_2, attention was directed toward understanding the passivation effects on the ETL and perovskite layer.

Considering the Nb_2O_5 by slot die coating, although some papers indicate satisfactory results of the application of this material, using other deposition techniques (AYDIN et al., 2021; FERNANDES et al., 2022; GUO et al., 2018; LIU et al., 2019; SHEN et al., 2018; ZHAO et al., 2020), reports focusing on the slot die coated Nb_2O_5 in perovskite solar cells could not be found. Therefore, the layers were successfully obtained and applied as ETL in CsFA perovskite devices.

Different deposition parameters were tested. The best result was obtained for 120 µL/min of pumping rate and a web speed of 25 cm/min. Around 12 % of PCE with J_{sc} of 19.9 mA/cm², V_{oc} of 1.07 V, and 57.2 % of fill factor was achieved in this case.

Those results may motivate further performance improvements, making it possible to reach higher values through the optimization of some steps. Testing different solution concentrations and the distance between the blade and substrate is still necessary. The results from other studies in the literature, using distinct deposition techniques, indicate that the most favorable thickness for this layer is 100 nm. Hereby, the thickness estimate was below 50 nm, and controlling the above-mentioned deposition parameters might be a way to increase the thickness.

Considering the scalability, a key advantage of the slot die coating process, there arises the need to explore lower process temperatures for annealing, aligning with the practical requirements of large-scale production. Moreover, a significant advancement could be achieved by manufacturing devices with both the Nb_2O_5 as the ETL and the perovskite layer through slot die coating, showcasing the versatility and efficiency of this technique. Lastly, conducting tests on devices with larger surface areas stands as a pertinent final step, shedding light on the practical implications and potential challenges in scaling up the production process.

Concerning the SnO_2 as ETL and the passivation using potassium chloride, two approaches were used for comparison with a non-passivated device. One was adding the KCl as a separated layer between the SnO_2 and a triple cation perovskite, which works as a passivation layer. While the other was adding the KCl (in three distinct amounts) to the triple cation perovskite precursor solution, the KCl then acting as an additive.

The SEM measurements indicate that the presence of the KCl induces the growth of larger and more uniform grains of the perovskite layers. It was observed that the addition of the KCl, regardless of the method, reduced the hysteresis dramatically. However, no significant improvement in the PCE was noted. This is attributed mainly to the fact that for the KCl to fully dissolve in the perovskite, it was necessary to stir for a longer time during the solution preparation, which might be detrimental to the perovskite.

Nonetheless, the best result was obtained for the concentration of 2.5 mg of KCl per mL. For the device where the KCl was mixed in the perovskite solution, an average PCE of 14.2 % was reached and a HI of 0.04. For the KCl as a passivation layer, the average PCE was 16.0 % and the HI 0.02. Finally, the reference device that was only the ETL of SnO_2, followed by the normal triple cation perovskite, showed an average PCE of 15.7 % and 0.17 HI. So far, these facts have led to the conclusion that it is advantageous to use the KCl as a separated layer. However, another method to mix the KCl might be a possibility that guides to a different outcome.

5. References

ABOU-RAS, D.; KIRCHARTZ, T.; RAU, U. (EDS.). **Advanced Characterization Techniques for Thin Film Solar Cells**. [s.l.] Wiley-VCH Verlag GmbH & Co, 2011.

ALTINKAYA, C. et al. **Tin Oxide Electron-Selective Layers for Efficient, Stable, and Scalable Perovskite Solar Cells**. **Advanced Materials**John Wiley and Sons Inc, , 1 abr. 2021.

AYDIN, E. et al. Ligand-bridged charge extraction and enhanced quantum efficiency enable efficient n-i-p perovskite/silicon tandem solar cells. **Energy and Environmental Science**, v. 14, n. 8, p. 4377–4390, 1 ago. 2021.

CAI, L.; ZHU, F. Toward efficient and stable operation of perovskite solar cells: Impact of sputtered metal oxide interlayers. **Nano Select**, v. 2, n. 8, p. 1417–1436, 4 ago. 2021.

CARVALHO, M. S.; KHESHGI, H. S. Low-flow limit in slot coating: Theory and experiments. **AIChE Journal**, v. 46, n. 10, p. 1907–1917, 2000.

CHAN, D.; PHANG, J. Analytical Methods for the Extraction of Solar-Cell Single-and Double-Diode Model Parameters from I-V Characteristics. **IEEE Transaction on Electron Devices**, v. 34, n. 2, p. 286–293, 1987.

CHANG, Y. R. et al. Three minimum wet thickness regions of slot die coating. **Journal of Colloid and Interface Science**, v. 308, n. 1, p. 222–230, 1 abr. 2007.

CHAVAN, R. D. et al. Mesoscopic TiO2/Nb2O5 Electron Transfer Layer for Efficient and Stable Perovskite Solar Cells. **Advanced Materials Interfaces**, v. 8, n. 10, 1 maio 2021.

CZUDEK, A. et al. **Transient Analysis during Maximum Power Point Tracking (TrAMPPT) to Assess Dynamic Response of Perovskite Solar CellsarXiv preprint arXiv:1906.05028**. [s.l: s.n.].

DAGAR, J. et al. Alkali Salts as Interface Modifiers in n-i-p Hybrid Perovskite Solar Cells. **Solar RRL**, v. 3, n. 9, 1 set. 2019.

DIANTORO, M. et al. Shockley's equation fit analyses for solar cell parameters from I-V curves. **International Journal of Photoenergy**, v. 2018, 2018.

DING, X.; LIU, J.; HARRIS, T. A. L. **A review of the operating limits in slot die coating processes**. **AIChE Journal**John Wiley and Sons Inc., , 1 jul. 2016.

DONG, C.; WANG, Z. K.; LIAO, L. S. **Progress of Triple Cation Organometal Halide Perovskite Solar Cells**. **Energy Technology**Wiley-VCH Verlag, , 1 abr. 2020.

Electrical Characterization of Organic and Perovskite Solar Cells. Disponível em: <https://www.fluxim.com/measurement-techniques-perovskite-solar-cells>. Acesso em: 27 maio. 2023.

ELSEMAN, A. M. et al. **Electron Transport Materials: Evolution and Case Study for High-Efficiency Perovskite Solar Cells**. **Solar RRL**Wiley-VCH Verlag, , 1 jul. 2020.

FERNANDES, S. L. **Desenvolvimento de células solares de perovskita baseadas em filmes de óxidos nanoestruturados**. Araraquara: Universidade Estadual Paulista "Júlio de Mesquita Filho", 2016.

FERNANDES, S. L. et al. Nb2O5 hole blocking layer for hysteresis-free perovskite solar cells. **Materials Letters**, v. 181, p. 103–107, 15 out. 2016.

FERNANDES, S. L. et al. Exploring the properties of niobium oxide films for electron transport layers in perovskite solar cells. **Frontiers in Chemistry**, v. 7, n. FEB, 2019.

FERNANDES, S. L. et al. The role of Nb2O5deposition process on perovskite solar cells. **Journal of Renewable and Sustainable Energy**, v. 14, n. 4, 1 jul. 2022.

FU, Q. et al. **Recent Progress on the Long-Term Stability of Perovskite Solar Cells**. **Advanced Science**John Wiley and Sons Inc., , 1 maio 2018.

GAO, P.; GRÄTZEL, M.; NAZEERUDDIN, M. K. **Organohalide lead perovskites for photovoltaic applications**. **Energy and Environmental Science**Royal Society of Chemistry, , 2014.

GARCIA, L. DE O. **Estudo e caracterização de células solares de perovskitas de cátions mistos**. Bauru: Universidade Estadual Paulista "Júlio de Mesquita Filho", 2022.

GIL, B. et al. **Recent Progress in Inorganic Hole Transport Materials for Efficient and Stable Perovskite Solar Cells**. **Electronic Materials Letters**The Korean Institute of Metals and Materials, , 10 set. 2019.

GIUSTINO, F.; SNAITH, H. J. **Toward Lead-Free Perovskite Solar Cells**. **ACS Energy Letters**American Chemical Society, , 9 dez. 2016.

GREEN, M. A.; HO-BAILLIE, A.; SNAITH, H. J. **The emergence of perovskite solar cells**. **Nature Photonics**Nature Publishing Group, , 2014.

GRIFFITH, K. J. et al. Titanium Niobium Oxide: From Discovery to Application in Fast-Charging Lithium-Ion Batteries. **Chemistry of Materials**, v. 33, n. 1, p. 4–18, 12 jan. 2021.

GUERRERO, A. et al. Interfacial Degradation of Planar Lead Halide Perovskite Solar Cells. **ACS Nano**, v. 10, n. 1, p. 218–224, 26 jan. 2016.

GUO, Y. et al. Interface Modification for Planar Perovskite Solar Cell Using Room-Temperature Deposited Nb2O5 as Electron Transportation Layer. **ACS Applied Energy Materials**, v. 1, n. 5, p. 2000–2006, 29 maio 2018.

HABISREUTINGER, S. N.; NOEL, N. K.; SNAITH, H. J. Hysteresis Index: A Figure without Merit for Quantifying Hysteresis in Perovskite Solar Cells. **ACS Energy Letters**, v. 3, n. 10, p. 2472–2476, 12 out. 2018.

HAN, G. S. et al. **Cutting-Edge Studies Toward Commercialization of Large Area Solution-Processed Perovskite Solar Cells**. **Advanced Materials Technologies**John Wiley and Sons Inc, , 2022.

HARTONO, N. T. P. et al. Stability follows efficiency based on the analysis of a large perovskite solar cells ageing dataset. **Nature Communications**, v. 14, n. 1, 1 dez. 2023.

HE, R. et al. **Wide-bandgap organic-inorganic hybrid and all-inorganic perovskite solar cells and their application in all-perovskite tandem solar cells**. **Energy and Environmental Science**Royal Society of Chemistry, , 1 nov. 2021.

HEO, J. H. et al. Hysteresis-less inverted CH3NH3PbI3 planar perovskite hybrid solar cells with 18.1% power conversion efficiency. **Energy and Environmental Science**, v. 8, n. 5, p. 1602–1608, 1 maio 2015.

HUANG, Y. T. et al. Solution-Based Synthesis of Ultrasmall Nb2O5 Nanoparticles for Functional Thin Films in Dye-Sensitized and Perovskite Solar Cells. **Electrochimica Acta**, v. 236, p. 131–139, 10 maio 2017.

IM, J.-H. et al. 6.5% efficient perovskite quantum-dot-sensitized solar cell. **Nanoscale**, v. 3, n. 10, p. 4088, 2011.

JIANG, Q. et al. Surface passivation of perovskite film for efficient solar cells. **Nature Photonics**, v. 13, n. 7, p. 460–466, 1 jul. 2019.

KANG, D. H.; PARK, N. G. **On the Current–Voltage Hysteresis in Perovskite Solar Cells: Dependence on Perovskite Composition and Methods to Remove Hysteresis**. **Advanced Materials**Wiley-VCH Verlag, , 1 ago. 2019.

KE, W.; KANATZIDIS, M. G. **Prospects for low-toxicity lead-free perovskite solar cells**. **Nature Communications**Nature Publishing Group, , 1 dez. 2019.

KIM, H. S.; PARK, N. G. Parameters affecting I-V hysteresis of CH3NH3PbI3 perovskite solar cells: Effects of perovskite crystal size and mesoporous TiO2 layer. **Journal of Physical Chemistry Letters**, v. 5, n. 17, p. 2927–2934, 4 set. 2014.

KIM, J. Y. et al. **High-Efficiency Perovskite Solar Cells**. **Chemical Reviews**American Chemical Society, , 12 ago. 2020.

KIM, S. Y. et al. Effects of potassium treatment on SnO2 electron transport layers for improvements of perovskite solar cells. **Solar Energy**, v. 233, p. 353–362, 1 fev. 2022.

KOJIMA, A. et al. Organometal halide perovskites as visible-light sensitizers for photovoltaic cells. **Journal of the American Chemical Society**, v. 131, n. 17, p. 6050–6051, 6 maio 2009.

LANDAU, L.; LEVICH, B. Dragging of a Liquid by a Moving Plate. Em: **Dynamics of Curved Fronts**. [s.l.] Elsevier, 1988. p. 141–153.

LEE, J. W. et al. Tuning Molecular Interactions for Highly Reproducible and Efficient Formamidinium Perovskite Solar Cells via Adduct Approach. **Journal of the American Chemical Society**, v. 140, n. 20, p. 6317–6324, 23 maio 2018.

LEE, J.-W. et al. The Interplay between Trap Density and Hysteresis in Planar Heterojunction Perovskite Solar Cells. **Nano Letters**, v. 17, n. 7, p. 4270–4276, 12 jul. 2017.

LEE, M. M. et al. Efficient Hybrid Solar Cells Based on Meso-Superstructured Organometal Halide Perovskites. **Science**, v. 338, n. 6107, p. 643–647, 2 nov. 2012.

LEMOS, H. G. et al. Electron transport bilayer with cascade energy alignment based on Nb2O5 –Ti3C2 MXene/TiO2 for efficient perovskite solar cells. **Journal of Materials Chemistry C**, v. 11, n. 10, p. 3571–3580, 2023.

LI, D. et al. **A Review on Scaling Up Perovskite Solar Cells**. **Advanced Functional Materials**John Wiley and Sons Inc, , 1 mar. 2021.

LI, J. et al. Ink Design Enabling Slot-Die Coated Perovskite Solar Cells with >22% Power Conversion Efficiency, Micro-Modules, and 1 Year of Outdoor Performance Evaluation. **Advanced Energy Materials**, v. 13, n. 33, 1 set. 2023.

LI, Y. et al. Efficient, stable formamidinium-cesium perovskite solar cells and minimodules enabled by crystallization regulation. **Joule**, v. 6, n. 3, p. 676–689, 16 mar. 2022.

LIN, C. F. et al. Operating windows of slot die coating: Comparison of theoretical predictions with experimental observations. **Advances in Polymer Technology**, v. 29, n. 1, p. 31–44, mar. 2010.

LIN, L. et al. **Inorganic Electron Transport Materials in Perovskite Solar Cells**. **Advanced Functional Materials**Wiley-VCH Verlag, , 1 jan. 2021.

LIU, X. et al. High Photovoltage Inverted Planar Heterojunction Perovskite Solar Cells with All-Inorganic Selective Contact Layers. **ACS Applied Materials and Interfaces**, v. 11, n. 50, p. 46894–46901, 18 dez. 2019.

MIN, H. et al. Perovskite solar cells with atomically coherent interlayers on SnO2 electrodes. **Nature**, v. 598, n. 7881, p. 444–450, 21 out. 2021.

NICO, C.; MONTEIRO, T.; GRAÇA, M. P. F. **Niobium oxides and niobates physical properties: Review and prospects**. **Progress in Materials Science**Elsevier Ltd, , 1 jul. 2016.

PARK, S. Y.; ZHU, K. **Advances in SnO2 for Efficient and Stable n–i–p Perovskite Solar Cells**. **Advanced Materials**John Wiley and Sons Inc, , 1 jul. 2022.

PATIDAR, R. et al. Slot-die coating of perovskite solar cells: An overview. **Materials Today Communications**, v. 22, 1 mar. 2020.

PETRUS, M. L. et al. **Capturing the Sun: A Review of the Challenges and Perspectives of Perovskite Solar Cells**. **Advanced Energy Materials**Wiley-VCH Verlag, , 23 ago. 2017.

PREMKUMAR, M. et al. A reliable optimization framework for parameter identification of single-diode solar photovoltaic model using weighted velocity-guided grey wolf optimization algorithm and Lambert-W function. **IET Renewable Power Generation**, 2 ago. 2023.

PVEducation. Disponível em: <https://www.pveducation.org/>. Acesso em: 27 maio. 2023.

RAM, J. P.; BABU, T. S.; RAJASEKAR, N. A comprehensive review on solar PV maximum power point tracking techniques. **Renewable and Sustainable Energy Reviews**, v. 67, p. 826–847, jan. 2017.

Reference Air Mass 1.5 Spectra | Grid Modernization | NREL. Disponível em: <https://www.nrel.gov/grid/solar-resource/spectra-am1.5.html>. Acesso em: 27 maio. 2023.

RICHARDS, D. et al. Predicting a process window for the roll-to-roll deposition of solvent-engineered SnO2 in perovskite solar cells. **Materials Advances**, v. 3, n. 23, p. 8588–8596, 23 set. 2022.

RONG, Y. et al. Toward Industrial-Scale Production of Perovskite Solar Cells: Screen Printing, Slot-Die Coating, and Emerging Techniques. **Journal of Physical Chemistry Letters**, v. 9, n. 10, p. 2707–2713, 17 maio 2018.

RUSCHAK, K. J. Limiting flow in a pre-metered coating device. **Chemical Engineering Science**, v. 31, n. 11, p. 1057–1060, 1976.

SCHILEO, G.; GRANCINI, G. **Lead or no lead? Availability, toxicity, sustainability and environmental impact of lead-free perovskite solar cells**. **Journal of Materials Chemistry C**Royal Society of Chemistry, , 7 jan. 2021.

SEONG, J. et al. Practical Design Guidelines for the Development of High-Precision Roll-to-Roll Slot-Die Coating Equipment and the Process. **IEEE Transactions on Components, Packaging and Manufacturing Technology**, v. 6, n. 11, p. 1677–1686, 1 nov. 2016.

SHALAN, A. E. et al. Cobalt Oxide (CoOx) as an Efficient Hole-Extracting Layer for High-Performance Inverted Planar Perovskite Solar Cells. **ACS Applied Materials and Interfaces**, v. 8, n. 49, p. 33592–33600, 14 dez. 2016.

SHAO, Y. et al. Origin and elimination of photocurrent hysteresis by fullerene passivation in CH3NH3PbI3 planar heterojunction solar cells. **Nature Communications**, v. 5, n. 1, p. 5784, 15 dez. 2014.

SHEN, D. et al. Facile Deposition of Nb2O5 Thin Film as an Electron-Transporting Layer for Highly Efficient Perovskite Solar Cells. **ACS Applied Nano Materials**, v. 1, n. 8, p. 4101–4109, 24 ago. 2018.

SHOCKLEY, W.; QUEISSER, H. J. Detailed balance limit of efficiency of p-n junction solar cells. **Journal of Applied Physics**, v. 32, n. 3, p. 510–519, 1961.

SHROTRIYA, V. et al. Accurate Measurement and Characterization of Organic Solar Cells. **Advanced Functional Materials**, v. 16, n. 15, p. 2016–2023, 4 out. 2006.

SNAITH, H. J. et al. Anomalous hysteresis in perovskite solar cells. **Journal of Physical Chemistry Letters**, v. 5, n. 9, p. 1511–1515, 1 maio 2014.

UNGER, E. L. et al. Hysteresis and transient behavior in current-voltage measurements of hybrid-perovskite absorber solar cells. **Energy and Environmental Science**, v. 7, n. 11, p. 3690–3698, 1 nov. 2014.

UNGER, E. L. et al. Current-voltage analysis: lessons learned from hysteresis. Em: **Characterization Techniques for Perovskite Solar Cell Materials**. [s.l.] Elsevier, 2020. p. 81–108.

WANG, P. et al. Boosting the performance of perovskite solar cells through a novel active passivation method. **Journal of Materials Chemistry A**, v. 6, n. 32, p. 15853–15858, 2018.

WANG, R. et al. **A Review of Perovskites Solar Cell Stability**. **Advanced Functional Materials**Wiley-VCH Verlag, , 1 nov. 2019a.

WANG, Z. et al. Solution Processed Nb2O5 Electrodes for High Efficient Ultraviolet Light Stable Planar Perovskite Solar Cells. **ACS Sustainable Chemistry and Engineering**, v. 7, n. 7, p. 7421–7429, 1 abr. 2019b.

WÜRFEL, P.; WÜRFEL, U. **Physics of Solar Cells: From Basic Principles to Advanced Concepts**. Third ed. Weinheim: John Wiley & Sons, 2016.

YANG, C. et al. **Toward Commercialization of Efficient and Stable Perovskite Solar Modules**. **Solar RRL**John Wiley and Sons Inc, , 1 mar. 2022.

YANG, S. et al. Toward a Diagnostic Method for Efficient Perovskite Solar Cells Based on Equivalent Circuit Parameters. **Journal of Physical Chemistry C**, v. 127, n. 12, p. 5663–5675, 30 mar. 2023.

YANG, Z. et al. Slot-die coating large-area formamidinium-cesium perovskite film for efficient and stable parallel solar module. **Science Advances**, v. 7, n. 18, 30 abr. 2021.

ZEISS LSM 900 - Confocal for Materials Research. Disponível em: <https://www.zeiss.com/microscopy/en/products/light-microscopes/confocal-microscopes/lsm-900-for-materials.html#overlay-benefits-884442725>. Acesso em: 27 maio. 2023.

ZHAO, F. et al. Efficient carbon-based planar CsPbBr3 perovskite solar cells with Li-doped amorphous Nb2O5 layer. **Journal of Alloys and Compounds**, v. 842, 25 nov. 2020.

6. Appendix

6.1 Papers

6.1.1 Papers being prepared

Slot-die coating of niobium pentoxide applied as electron selective layer for perovskite solar cells. Authors: Lucas J. Affonço, Silvia L. Fernandes, João P. F. Assunção, Janardan Dagar, Carlos. F. de O. Graeff, José H. D. da Silva1, Eva Unger.

6.1.2 Papers published as collaborator

1. Neto, N. F. A., Calligaris, G. A., Affonço, L. J., Zanatta, A. R., Soares, M. M., & da Silva, J. H. (2023). The role of the substrate on the structure of reactive sputtered Co3O4: From polycrystalline to highly oriented films. Thin Solid Films, 782, 140040.

2. Lemos, H. G., Rossato, J. H., Ramos, R. A., Lima, J. V., Affonço, L. J., Trofimov, S., ... & Graeff, C. F. (2023). Electron transport bilayer with cascade energy alignment based on Nb 2 O 5–Ti 3 C 2 MXene/TiO2 for efficient perovskite solar cells. Journal of Materials Chemistry C, 11(10), 3571-3580.

3. Fernandes, S. L., Garcia, L. D. O., Júnior, R. D. A. R., Affonço, L. J., Bagnis, D., Vilaça, R., ... & Graeff, C. F. (2022). The role of Nb2O5 deposition process on perovskite solar cells. Journal of Renewable and Sustainable Energy, 14(4).

4. Neto, N. F. A., Stegemann, C., Affonço, L. J., Leite, D. M., & Da Silva, J. H. (2022). Role of oxygen flow rate on the structure and stoichiometry of cobalt oxide films deposited by reactive sputtering. Journal of Vacuum Science & Technology A, 40(1).

5. Escaliante, L. C., Pereira, A. L. D. J., Affonço, L. J., & da Silva, J. H. D. (2021). Multilayered TiO 2/TiO 2− x/TiO 2 films deposited by reactive sputtering for photocatalytic applications. Journal of Materials Research, 36, 3096-3108.

6. Çaha, I., Alves, A. C., Affonço, L. J., da Silva, J. H. D., Rodrigues, I. R., Grandini, C. R., ... & Toptan, F. (2021). Degradation behaviour of Ti-12Nb alloy coated with ZnO/TiN double layer. Surface and Coatings Technology, 413, 127104.

7. Fernandes, S. L., Albano, L. G. S., Affonço, L. J., Silva, J. H. D. D., Longo, E., & Graeff, C. F. D. O. (2019). Exploring the properties of niobium oxide films for electron transport layers in perovskite solar cells. Frontiers in Chemistry, 7, 50.

8. Fernandes, S. L., Affonço, L. J., Junior, R. A., da Silva, J. H., Longo, E., & Graeff, C. F. D. O. (2019). Niobium oxide films deposited by reactive sputtering: effect of oxygen flow rate. JoVE (Journal of Visualized Experiments), (151), e59929.

9. Caha, I., Alves, A. C., Affonço, L. J., Lisboa-Filho, P. N., da Silva, J. H. D., Rocha, L. A., ... & Toptan, F. (2019). Corrosion and tribocorrosion behaviour of titanium nitride thin films grown on titanium under different deposition times. Surface and Coatings Technology, 374, 878-888.

6.2 Supplementary data

6.2.1 J-V curves

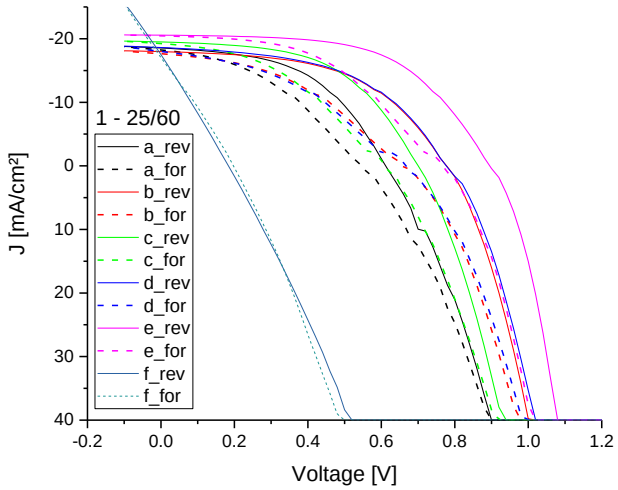

Web speed: 25 cm/min, Pump rate: 60 µL/min.				
Parameter	E Rev.	E For.	Avg. Rev.	Avg. For.
J_{sc} (mA/cm²)	-20.56	-20.46	-19.04 ± 1.01	-18.7 ± 1.14
V_{oc} (V)	0.90	0.77	0.75 ± 0.11	0.65 ± 0.08
Fill Factor (%)	57.10	47.10	52.54 ± 2.74	41.94 ± 2.99
PCE (%)	10.51	7.40	7.60 ± 1.76	5.16 ± 1.30
HI	0.30		0.32	

FIGURE 1. On the left, current density versus voltage curve in reverse and forward scans for all pixels one sample coated at web speed 25 cm/min and pump rate 60 µL/min. On the right side, the values of the respective parameters. The pixel "f" was not taken into account for the average value.

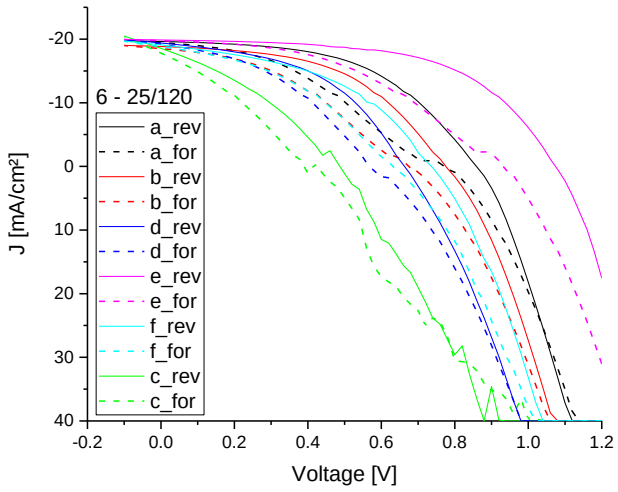

Web speed: 25 cm/min, Pump rate: 120 µL/min.				
Parameter	E Rev.	E For.	Avg. Rev.	Avg. For.
J_{sc} (mA/cm²)	-19.88	-19.75	-19.23 ± 0.50	-18.92 ± 0.70
V_{oc} (V)	1.07	0.93	0.77 ± 0.20	0.66 ± 0.18
Fill Factor (%)	57.25	43.47	47.29 ± 8.03	38.77 ± 3.86
PCE (%)	12.22	8.00	7.26 ± 3.06	4.98 ± 1.86
HI	0.35		0.31	

FIGURE 2. On the left, current density versus voltage curve in reverse and forward scans for all pixels one sample coated at web speed 25 cm/min and pump rate 120 µL/min. On the right side, the values of the respective parameters.

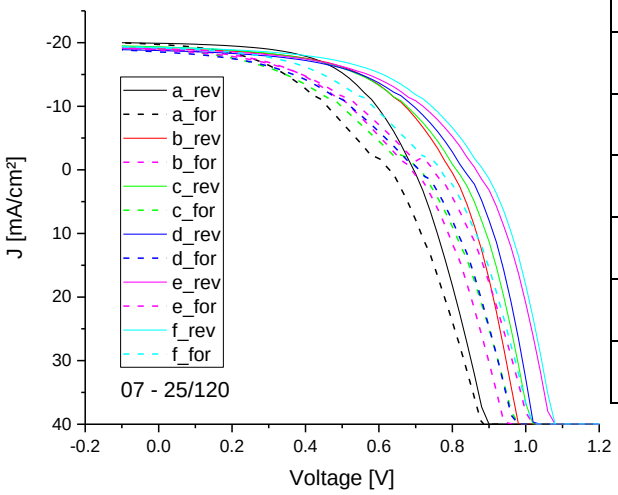

Web speed: 25 cm/min, Pump rate: 120 µL/min.				
Parameter	F Rev.	F For.	Avg. Rev.	Avg. For.
J_{sc} (mA/cm²)	-19.26	-19.16	-19.23 ± 0.39	-19.04 ± 0.39
V_{oc} (V)	0.88	0.77	0.81 ± 0.07	0.71 ± 0.05
Fill Factor (%)	53.77	45.72	53.52 ± 1.36	43.06 ± 2.17
PCE (%)	9.16	6.73	8.35 ± 0.49	5.81 ± 0.54
HI	0.27		0.30	

FIGURE 3. On the left, current density versus voltage curve in reverse and forward scans for all pixels one sample coated at web speed 25 cm/min and pump rate 120 µL/min. On the right side, the values of the respective parameters.

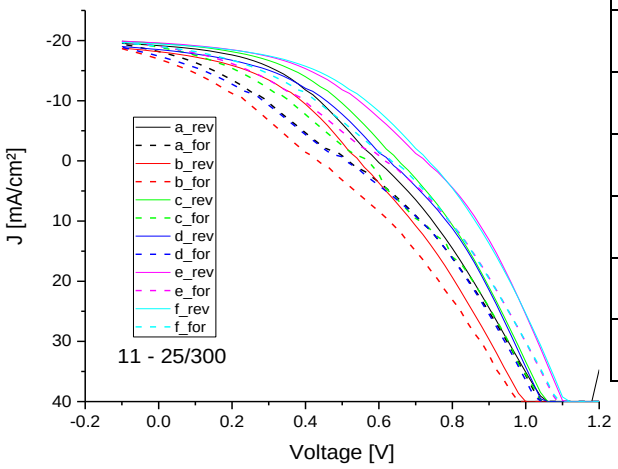

Web speed: 25 cm/min, Pump rate: 300 µL/min.				
Parameter	F Rev.	F For.	Avg. Rev.	Avg. For.
J_{sc} (mA/cm²)	-19.42	-19.02	-19.06 ± 0.60	-18.24 ± 0.91
V_{oc} (V)	0.73	0.63	0.65 ± 0.07	0.55 ± 0.07
Fill Factor (%)	45.57	37.87	43.23 ± 1.51	34.10 ± 2.18
PCE (%)	6.50	4.56	5.37 ± 0.91	3.45 ± 0.82
HI	0.30		0.36	

FIGURE 4. On the left, current density versus voltage curve in reverse and forward scans for all pixels one sample coated at web speed 25 cm/min and pump rate 300 µL/min. On the right side, the values of the respective parameters.

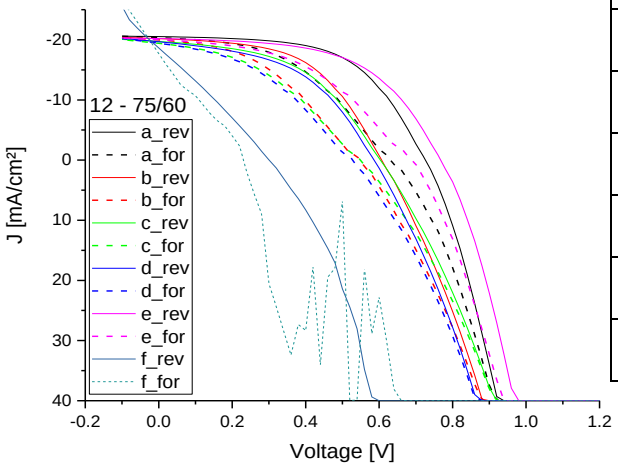

Web speed: 75 cm/min, Pump rate: 60 µL/min.				
Parameter	E Rev.	E For.	Avg. Rev.	Avg. For.
J_{sc} (mA/cm²)	-20.20	-20.01	-20.06 ± 0.36	-19.84 ± 0.41
V_{oc} (V)	0.77	0.69	0.66 ± 0.08	0.59 ± 0.07
Fill Factor (%)	55.69	45.32	52.58 ± 10.88	42.50 ± 2.95
PCE (%)	8.63	6.25	7.00 ± 1.48	5.01 ± 1.00
HI	0.28		0.29	

FIGURE 5. On the left, current density versus voltage curve in reverse and forward scans for all pixels one sample coated at web speed 75 cm/min and pump rate 60 µL/min. On the right side, the values of the respective parameters. The pixel “f” was not considered for the average value.

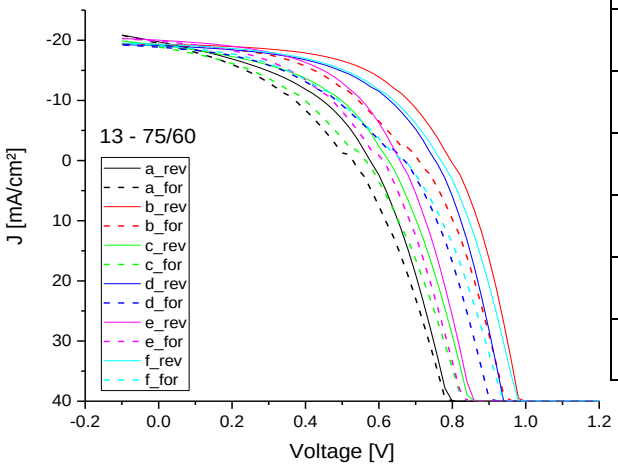

Web speed: 75 cm/min, Pump rate: 60 µL/min.				
Parameter	B Rev.	B For.	Avg. Rev.	Avg. For.
J_{sc} (mA/cm²)	-19.34	-19.22	-19.45 ± 0.35	-19.23 ± 0.38
V_{oc} (V)	0.80	0.71	0.70 ± 0.09	0.62 ± 0.07
Fill Factor (%)	55.39	46.82	49.54 ± 4.78	42.07 ± 3.33
PCE (%)	8.52	6.38	6.76 ± 1.40	5.08 ± 0.91
HI	0.25		0.25	

FIGURE 6. On the left, current density versus voltage curve in reverse and forward scans for all pixels one sample coated at web speed 75 cm/min and pump rate 60 µL/min. On the right side, the values of the respective parameters.

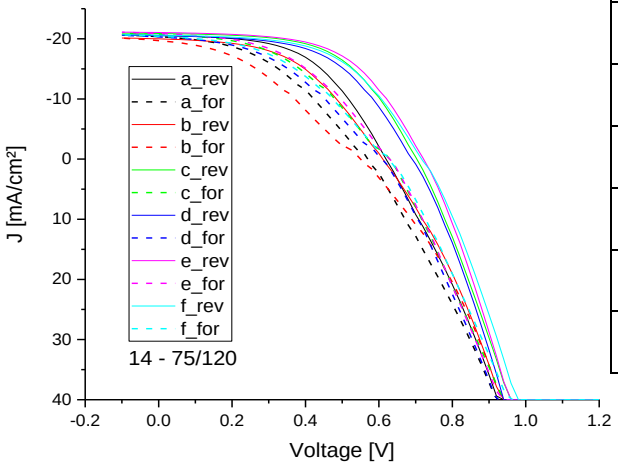

Web speed: 75 cm/min, Pump rate: 120 µL/min.				
Parameter	E Rev.	E For.	Avg. Rev.	Avg. For.
J_{sc} (mA/cm²)	-21.04	-20.87	-20.60 ± 0.36	-20.39 ± 0.41
V_{oc} (V)	0.72	0.63	0.68 ± 0.05	0.60 ± 0.03
Fill Factor (%)	56.45	46.17	54.13 ± 2.73	42.77 ± 2.95
PCE (%)	8.57	6.06	7.58 ± 0.99	5.28 ± 0.72
HI	0.29		0.30	

FIGURE 7. On the left, current density versus voltage curve in reverse and forward scans for all pixels one sample coated at web speed 75 cm/min and pump rate 120 µL/min. On the right side, the values of the respective parameters.

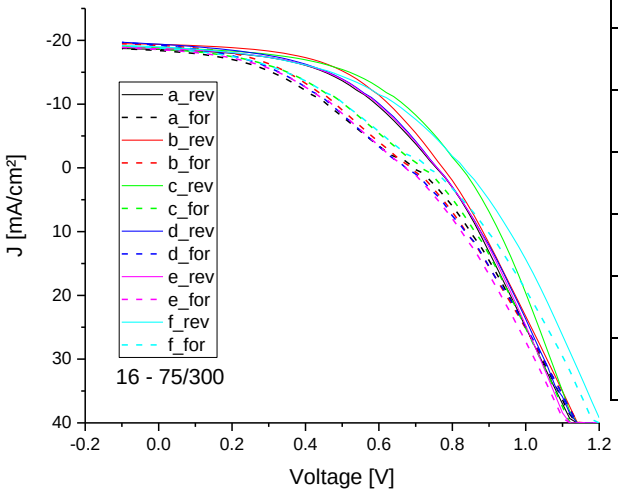

Web speed: 75 cm/min, Pump rate: 300 µL/min.				
Parameter	C Rev.	C For.	Avg. Rev.	Avg. For.
J_{sc} (mA/cm²)	-18.85	-18.66	-18.98 ± 0.34	-18.81 ± 0.35
V_{oc} (V)	0.82	0.72	0.78 ± 0.03	0.70 ± 0.02
Fill Factor (%)	50.47	40.82	48.69 ± 1.83	39.84 ± 0.98
PCE (%)	7.84	5.46	7.24 ± 0.40	5.22 ± 0.23
HI	0.30		0.28	

FIGURE 8. On the left, current density versus voltage curve in reverse and forward scans for all pixels one sample coated at web speed 75 cm/min and pump rate 300 µL/min. On the right side, the values of the respective parameters.

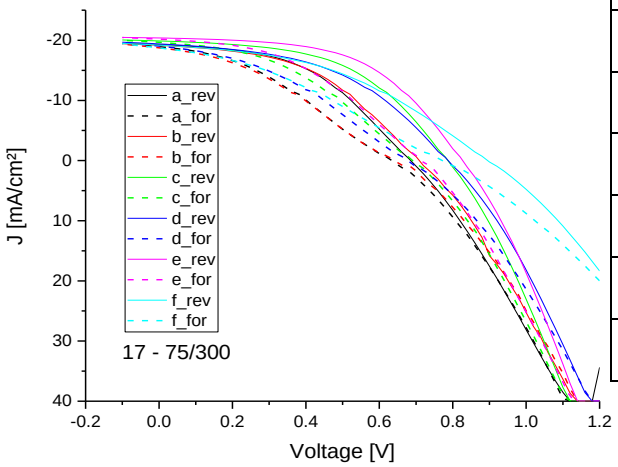

Web speed: 75 cm/min, Pump rate: 300 µL/min.				
Parameter	E Rev.	E For.	Avg. Rev.	Avg. For.
J_{sc} (mA/cm²)	-20.38	-20.18	-19.55 ± 0.49	-19.22 ± 0.58
V_{oc} (V)	0.83	0.71	0.78 ± 0.08	0.69 ± 0.05
Fill Factor (%)	53.38	42.42	47.55 ± 3.94	37.38 ± 3.39
PCE (%)	9.00	6.12	7.28 ± 1.07	4.96 ± 0.75
HI	0.32		0.32	

FIGURE 9. On the left, current density versus voltage curve in reverse and forward scans for all pixels one sample coated at web speed 75 cm/min and pump rate 300 µL/min. On the right side, the values of the respective parameters.

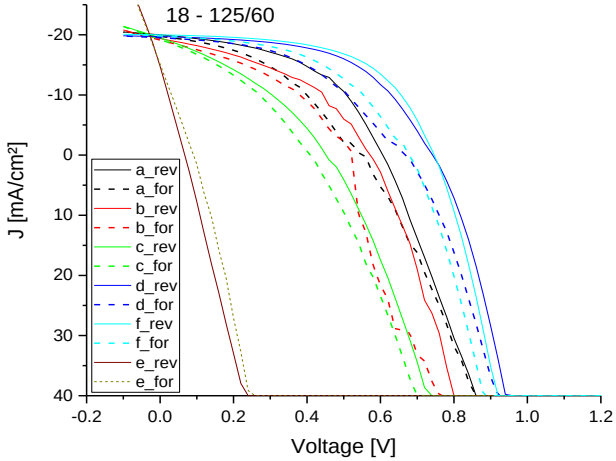

Web speed: 125 cm/min, Pump rate: 60 µL/min.				
Parameter	F Rev.	F For.	Avg. Rev.	Avg. For.
J_{sc} (mA/cm²)	-19.99	-19.81	-19.71 ± 0.28	-19.48 ± 0.31
V_{oc} (V)	0.75	0.68	0.62 ± 0.12	0.57 ± 0.11
Fill Factor (%)	57.37	49.47	47.94 ± 8.89	42.30 ± 5.50
PCE (%)	8.56	6.65	6.08 ± 2.25	4.77 ± 1.55
HI	0.25		0.25	

FIGURE 10. On the left, current density versus voltage curve in reverse and forward scans for all pixels one sample coated at web speed 125 cm/min and pump rate 60 µL/min. On the right side, the values of the respective parameters. The pixel "e" was not taken into account for the average value.

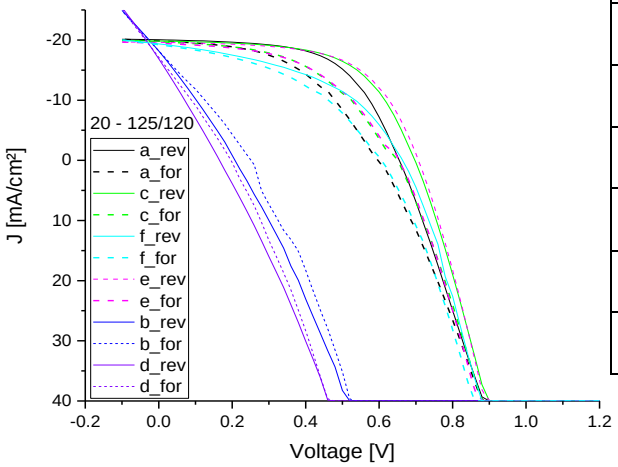

Web speed: 125 cm/min, Pump rate: 120 µL/min.				
Parameter	E Rev.	E For.	Avg. Rev.	Avg. For.
J_{sc} (mA/cm²)	-19.61	-19.46	-19.71 ± 0.29	-19.56 ± 0.27
V_{oc} (V)	0.71	0.65	0.68 ± 0.03	0.63 ± 0.03
Fill Factor (%)	60.29	49.50	56.05 ± 7.09	47.46 ± 3.20
PCE (%)	8.36	6.30	7.54 ± 1.17	5.83 ± 0.62
HI	0.25		0.23	

FIGURE 11. On the left, current density versus voltage curve in reverse and forward scans for all pixels one sample coated at web speed 125 cm/min and pump rate 120 µL/min. On the right side, the values of the respective parameters. The pixels "b" and "d" were not taken into account for the average value.

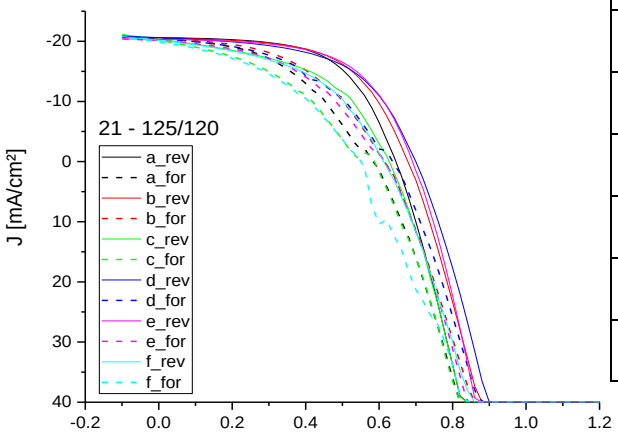

Web speed: 125 cm/min, Pump rate: 120 µL/min.				
Parameter	E Rev.	E For.	Avg. Rev.	Avg. For.
J_{sc} (mA/cm²)	-20.33	-20.10	-20.44 ± 0.19	-20.24 ± 0.22
V_{oc} (V)	0.69	0.61	0.66 ± 0.04	0.60 ± 0.03
Fill Factor (%)	58.87	45.67	54.72 ± 5.17	44.11 ± 3.55
PCE (%)	8.27	5.64	7.40 ± 1.05	5.35 ± 0.68
HI	0.32		0.28	

FIGURE 12. On the left, current density versus voltage curve in reverse and forward scans for all pixels one sample coated at web speed 125 cm/min and pump rate 120 µL/min. On the right side, the values of the respective parameters.

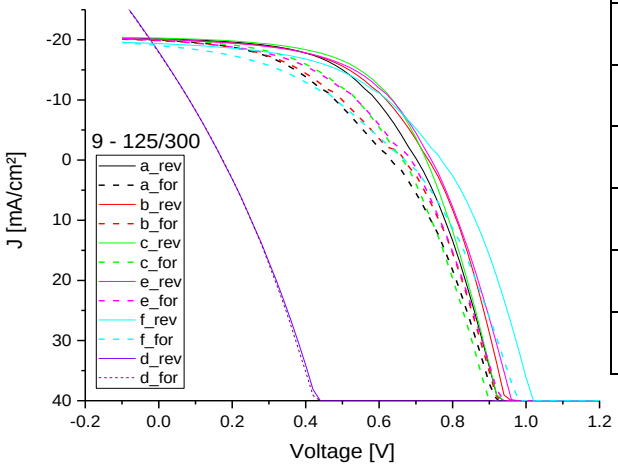

Web speed: 125 cm/min, Pump rate: 300 µL/min.				
Parameter	C Rev.	C For.	Avg. Rev.	Avg. For.
J_{sc} (mA/cm²)	-20.28	-20.09	-19.98 ± 0.36	-19.76 ± 0.42
V_{oc} (V)	0.73	0.66	0.74 ± 0.02	0.66 ± 0.02
Fill Factor (%)	56.22	48.27	53.18 ± 2.47	44.51 ± 2.88
PCE (%)	8.30	6.44	7.81 ± 0.37	8.85 ± 0.52
HI	0.22		0.25	

FIGURE 13. On the left, current density versus voltage curve in reverse and forward scans for all pixels one sample coated at web speed 125 cm/min and pump rate 300 µL/min. On the right side, the values of the respective parameters. The pixel "d" was not taken into account for the average value.

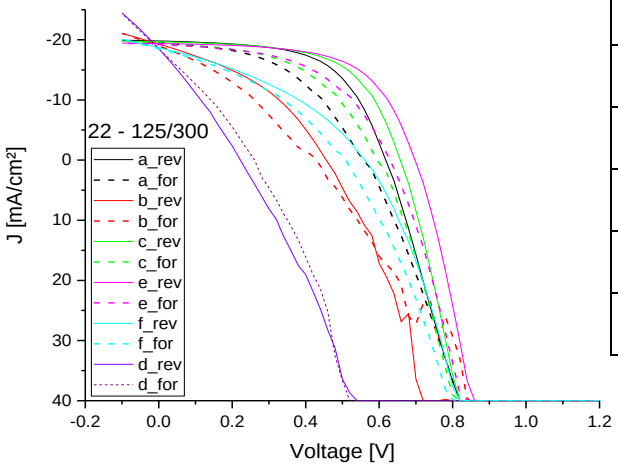

Web speed: 125 cm/min, Pump rate: 300 µL/min.				
Parameter	E Rev.	E For.	Avg. Rev.	Avg. For.
J_{sc} (mA/cm²)	-19.38	-19.20	-19.37 ± 0.43	-19.12 ± 0.41
V_{oc} (V)	0.70	0.63	0.60 ± 0.09	0.54 ± 0.08
Fill Factor (%)	61.10	51.95	51.31 ± 12.20	44.22 ± 8.49
PCE (%)	8.26	6.28	6.12 ± 2.29	4.71 ± 1.55
HI	0.24		0.23	

FIGURE 14. On the left, current density versus voltage curve in reverse and forward scans for all pixels one sample coated at web speed 125 cm/min and pump rate 300 µL/min. On the right side, the values of the respective parameters. The pixel "d" was not taken into account for the average value.

6.2.2 MPPT

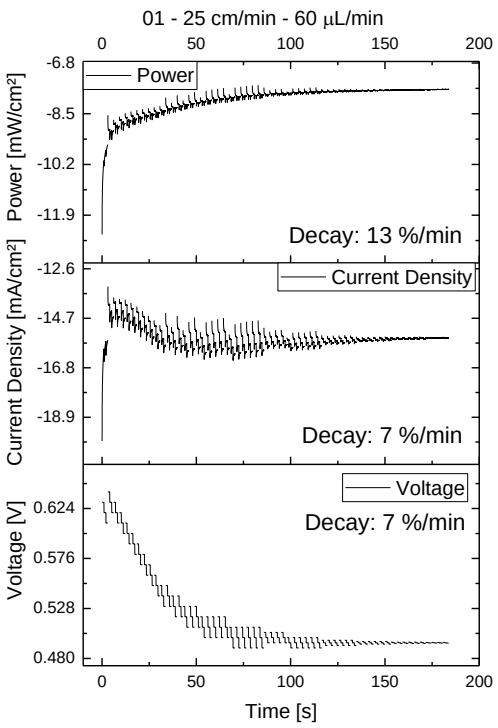

FIGURE 15. Power, Current density and voltage vs time from the MPPT for the best pixel of one sample coated at web speed 25 cm/min and pump rate 60 μL/min.

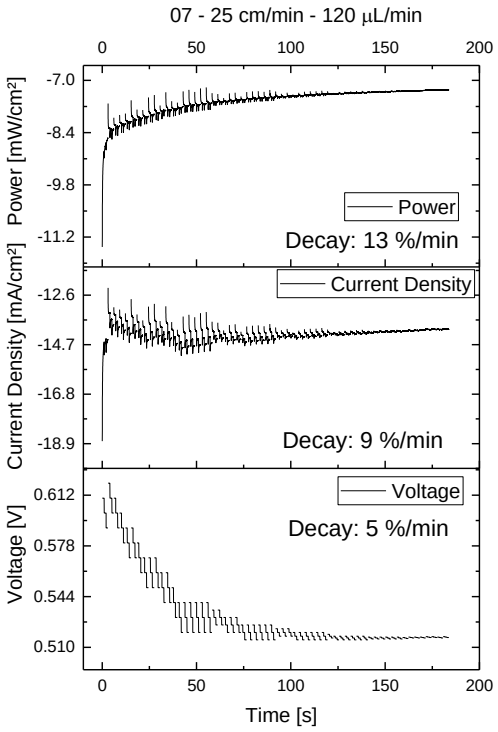

FIGURE 16. Power, Current density and voltage vs time from the MPPT for the best pixel of one sample coated at web speed 25 cm/min and pump rate 120 μL/min.

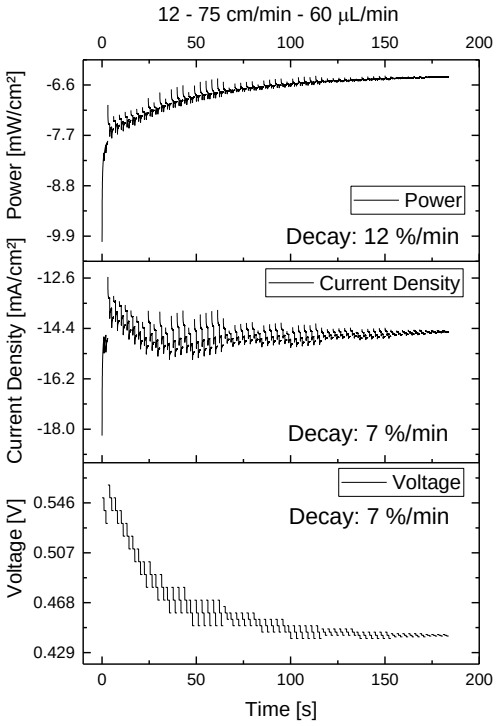

FIGURE 17. Power, Current density and voltage vs time from the MPPT for the best pixel of one sample coated at web speed 75 cm/min and pump rate 60 μL/min.

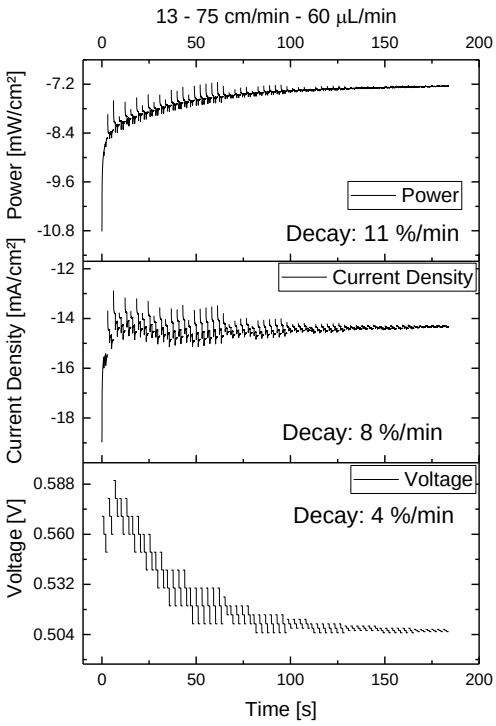

FIGURE 18. Power, Current density and voltage vs time from the MPPT for the best pixel of one sample coated at web speed 75 cm/min and pump rate 60 μL/min.

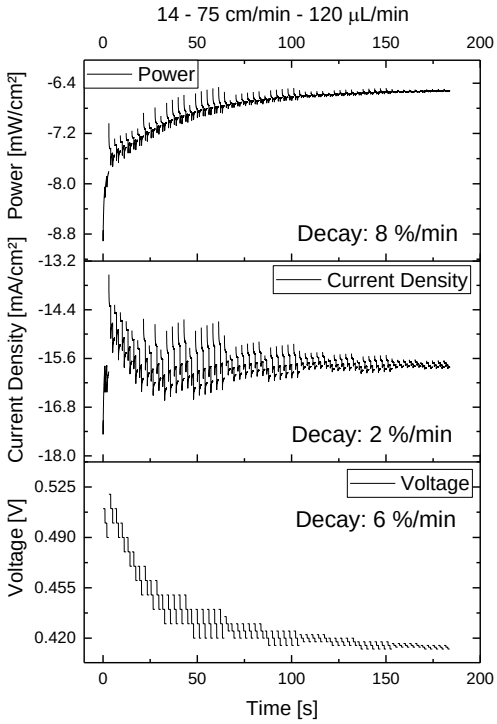

FIGURE 19. Power, Current density and voltage vs time from the MPPT for the best pixel of one sample coated at web speed 75 cm/min and pump rate 120 μL/min.

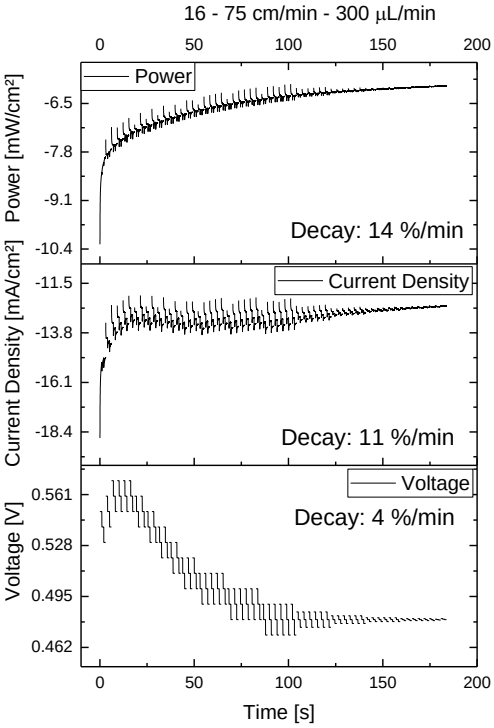

FIGURE 20. Power, Current density and voltage vs time from the MPPT for the best pixel of one sample coated at web speed 75 cm/min and pump rate 300 μL/min.

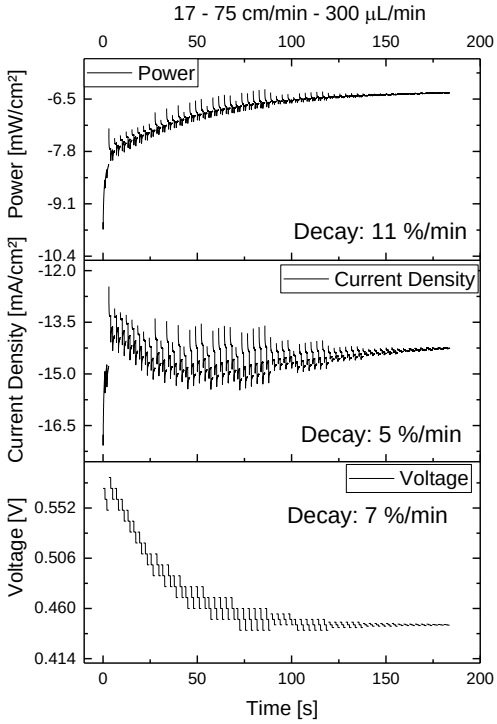

FIGURE 21. Power, Current density and voltage vs time from the MPPT for the best pixel of one sample coated at web speed 75 cm/min and pump rate 300 μL/min.

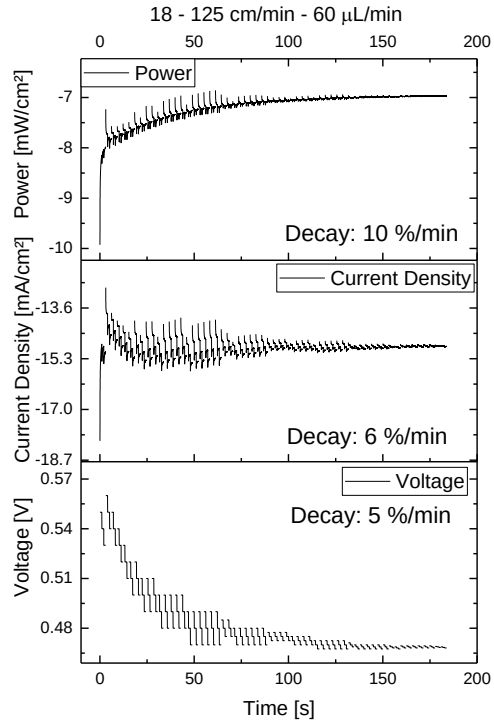

FIGURE 22. Power, Current density and voltage vs time from the MPPT for the best pixel of one sample coated at web speed 125 cm/min and pump rate 60 μL/min.

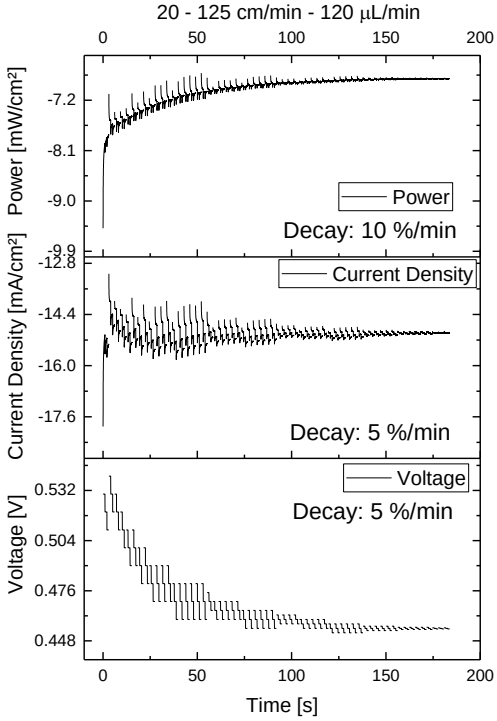

FIGURE 23. Power, Current density and voltage vs time from the MPPT for the best pixel of one sample coated at web speed 125 cm/min and pump rate 120 μL/min.

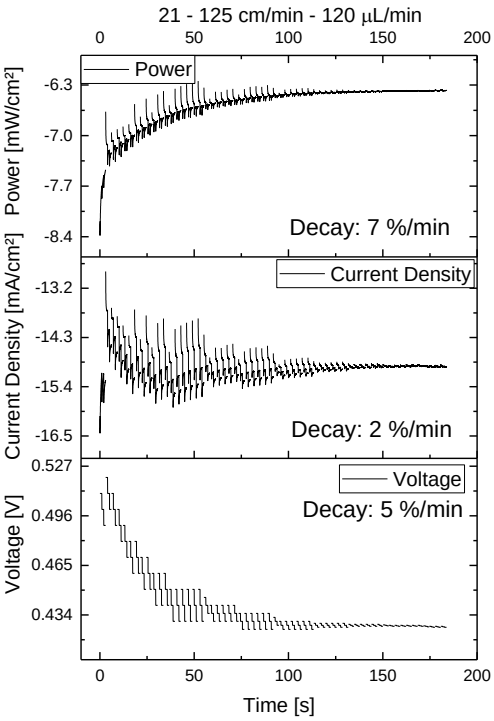

FIGURE 24. Power, Current density and voltage vs time from the MPPT for the best pixel of one sample coated at web speed 125 cm/min and pump rate 120 μL/min.

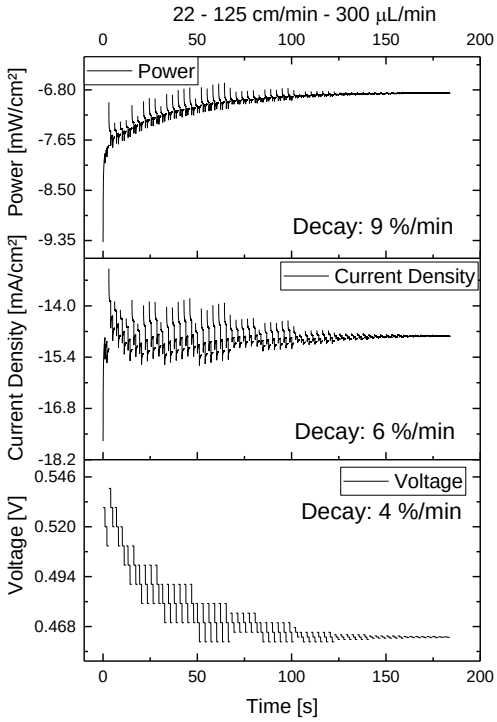

FIGURE 25. Power, Current density and voltage vs time from the MPPT for the best pixel of one sample coated at web speed 125 cm/min and pump rate 300 μL/min.

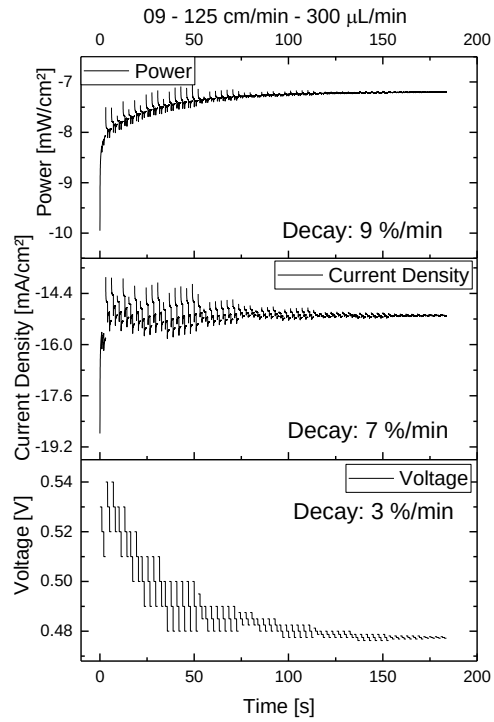

FIGURE 26. Power, Current density and voltage vs time from the MPPT for the best pixel of one sample coated at web speed 125 cm/min and pump rate 300 μL/min.

6.2.3 TrAMPPT

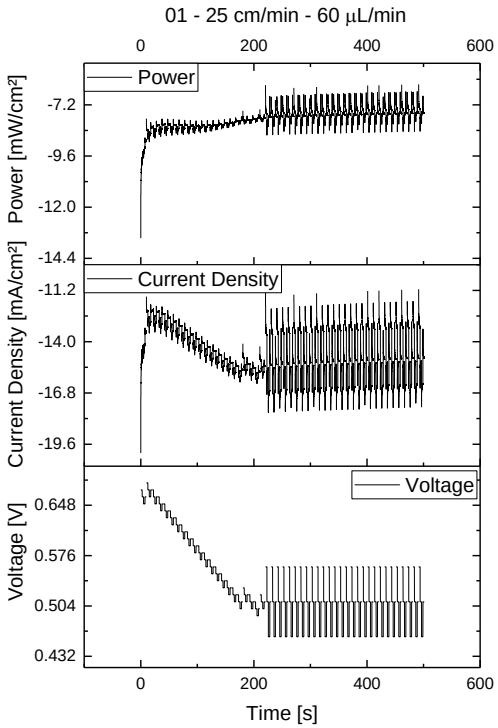

FIGURE 27. Power, Current density and voltage vs time from the TrAMPPT for the best pixel of one sample coated at web speed 25 cm/min and pump rate 60 μL/min.

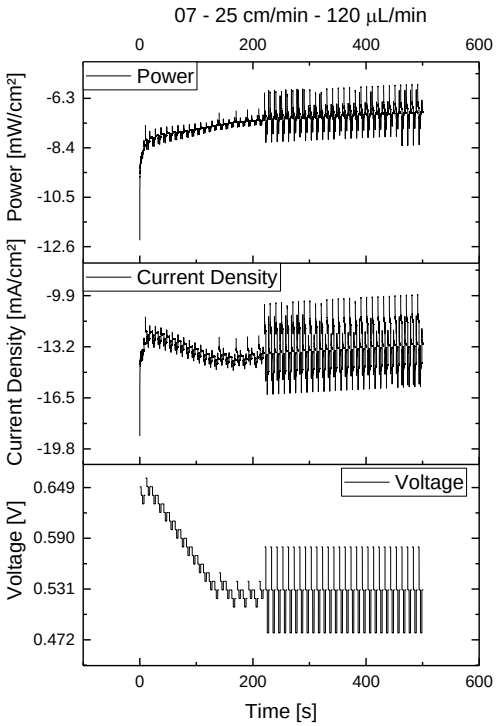

FIGURE 28. Power, Current density and voltage vs time from the TrAMPPT for the best pixel of one sample coated at web speed 25 cm/min and pump rate 120 μL/min.

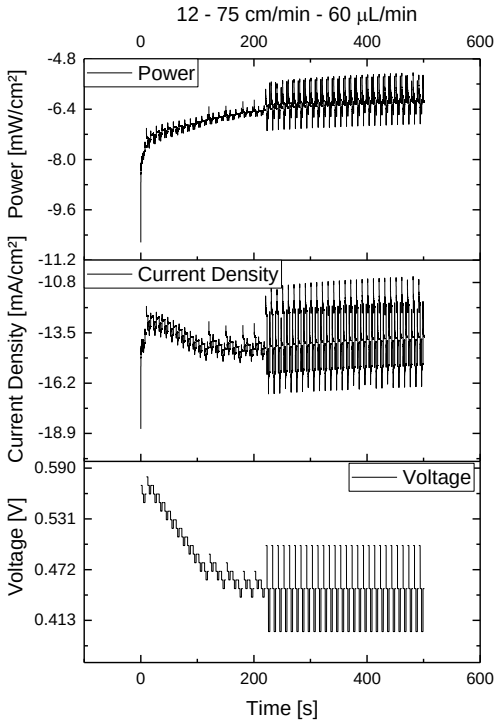

FIGURE 29. Power, Current density and voltage vs time from the TrAMPPT for the best pixel of one sample coated at web speed 75 cm/min and pump rate 60 μL/min.

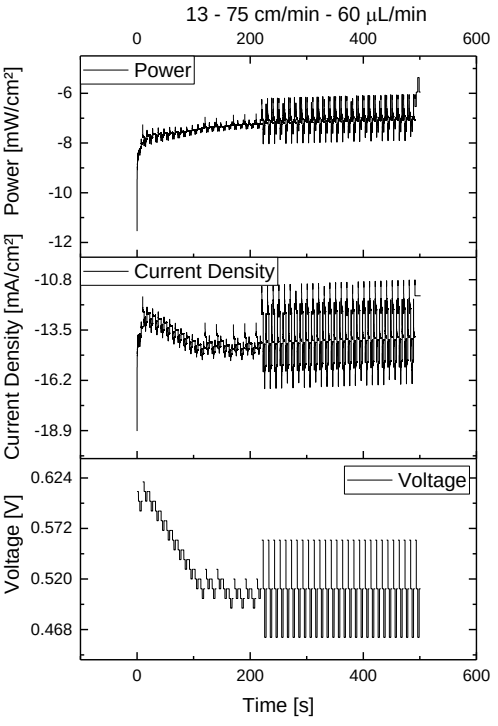

FIGURE 30. Power, Current density and voltage vs time from the TrAMPPT for the best pixel of one sample coated at web speed 75 cm/min and pump rate 60 μL/min.

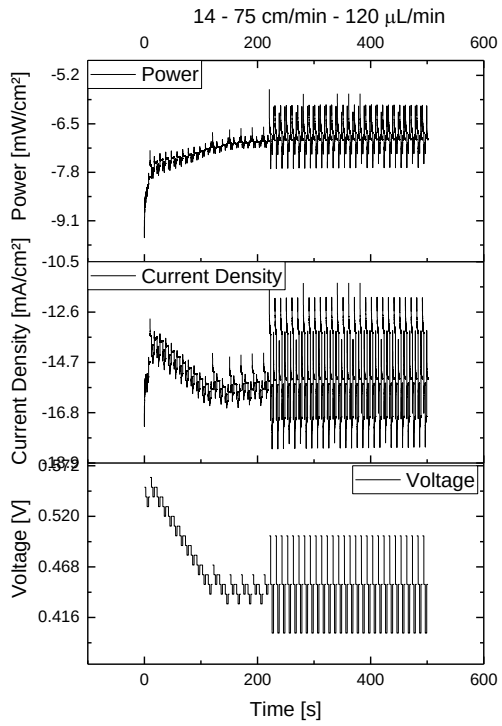

FIGURE 31. Power, Current density and voltage vs time from the TrAMPPT for the best pixel of one sample coated at web speed 75 cm/min and pump rate 120 μL/min.

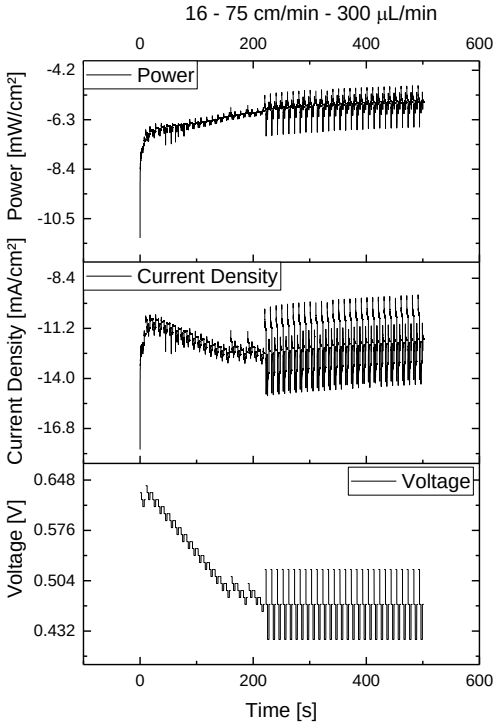

FIGURE 32. Power, Current density and voltage vs time from the TrAMPPT for the best pixel of one sample coated at web speed 75 cm/min and pump rate 300 μL/min.

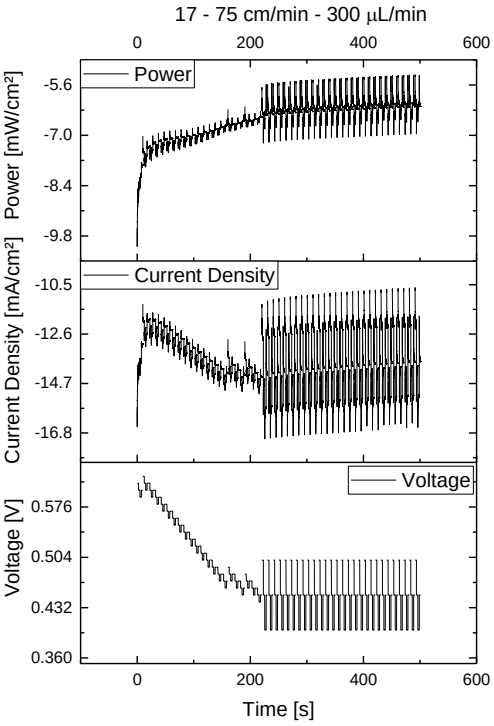

FIGURE 33. Power, Current density and voltage vs time from the TrAMPPT for the best pixel of one sample coated at web speed 75 cm/min and pump rate 300 μL/min.

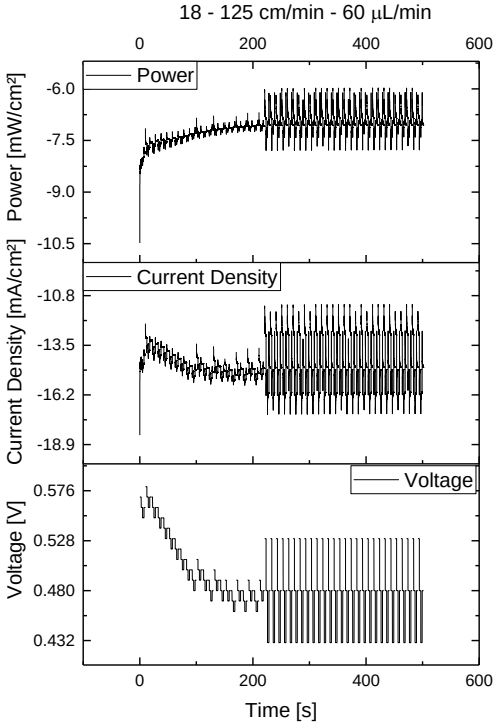

FIGURE 34. Power, Current density and voltage vs time from the TrAMPPT for the best pixel of one sample coated at web speed 125 cm/min and pump rate 60 μL/min.

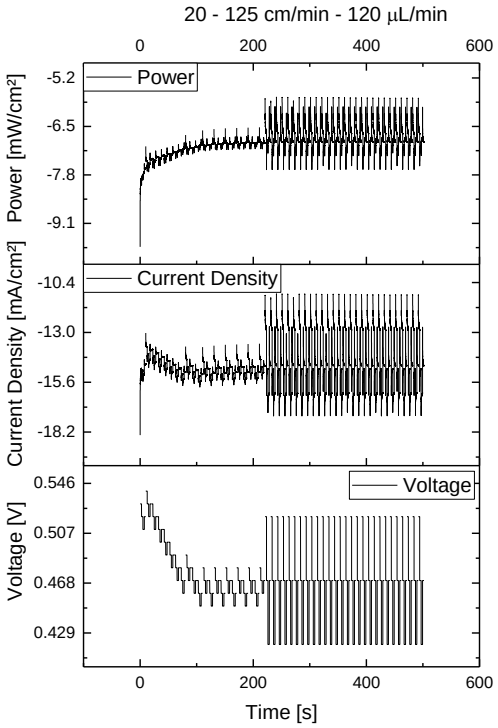

FIGURE 35. Power, Current density and voltage vs time from the TrAMPPT for the best pixel of one sample coated at web speed 125 cm/min and pump rate 120 μL/min.

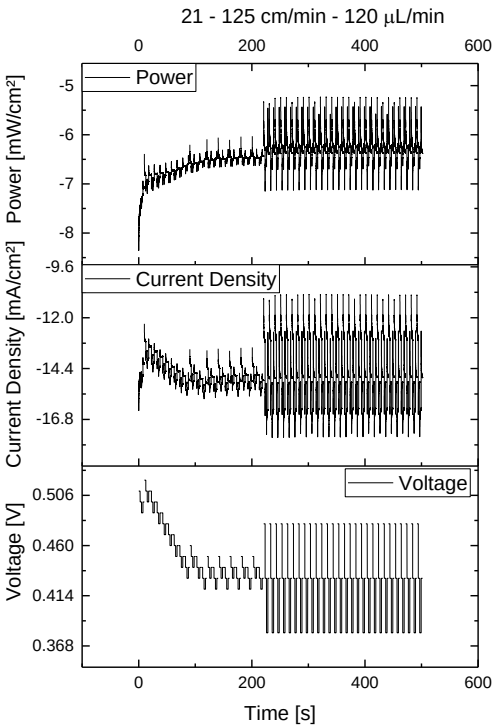

FIGURE 36. Power, Current density and voltage vs time from the TrAMPPT for the best pixel of one sample coated at web speed 125 cm/min and pump rate 120 μL/min.

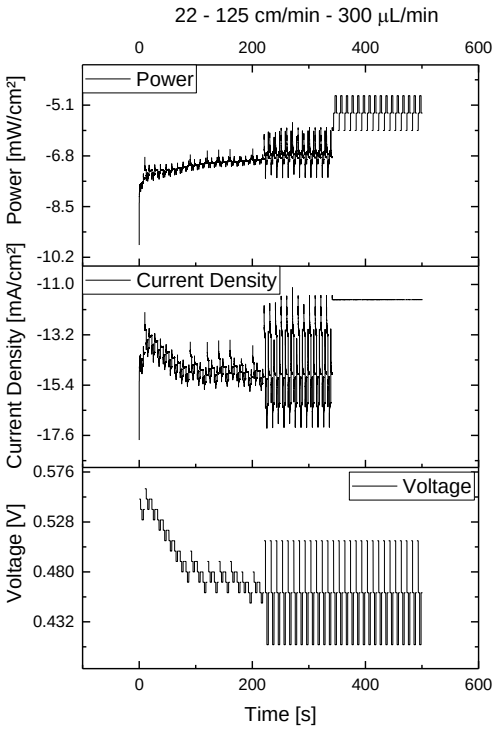

FIGURE 37. Power, Current density and voltage vs time from the TrAMPPT for the best pixel of one sample coated at web speed 125 cm/min and pump rate 300 μL/min.

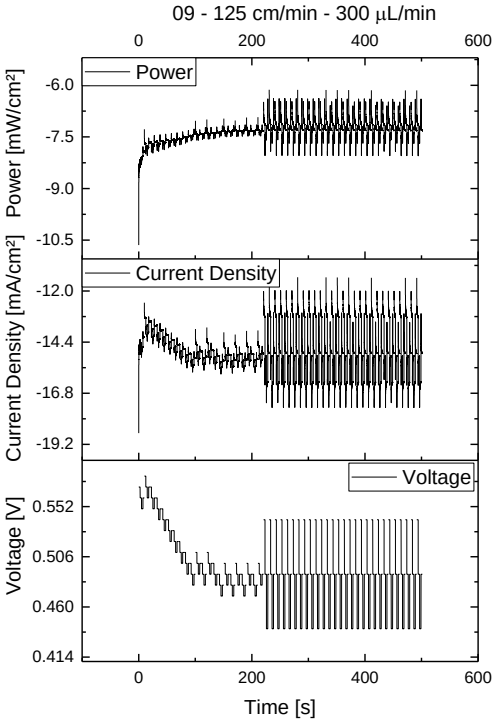

FIGURE 38. Power, Current density and voltage vs time from the TrAMPPT for the best pixel of one sample coated at web speed 125 cm/min and pump rate 300 μL/min.

6.2.4 Current Density from TrAMPPT

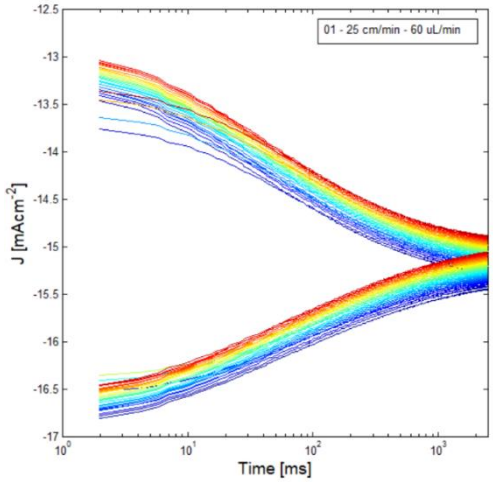

FIGURE 39. The transient current response, fitted of from the TrAMPPT for the best pixel of one sample coated at web speed 25 cm/min and pump rate 60 µL/min.

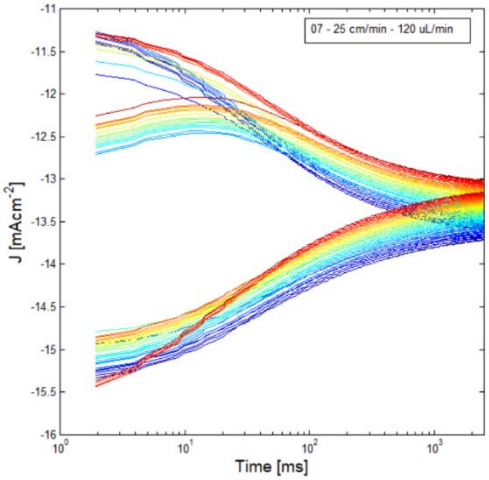

FIGURE 40. The transient current response, fitted of from the TrAMPPT for the best pixel of one sample coated at web speed 25 cm/min and pump rate 120 µL/min.

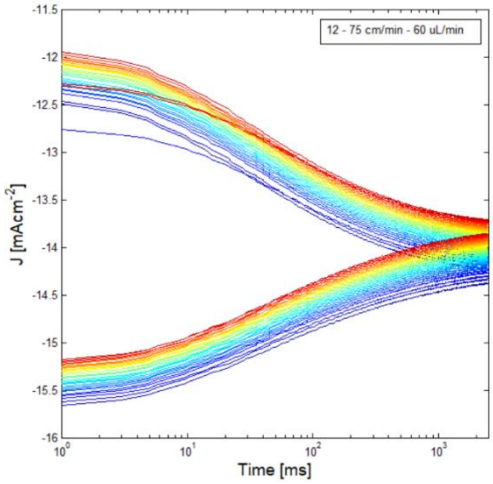

FIGURE 41. The transient current response, fitted of from the TrAMPPT for the best pixel of one sample coated at web speed 75 cm/min and pump rate 60 µL/min.

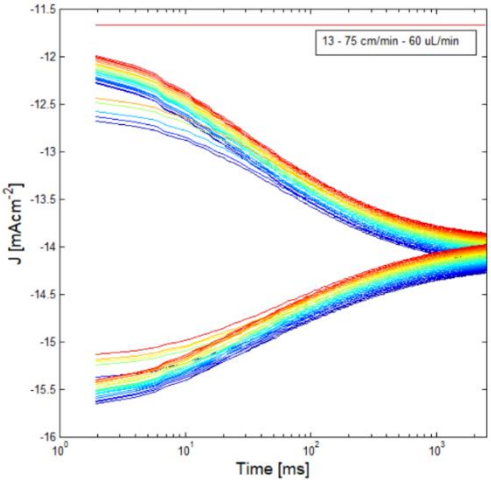

FIGURE 42. The transient current response, fitted of from the TrAMPPT for the best pixel of one sample coated at web speed 75 cm/min and pump rate 60 µL/min.

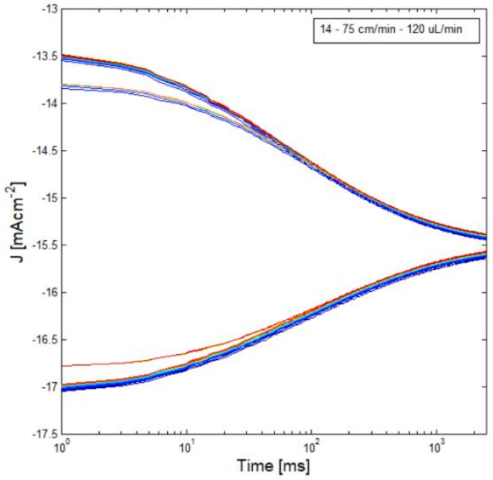

FIGURE 43. The transient current response, fitted of from the TrAMPPT for the best pixel of one sample coated at web speed 75 cm/min and pump rate 120 µL/min.

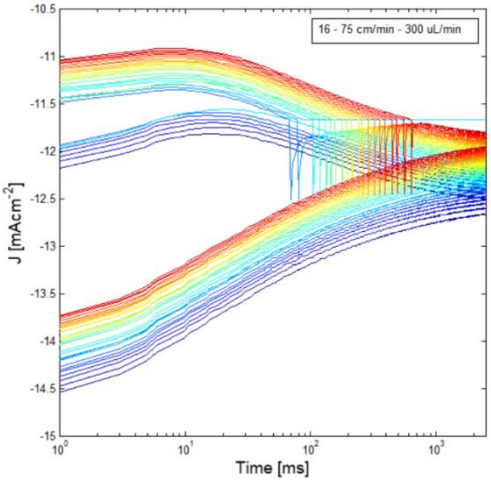

FIGURE 44. The transient current response, fitted of from the TrAMPPT for the best pixel of one sample coated at web speed 75 cm/min and pump rate 300 µL/min.

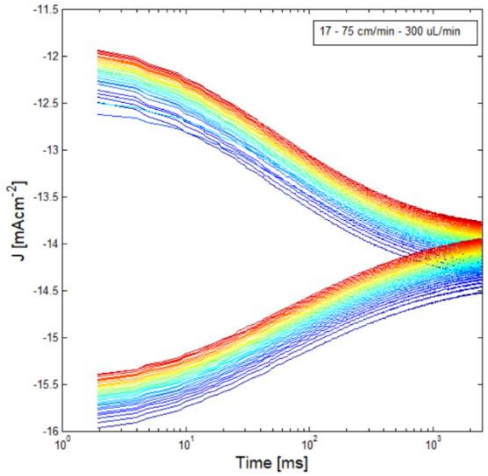

FIGURE 45. The transient current response, fitted of from the TrAMPPT for the best pixel of one sample coated at web speed 75 cm/min and pump rate 300 µL/min.

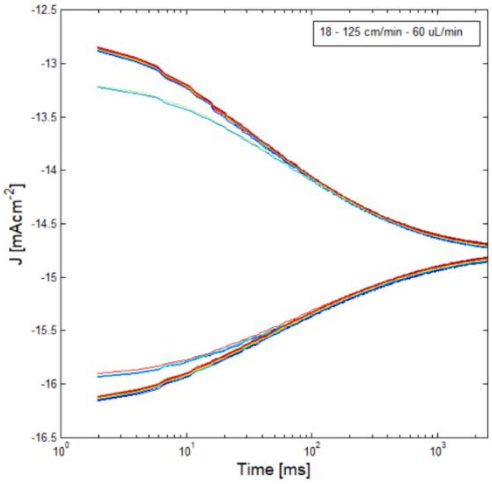

FIGURE 46. The transient current response, fitted of from the TrAMPPT for the best pixel of one sample coated at web speed 125 cm/min and pump rate 60 µL/min.

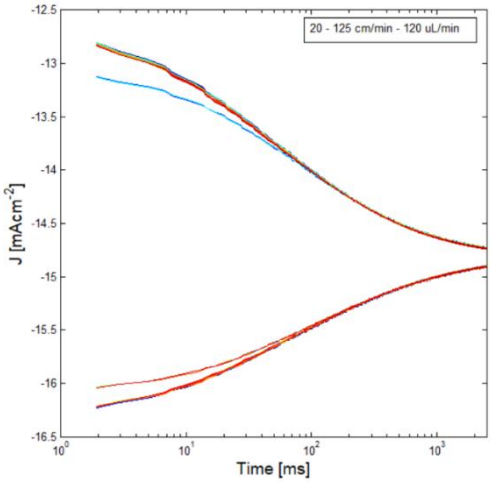

FIGURE 47. The transient current response, fitted of from the TrAMPPT for the best pixel of one sample coated at web speed 125 cm/min and pump rate 120 µL/min.

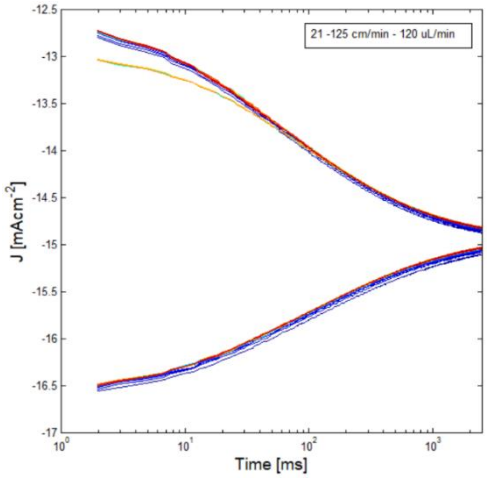

FIGURE 48. The transient current response, fitted of from the TrAMPPT for the best pixel of one sample coated at web speed 125 cm/min and pump rate 120 µL/min.

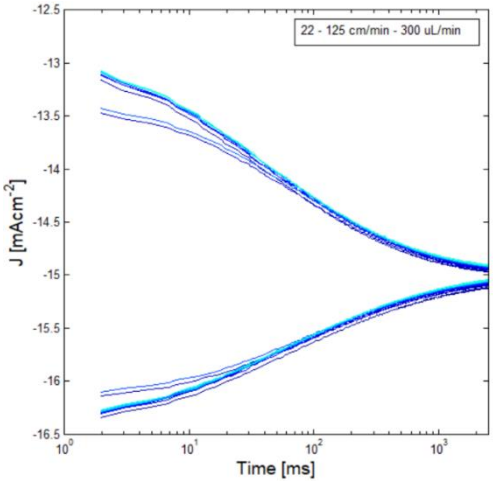

FIGURE 49. The transient current response, fitted of from the TrAMPPT for the best pixel of one sample coated at web speed 125 cm/min and pump rate 300 µL/min.

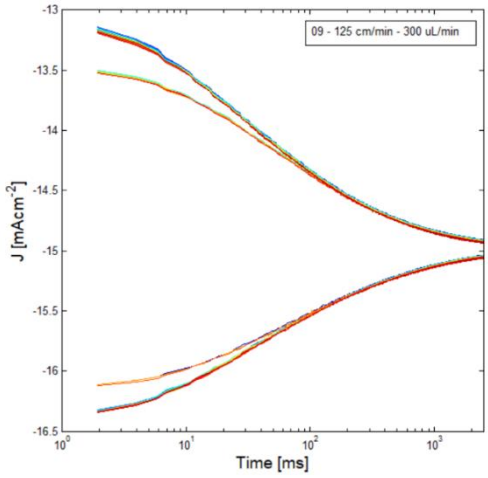

FIGURE 50. The transient current response, fitted of from the TrAMPPT for the best pixel of one sample coated at web speed 125 cm/min and pump rate 300 µL/min.

6.2.5 Time constants

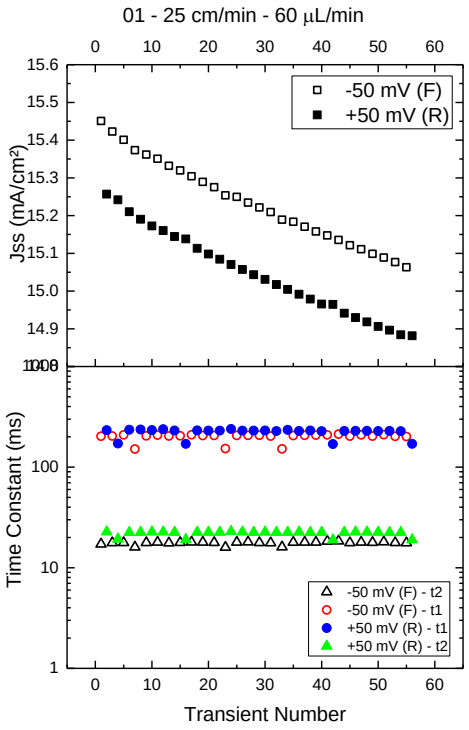

FIGURE 51. Top panel shows the steady state current (J_{ss}), and the bottom panel shows the time constants (τ_{slow} - ts - and τ_{fast} - tf -) for the sample coated at web speed of 25 cm/min and pump rate of 60 µL/min, for the -50 mV (Forward - F -) and +50 mV (Reverse - R -) steps.

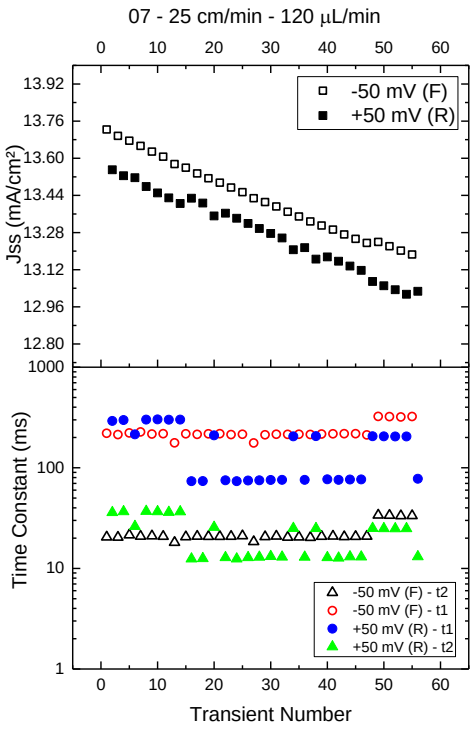

FIGURE 52. Top panel shows the steady state current (J_{ss}), and the bottom panel shows the time constants (τ_{slow} - ts - and τ_{fast} - tf -) for the sample coated at web speed of 25 cm/min and pump rate of 120 µL/min, for the -50 mV (Forward - F -) and +50 mV (Reverse - R -) steps.

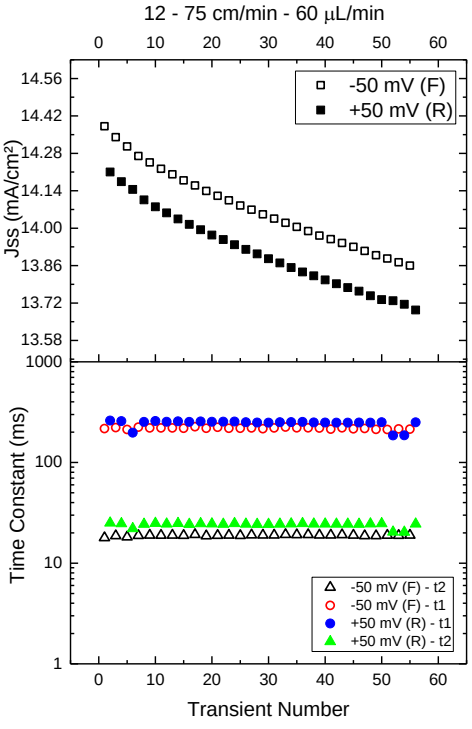

FIGURE 53. Top panel shows the steady state current (J_{ss}), and the bottom panel shows the time constants (τ_{slow} - ts - and τ_{fast} - tf -) for the sample coated at web speed of 75 cm/min and pump rate of 60 µL/min, for the -50 mV (Forward - F -) and +50 mV (Reverse - R -) steps.

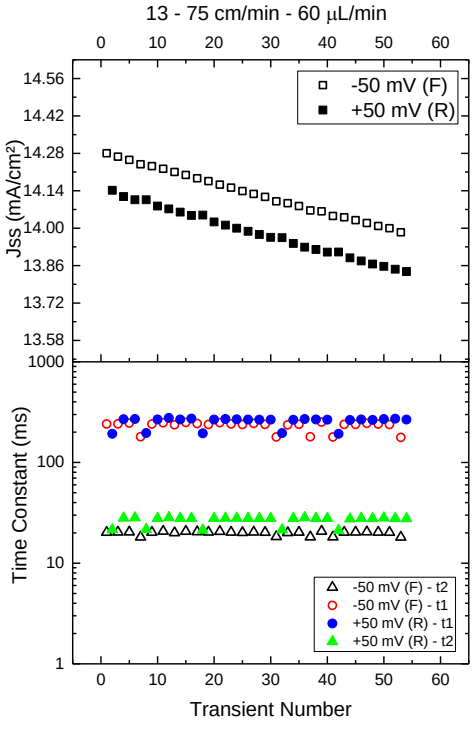

FIGURE 54. Top panel shows the steady state current (J_{ss}), and the bottom panel shows the time constants (τ_{slow} - ts - and τ_{fast} - tf -) for the sample coated at web speed of 75 cm/min and pump rate of 60 µL/min, for the -50 mV (Forward - F -) and +50 mV (Reverse - R -) steps.

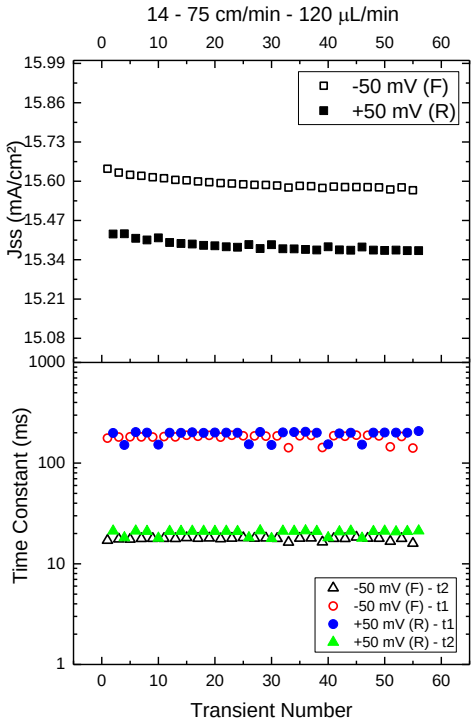

FIGURE 55. Top panel shows the steady state current (J_{ss}), and the bottom panel shows the time constants (τ_{slow} - ts - and τ_{fast} - tf -) for the sample coated at web speed of 75 cm/min and pump rate of 120 µL/min, for the -50 mV (Forward - F -) and +50 mV (Reverse - R -) steps.

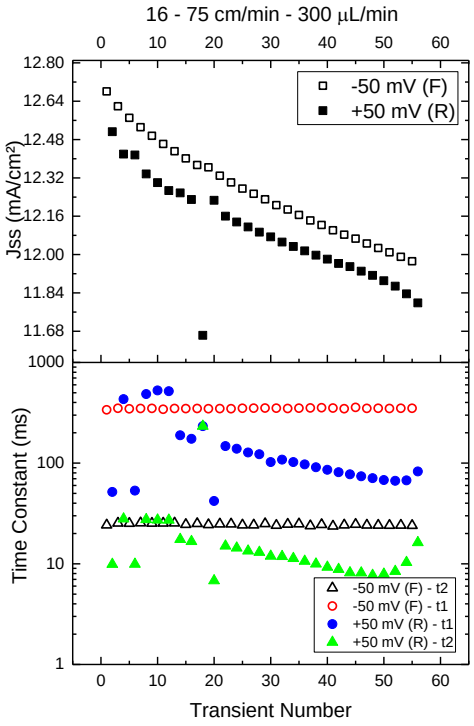

FIGURE 56. Top panel shows the steady state current (J_{ss}), and the bottom panel shows the time constants (τ_{slow} - ts - and τ_{fast} - tf -) for the sample coated at web speed of 75 cm/min and pump rate of 300 µL/min, for the -50 mV (Forward - F -) and +50 mV (Reverse - R -) steps.

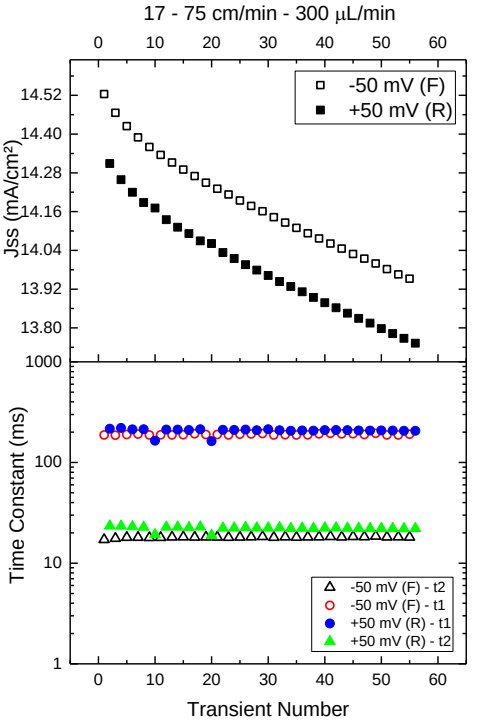

FIGURE 57. Top panel shows the steady state current (J_{ss}), and the bottom panel shows the time constants (τ_{slow} - ts - and τ_{fast} - tf -) for the sample coated at web speed of 75 cm/min and pump rate of 300 µL/min, for the -50 mV (Forward - F -) and +50 mV (Reverse - R -) steps.

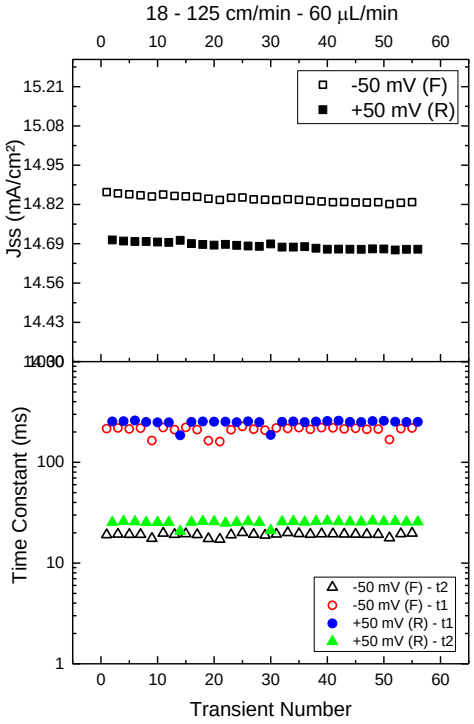

FIGURE 58. Top panel shows the steady state current (J_{ss}), and the bottom panel shows the time constants (τ_{slow} - ts - and τ_{fast} - tf -) for the sample coated at web speed of 125 cm/min and pump rate of 60 µL/min, for the -50 mV (Forward - F -) and +50 mV (Reverse - R -) steps.

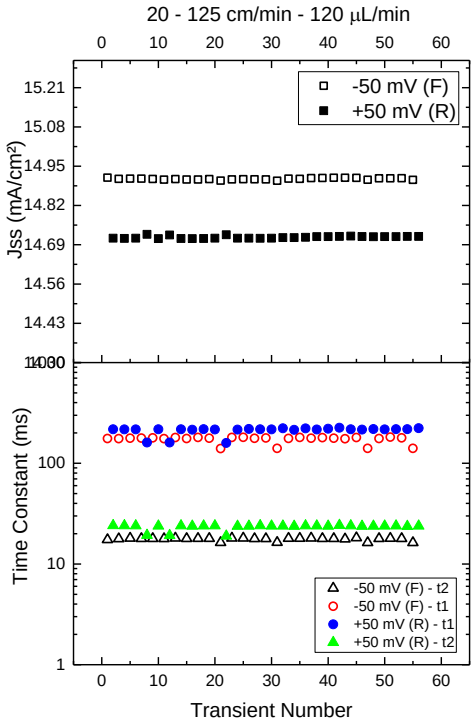

FIGURE 59. Top panel shows the steady state current (J_{ss}), and the bottom panel shows the time constants (τ_{slow} - ts - and τ_{fast} - tf -) for the sample coated at web speed of 125 cm/min and pump rate of 120 µL/min, for the -50 mV (Forward - F -) and +50 mV (Reverse - R -) steps.

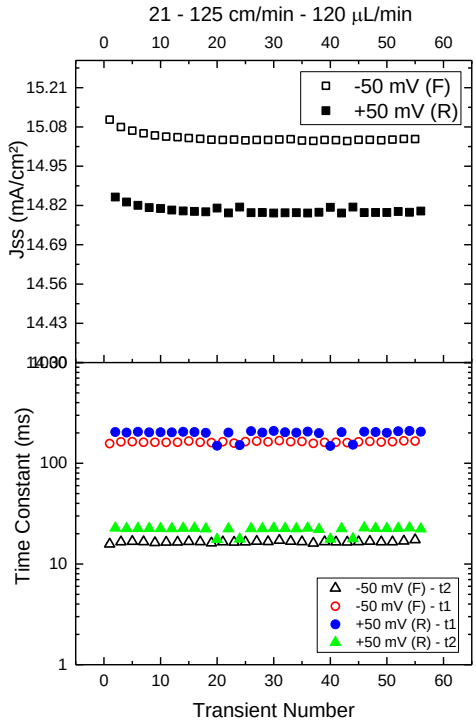

FIGURE 60. Top panel shows the steady state current (J_{ss}), and the bottom panel shows the time constants (τ_{slow} - ts - and τ_{fast} - tf -) for the sample coated at web speed of 125 cm/min and pump rate of 120 µL/min, for the -50 mV (Forward - F -) and +50 mV (Reverse - R -) steps.

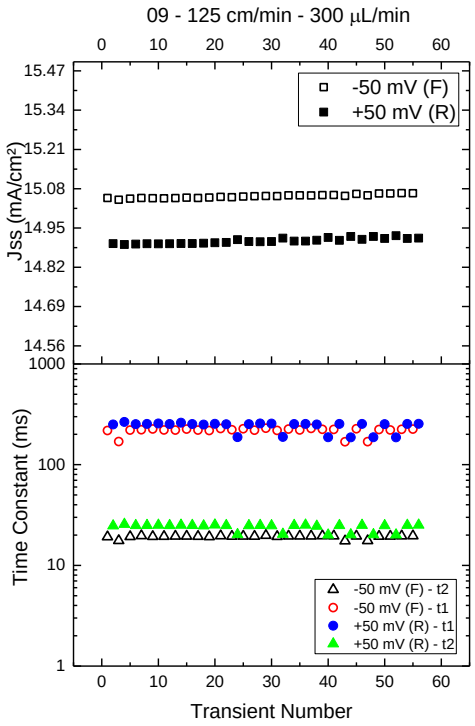

FIGURE 61. Top panel shows the steady state current (J_{ss}), and the bottom panel shows the time constants (τ_{slow} - ts - and τ_{fast} - tf -) for the sample coated at web speed of 125 cm/min and pump rate of 300 µL/min, for the -50 mV (Forward - F -) and +50 mV (Reverse - R -) steps.

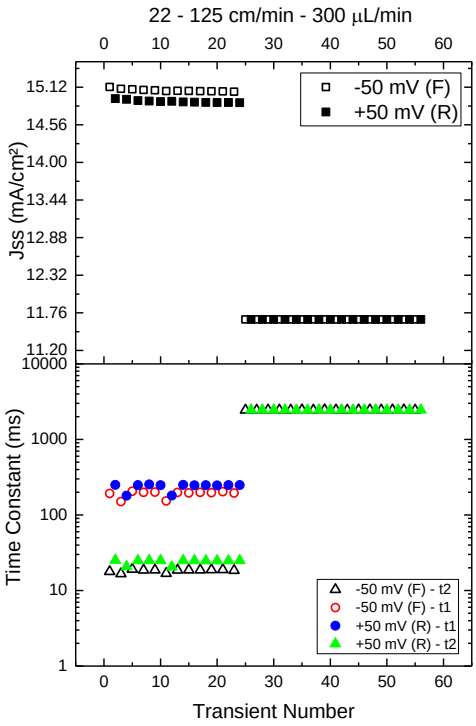

FIGURE 62. Top panel shows the steady state current (J_{ss}), and the bottom panel shows the time constants (τ_{slow} - ts - and τ_{fast} - tf -) for the sample coated at web speed of 125 cm/min and pump rate of 300 µL/min, for the -50 mV (Forward - F -) and +50 mV (Reverse - R -) steps.

6.2.5 Time dependence scans and hysteresis

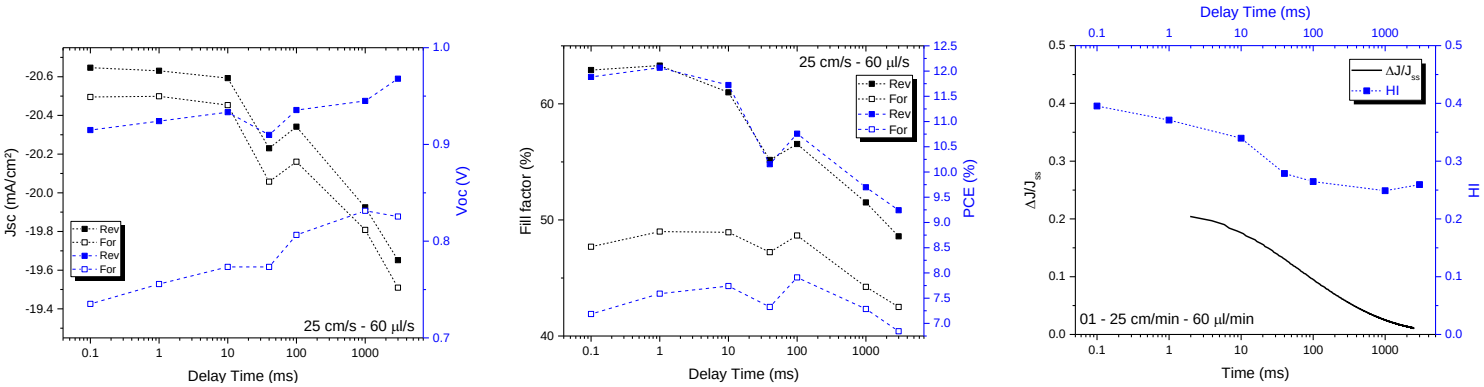

FIGURE 63. From left to right, the device main parameters from the JV curve with different delay time (as the table 6 in the main file), followed by the relative discrepancy between the reverse and forward transient current ($\Delta J/J_{ss}$) in time (left y and bottom x axis) correlated with the hysteresis index at each delay time (right y and top x axis) for the sample coated with web speed of 25 cm/min and pump rate of 60 µL/min.

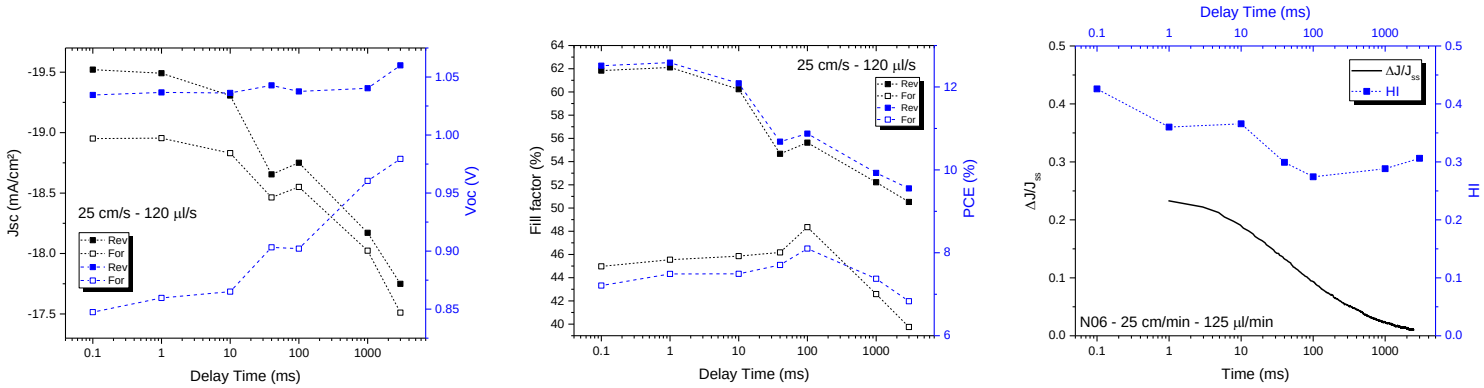

FIGURE 64. From left to right, the device main parameters from the JV curve with different delay time (as the table 6 in the main file), followed by the relative discrepancy between the reverse and forward transient current ($\Delta J/J_{ss}$) in time (left y and bottom x axis) correlated with the hysteresis index at each delay time (right y and top x axis) for the sample coated with web speed of 25 cm/min and pump rate of 120 µL/min.

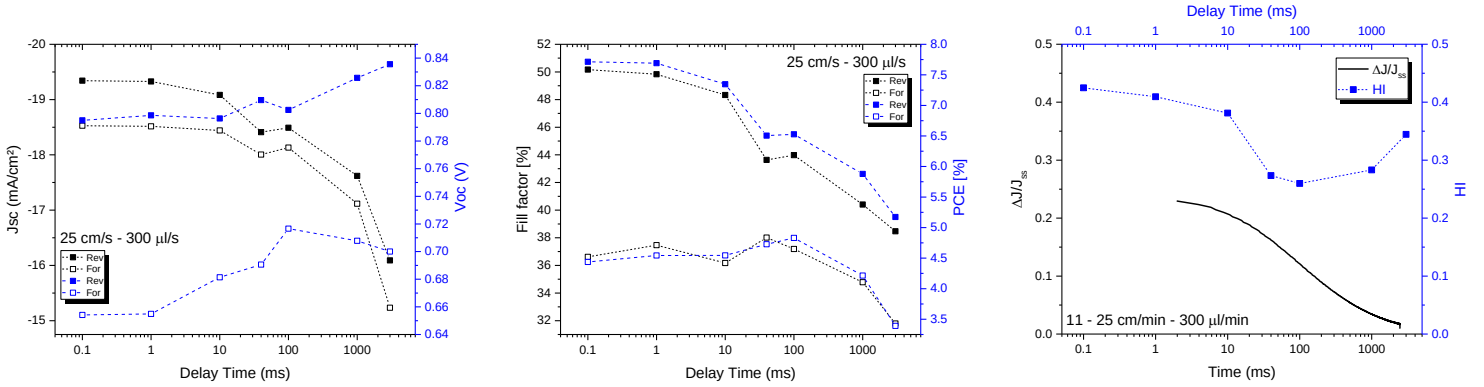

FIGURE 65. From left to right, the device main parameters from the JV curve with different delay time (as the table 6 in the main file), followed by the relative discrepancy between the reverse and forward transient current ($\Delta J/J_{ss}$) in time (left y and bottom x axis) correlated with the hysteresis index at each delay time (right y and top x axis) for the sample coated with web speed of 25 cm/min and pump rate of 300 µL/min.

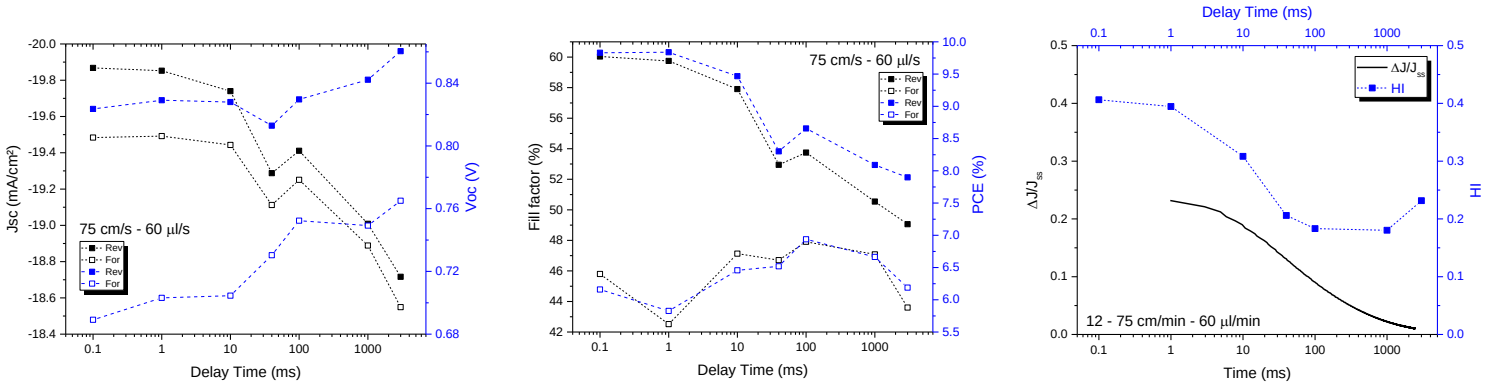

FIGURE 66. From left to right, the device main parameters from the JV curve with different delay time (as the table 6 in the main file), followed by the relative discrepancy between the reverse and forward transient current ($\Delta J/J_{ss}$) in time (left y and bottom x axis) correlated with the hysteresis index at each delay time (right y and top x axis) for the sample coated with web speed of 75 cm/min and pump rate of 60 µL/min.

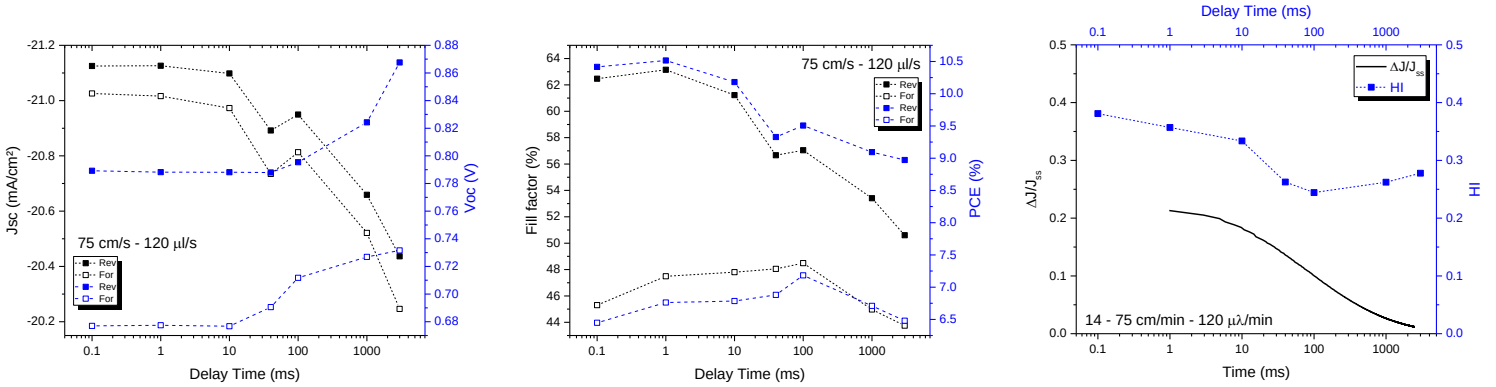

FIGURE 67. From left to right, the device main parameters from the JV curve with different delay time (as the table 6 in the main file), followed by the relative discrepancy between the reverse and forward transient current ($\Delta J/J_{ss}$) in time (left y and bottom x axis) correlated with the hysteresis index at each delay time (right y and top x axis) for the sample coated with web speed of 75 cm/min and pump rate of 120 µL/min.

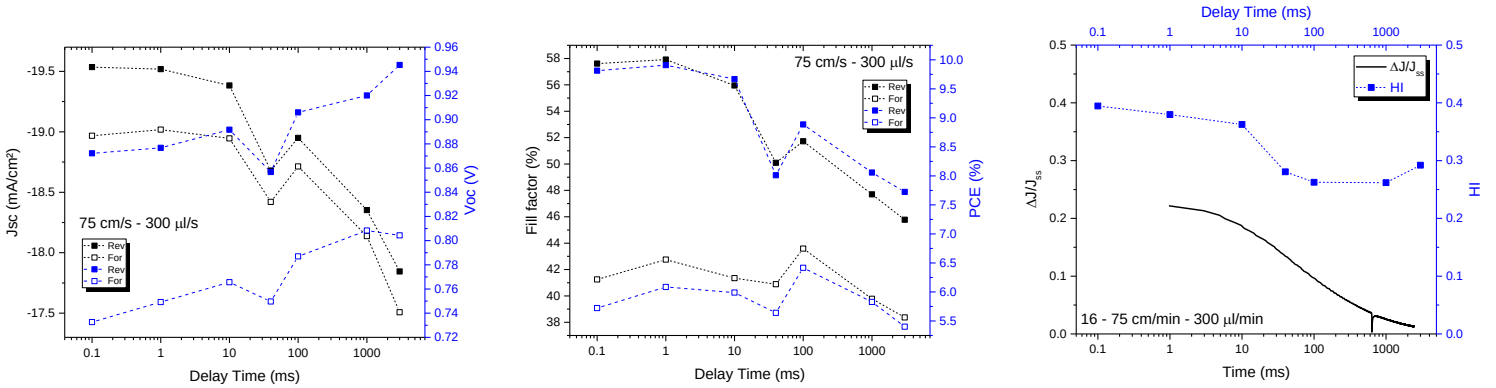

FIGURE 68. From left to right, the device main parameters from the JV curve with different delay time (as the table 6 in the main file), followed by the relative discrepancy between the reverse and forward transient current ($\Delta J/J_{ss}$) in time (left y and bottom x axis) correlated with the hysteresis index at each delay time (right y and top x axis) for the sample coated with web speed of 75 cm/min and pump rate of 300 µL/min.

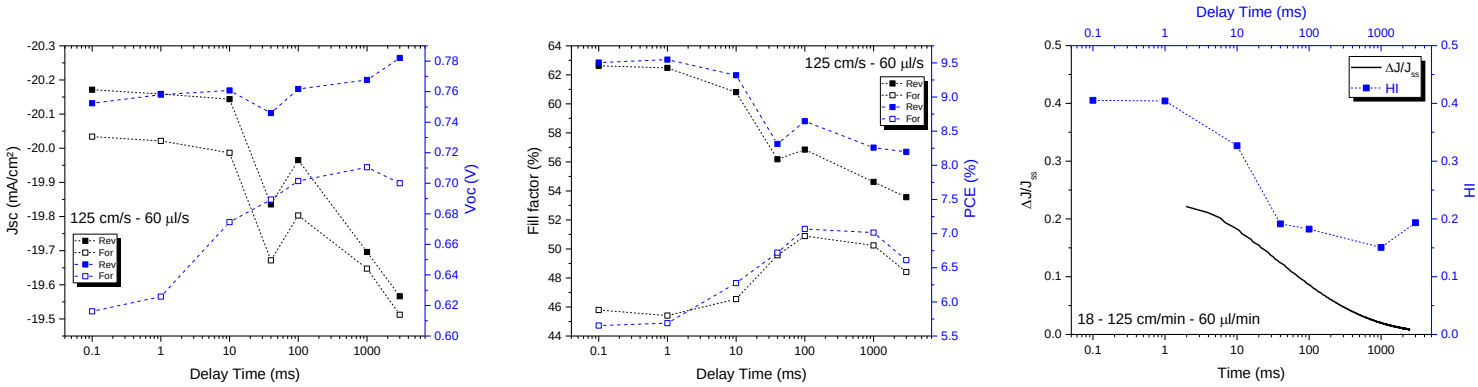

FIGURE 69. From left to right, the device main parameters from the JV curve with different delay time (as the table 6 in the main file), followed by the relative discrepancy between the reverse and forward transient current ($\Delta J/J_{ss}$) in time (left y and bottom x axis) correlated with the hysteresis index at each delay time (right y and top x axis) for the sample coated with web speed of 125 cm/min and pump rate of 60 µL/min.

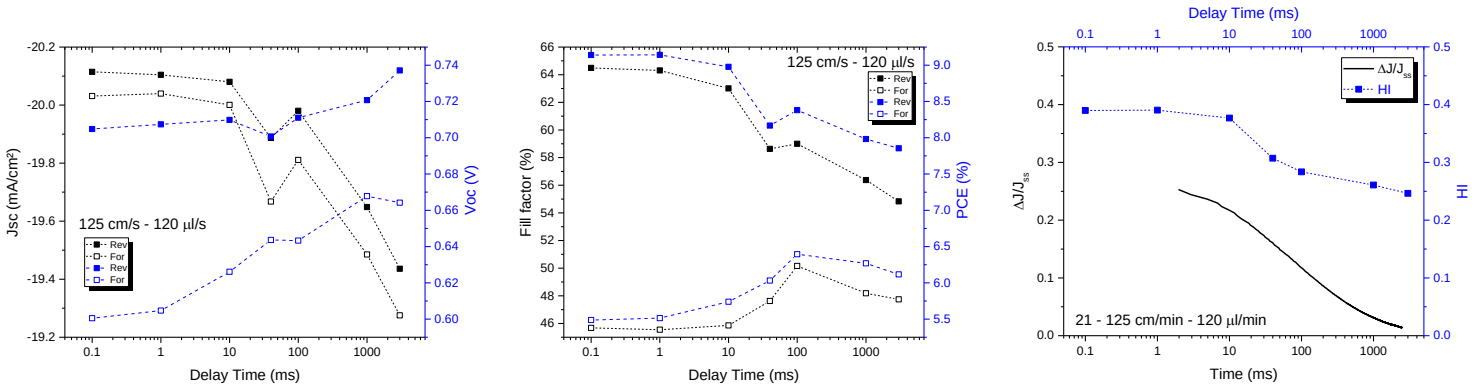

FIGURE 70. From left to right, the device main parameters from the JV curve with different delay time (as the table 6 in the main file), followed by the relative discrepancy between the reverse and forward transient current ($\Delta J/J_{ss}$) in time (left y and bottom x axis) correlated with the hysteresis index at each delay time (right y and top x axis) for the sample coated with web speed of 125 cm/min and pump rate of 120 µL/min.

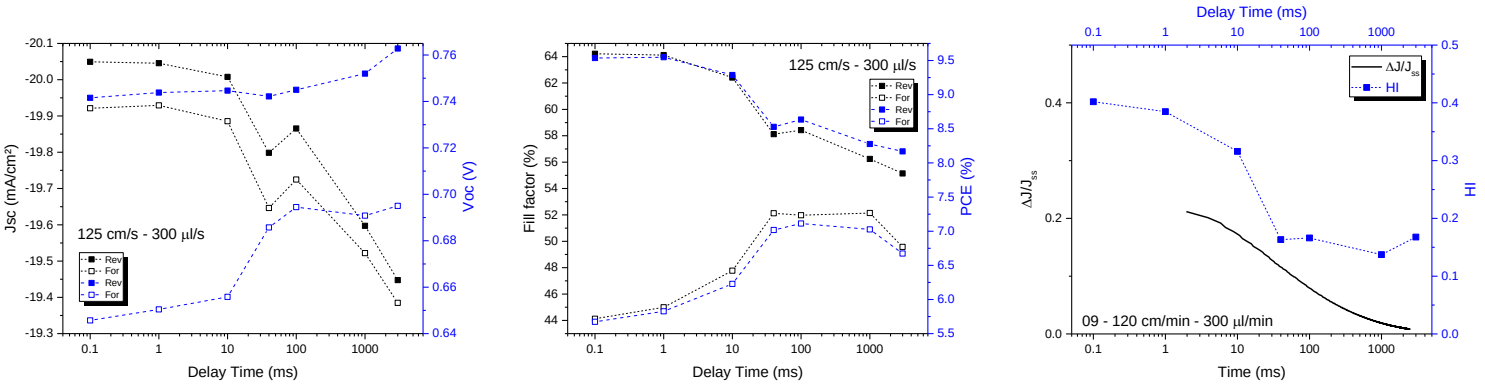

FIGURE 71. From left to right, the device main parameters from the JV curve with different delay time (as the table 6 in the main file), followed by the relative discrepancy between the reverse and forward transient current ($\Delta J/J_{ss}$) in time (left y and bottom x axis) correlated with the hysteresis index at each delay time (right y and top x axis) for the sample coated with web speed of 75 cm/min and pump rate of 300 µL/min.